Development of pulse sequences for hyperpolarized ^{13}C magnetic resonance spectroscopic imaging of tumour metabolism

Jiazheng Wang

Girton College

Supervisor: Professor Kevin Brindle

December 2017

This dissertation is submitted for the degree of Doctor of Philosophy

Declaration

This dissertation is the result of my own work and includes nothing which is the outcome of work done in collaboration except as declared in the Preface and specified in the text. It is not substantially the same as any that I have submitted, or, is being concurrently submitted for a degree or diploma or other qualification at the University of Cambridge or any other University or similar institution except as declared in the Preface and specified in the text. I further state that no substantial part of my dissertation has already been submitted, or, is being concurrently submitted for any such degree, diploma or other qualification at the University of Cambridge or any other University or similar institution except as declared in the Preface and specified in the text. The length of this dissertation does not exceed 60000 words.

Jiazheng Wang

To my parents

Acknowledgements

I am grateful to my supervisor Professor Kevin Brindle who offered me this precious chance to conduct a PhD study in a rising and exciting field. It is his guidance that keeps my research on the right track.

I am indebted to Professor Christoffer Laustsen who instructed me on the coding in many of my experiments.

I would like to thank Dr. Alan Wright very much for his instructions on the designs of my experiments and his support in every part of my work.

My thanks also go to Dr. Richard Hesketh and Dr. De-en Hu, who prepared the tumour cell line and the mice for all my animal experiments. Richard accompanied me and helped in all the in vivo experiments. He also inspired me with his expertise in biology and clinical medicine through every day's discussions.

I appreciate the help from Dr. Tiago Rodrigues and Dr. Franz Schilling. They are very inspiring through many fruitful discussions on biochemistry and MRI physics.

I would also like to thank all the lab members in the Brindle lab for their kind help in my daily work.

Final thanks go to my family, my wife, my parents, and my wife's parents. Without their support I would not have had this chance to study for a PhD and survive it.

My PhD study is funded partly by the CRUK and EPSRC Cambridge-Manchester Cancer Imaging Centre and partly by the University of Aarhus (FB Danish Strategic Research Council) LIFE DNP.

Abstract

Metabolic imaging with hyperpolarized ^{13}C-labeled cell substrates is a promising technique for imaging tissue metabolism in vivo. However, the transient nature of the hyperpolarization - and its depletion following excitation - limits the imaging time and the number of excitation pulses that can be used. A single-shot 3D imaging sequence has been developed and it is shown in this thesis to generate ^{13}C MR images in tumour-bearing mice injected with hyperpolarized [1-^{13}C]pyruvate. The pulse sequence acquires a stack-of-spirals at two spin echoes after a single excitation pulse and encodes the kz-dimension in an interleaved manner to enhance robustness to B_0 inhomogeneity. Spectral-spatial pulses are used to acquire dynamic 3D images from selected hyperpolarized ^{13}C-labeled metabolites. A nominal spatial/temporal resolution of 1.25 x 1.25 x 2.5 mm^3 x 2 s was achieved in tumour images of hyperpolarized [1-^{13}C]pyruvate and [1-^{13}C]lactate acquired in vivo. An advanced sequence is also described in this thesis in a later study to acquire higher resolution images with isotropic voxels (1.25 x 1.25 x 1.25 mm^3) at no cost of temporal resolution.

EPI is a sequence widely used in hyperpolarized ^{13}C MRI because images can be acquired rapidly with limited RF exposure. However, EPI suffers from Nyquist ghosting, which is normally corrected for by acquiring a reference scan. In this thesis a workflow for hyperpolarized ^{13}C EPI is proposed that requires no reference scan and, therefore, that does not sacrifice a time point in the dynamic monitoring of tissue metabolism.

To date, most of the hyperpolarized MRI on metabolism are based on ^{13}C imaging, while ^{1}H is a better imaging target for its 4 times higher gyromagnetic ratio and hence 16 times signal. In this thesis the world's first dynamic 1H imaging in vivo of hyperpolarized [1-^{13}C]lactate is presented, via a novel double-dual-spin-echo INEPT sequence that transfers the hyperpolarization from ^{13}C to ^{1}H, achieving a spatial resolution of 1.25 x 1.25 mm^2.

Abbreviations

bSSFP	balanced Steady-State Free Precession
COPE	Carbon-Observed-Proton-Edited
CPMG	Carr-Purcell-Meiboom-Gill
CSI	Chemical Shift Imaging
CT	Computed Tomography
DNP	Dynamic Nuclear Polarization
DDSE	Double Dual Spin Echo
DSE	Dual Spin Echo
dDNP	dissolution Dynamic Nuclear Polarization
EPI	Echo Planar Imaging
EPSI	Echo Planar Spectroscopic Imaging
FDG	Fluorodeoxyglucose
FOV	Field of View
FSE	Fast Spin Echo
FWHM	Full Width at Half Maximum
GRE	Gradient Echo
HS	Hyperbolic-Secant
HSQC	Heteronuclear Single Quantum Coherence
IDH	Isocitrate Dehydrogenase
INEPT	Insensitive Nuclei Enhanced by Polarization Transfer

LDH	Lactate Dehydrogenase
MR	Magnetic Resonance
MRI	Magnetic Resonance Imaging
MRS	Magnetic Resonance Spectroscopy
MRSI	Magnetic Resonance Spectroscopic Imaging
NAD+	Nicotinamide Adenine Dinucleotide (oxidised)
NADH	Nicotinamide Adenine Dinucleotide (reduced)
PDH	Pyruvate Dehydrogenase
PET	Positron Emission Tomography
PPP	Pentose Phosphate Pathway
PSF	Point Spread Function
RF	Radio Frequency
ROI	Region of Interest
SAR	Specific Absorption Rate
SE	Spin Echo
SNR	Signal-to-Noise Ratio
SpSp	Spectral Spatial
SSIM	Structural Similarity
TCA	Tricarboxylic Acid
TE	Echo Time

List of publications

The following chapters have been published, accepted for publication, or will be submitted for publication. All of these manuscripts were written by me and revised by my co-authors.

Chapter 2 This Chapter is based upon the following publication:

Wang J, Wright AJ, Hu D, Hesketh R, Brindle KM. Single shot three-dimensional pulse sequence for hyperpolarized ^{13}C MRI. Magn Reson Med 2017; 77: 740-752

Chapter 3 This Chapter is based upon a paper that has been submitted for publication:

Wang J, Hesketh RL, Wright AJ, Brindle KM. High resolution hyperpolarized ^{13}C spectroscopic imaging using optimized single shot 3D sequences. Magn Reson Med; under review

Chapter 4 This Chapter is based upon the following publication:

Wang J, Wright AJ, Richard LH, Hu D, Brindle KM. A referenceless Nyquist ghost correction workflow for echo planar imaging of hyperpolarized [1-^{13}C]pyruvate and [1-^{13}C]lactate. NMR Biomed 2017; DOI: 10.1002/nbm.3866

Chapter 5 This Chapter is based upon the following publication:

Wang J, Kreis F, Wright AJ, Hesketh RL, Levitt MH, Brindle KM. Dynamic ^{1}H imaging of hyperpolarized [1-^{13}C]lactate in vivo using a reverse INEPT experiment. Magn Reson Med 2017; DOI: 10.1002/mrm.26725

Table of Contents

Table of Figures

1. General Introduction

1.1. Background

Cancer is amongst the leading causes of mortality in the developed world. In 2012 there were more than 14 million new cancer cases diagnosed worldwide, and about 8.2 million people died, more than the total number of deaths caused by coronary heart disease [1]. Cancer is difficult to treat because it is very heterogeneous both inter-tumourally [2] and intra-tumourally [3]. Different patients with similar cancer types can respond very differently to the same therapy [4], and even within the same tumour different regions can show different responses [5]. A common goal in cancer research and clinical cancer treatment is to detect early the efficacy of cancer drugs and treatments, which can then be targeted at those that would benefit the most [6].

In the clinic the effects of tumour treatment are usually assessed by medical imaging techniques, such as computed tomography (CT), magnetic resonance imaging (MRI), and ultrasound, where the aim is to look for changes in tumour size post treatment [7]. However, morphological changes in tumours can take weeks or even months to occur, and therefore ineffective treatments may be given over prolonged periods at the cost of patient suffering and unnecessary costs to the healthcare system [8]. This limitation of anatomical imaging has led to a search for new imaging methods that can give a more rapid evaluation of the effect of treatment. Tumours are known to possess altered metabolism [9], which for a long time has been known to show early changes after treatment. For example, in 1989 Rozental and colleagues noted acute changes in glucose uptake after treating gliomas with chemotherapy [10], and 2 years later a similar phenomenon was observed in gliomas treated with radiotherapy [11].

MRI is among the most promising candidates for early assessment of tumour treatment response because, in principle, it is capable of simultaneously monitoring numerous metabolites in cells by exploiting their different chemical shifts. Magnetic resonance spectroscopy (MRS) studies of tissue metabolism have been conducted since the late 1970s, especially ^{31}P MRS studies of tissue energetics in normal, stress, and pathological

conditions [12]. Metabolites such as lactate and cholines have been identified as biomarkers for tumour diagnosis and treatment monitoring and have been translated into clinical use [13]. The clinical use of MRS is limited primarily by its lack of spatial resolution, which is not ideal considering the heterogeneity present in the tumours. MRI, on the other hand, has not been used routinely as a functional imaging tool at molecular level, despite the extensive studies imaging brain function. MRI as a molecular imaging tool is limited by its low sensitivity and the relatively low concentrations of metabolites when compared to tissue water. Routine clinical MRI detects the magnetic resonance signal of water and lipid protons and benefits from their abundance throughout the human body. In contrast, cell metabolites are usually present at about 10000 times lower concentration than water [8]. As a result, it is impossible to acquire images of metabolites at a useful resolution and in a clinically acceptable period of time. However, high resolution is needed to reveal the heterogeneous nature of tumour metabolism. For example, an individual lung tumour can have regions that show either anaerobic or aerobic glucose metabolism [14], and can be either glucose avid or glutamine avid [15], depending on the local environment. Low sensitivity and low metabolite concentrations also limit the acquisition of dynamic information, which is important for kinetic analyses of metabolism. The pioneering research of Golman, Ardenkjaer-Larsen and colleagues in 2003 showed that the sensitivity of the magnetic resonance experiment could be enhanced by more than 10000 times after tens-of-minutes of dynamic nuclear polarization (DNP). In this process nuclear spins in the solid state are hyperpolarized, followed by a dissolution process that can then allow observation of the hyperpolarized molecules in vivo [16]. Dissolution Dynamic Nuclear Polarization (dDNP or simply DNP in the context of this thesis) has made possible the imaging of cell metabolites as well as dynamic analysis of their metabolism. This has been exploited to monitor tumour treatment response by probing the changes in cell metabolism before and after treatment.

My PhD research has focused on developing imaging techniques for hyperpolarized MRI that can be used to image tumour metabolism in vivo. Chapter 1 introduces the motivations behind the study, outlines the basic physics of DNP and MRI, and provides an overview of the possible hyperpolarized imaging agents and the prior-art imaging

techniques that have been described in the literature. Chapter 2 proposes a new imaging sequence for hyperpolarized MRI, where the aim was to achieve high signal-to-noise ratio (SNR) and high spatial and temporal resolutions with the minimum number of excitation pulses. Chapter 3 describes an enhanced version of the sequence described in Chapter 2 that doubles the spatial resolution at no cost of temporal resolution and minimises loss of SNR. Chapter 4 describes adaptation of a technique used in water proton imaging to ^{13}C imaging that can be used to remove Nyquist ghosting in echo planar imaging (EPI) without additional data acquisition. Chapter 5 shows how hyperpolarized ^{1}H imaging could be realized in vivo by transferring hyperpolarization from ^{13}C to ^{1}H. Chapter 6 includes a general discussion of the studies presented in Chapters 2 to 5 and proposes the subjects for future research.

1.2. DNP

Magnetic resonance experiments study the microenvironment and properties of the nuclei through their interactions with magnetic fields. Most elementary particles possess intrinsic angular momentum, known as spin. Quantum mechanics describes a spin system with two quantum numbers, the spin quantum number, and the azimuthal quantum number, which describes the number of sub energy levels with a certain spin quantum number. ^{1}H and ^{13}C nuclei, the principal nuclei studied using MRI and hyperpolarized MRI, both have spin number 1/2 and are known as spin-1/2 systems. In the presence of an external magnetic field, B_0, the spin-1/2 system splits into two sub energy levels (Zeeman Splitting), as shown in Figure 1.1A. Since one of the energy levels (the $|\alpha\rangle$ state) has slightly lower energy than the other ($|\beta\rangle$ state), it is slightly more energetically favourable and is therefore slightly more populated. The spin population difference between these two quantum states builds up a polarization, which at thermal equilibrium is dependent on the Boltzmann distribution, where the lower energy population is only about $\left(\frac{1}{2}+\frac{1}{4}\mathbf{B}\right)$ and the higher energy population is $\left(\frac{1}{2}-\frac{1}{4}\mathbf{B}\right)$. $\mathbf{B}$ is the Boltzmann factor, defined as:

$$\mathbf{B}=\frac{\hbar\gamma\mathrm{B}_0}{\mathrm{k}_\mathrm{B}\mathrm{T}} \qquad 1.1$$

where $\hbar$ is Planck's constant (in J∗s/rad), γ is the gyromagnetic ratio, B_0 is the magnetic field strength, k_B is the Boltzmann constant, and T is the absolute temperature [17]. For ^{1}H spins at a magnetic field strength of 3 T and room temperature, this equation gives approximately 10 more lower energy spins per million, which are the only spins that can contribute to the MR signal, leading to the intrinsic low sensitivity of the MR experiment. If we define the polarization as the excess number of spins at the lower energy level as a percentage of the total number of spins, then at thermal equilibrium:

$$\text{Thermal Polarization} = \frac{1}{2}\mathbf{B} \qquad 1.2$$

The thermal polarization of ^{1}H at 3 T and room temperature is then 0.001%.

The maximal possible signal in a MR experiment is determined not only by the polarization but also by the total spin population. The key factor behind the success of clinical MRI is that water protons, the signal source for the clinical MRI, have a concentration of approximately 80 M in human tissues [8]. Therefore, about 0.08 mmol spins contribute to the signal in a 1 mm^3 voxel in the MRI scan. In contrast, metabolites usually have a concentration in the millimolar range [18], so that the number of MR-detectable spins is only on the nanomol scale in a 1 mm^3 voxel.

Since metabolite concentrations could not be increased globally in the human body, it is desirable to enhance the spin polarization when performing MR experiments, which is conventionally achieved by increasing the magnetic field strength. Electrons have much higher polarization than nuclear spins due to their much larger gyromagnetic ratio (the electron gyromagnetic ratio is about 650 times the proton gyromagnetic ratio). This means that at low temperature (~ 1-2K) and high magnetic field, such as 3 T, the electrons have almost 100% polarization. DNP technique makes use of this high electron spin polarization and transfers it to the nuclear spins [19]. In the DNP process, molecules with the target nuclei (e.g. ^{13}C) are mixed with a source of unpaired electrons (a stable radical) and then placed in a magnetic field at low temperature. In the simplest case where one electron spin couples with only one nuclear spin, four Zeeman energy levels are formed within this two spin system (Figure 1.1B). Microwave irradiation that matches the energy difference

between electron and nuclear spins is then used to force the spin transition from the lower energy spin state to the higher energy spin state via the dipole coupling between the electron and the nuclear spins [20], as illustrated in Figure 1.1C. In addition to microwaves at the right frequency, another factor that leads to highly polarized nuclear spins is very short spin-lattice relaxation (or, T_1 relaxation) time of the electrons. Spin-lattice relaxation is a process where the spin populations recover to their Boltzmann distribution from an excited state (for example, the hyperpolarized state) [21]. At the operating temperature of DNP, electrons possess T_1s in the millisecond range, while the nuclear spin T_1s are usually in the 1000 seconds range. This dramatic difference in T_1 means that the DNP process is so fast that the hyperpolarized nuclear spins preferentially remain in the excited state instead of quickly relaxing back to thermal equilibrium. Depending on the radical used as the source of the unpaired electrons and its concentration relative to the target molecule, the DNP process is more complex and involves thermal mixing effects, where one electron spin interacts with multiple nuclear spins [22]. For the DNP process described in this thesis, thermal mixing is the dominant mechanism since the electron absorption spectrum line width of the radical used is much broader than the nuclear spin resonance frequency. Therefore, it is difficult to cover all electron spins with a single frequency microwave irradiation, leading to a relatively long hyperpolarization time.

The dissolution DNP technique uses superheated water (~180^{o}C at ~ 10 bar) to melt the hyperpolarized sample from the solid state in less than a second. The hyperpolarized sample shows almost no polarization loss during the dissolution process and could enhance the MR signal by more than 10000 times when used for imaging of cell metabolism in vivo [23].

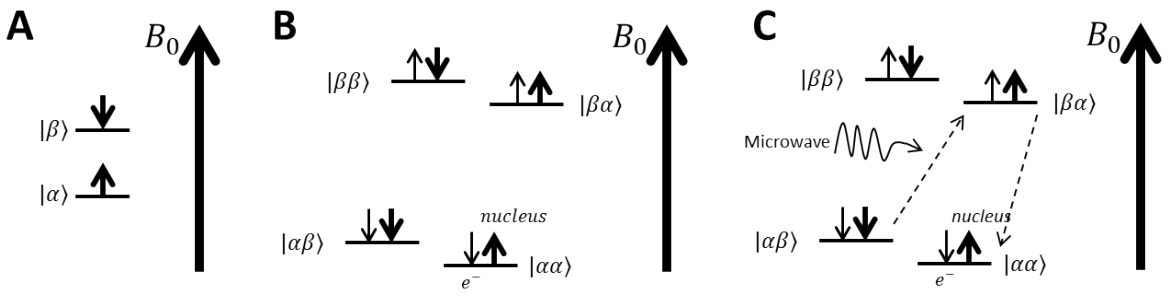

Figure 1.1: Spin system in DNP
(A) Zeeman splitting of a single spin system, where |α⟩ state possesses slightly lower energy than |β⟩ state and is hence slightly more populated. (B) Two spin system (an electron spin and a nuclear spin) where four sub-energy levels are present. (C) Microwave irradiation at a certain frequency enhances the nuclear polarization through the dipole coupling between the electron and nuclear spins.

1.3. Hyperpolarized imaging agents

This section gives an overview of the possible imaging agents, and a brief introduction to the MRI techniques will be covered in the following two sections.

Selection of imaging agents

For a substrate to be used clinically for imaging tumour metabolism it must satisfy several conditions [24]. The substrate should be able to form a glass in the solid state, it should play an important role in tumour metabolism, and its metabolism should be fast enough to be observed before complete decay of the polarization. Thus the observed nucleus in the substrate should have a relatively long T_1, since the slower the T_1 relaxation the longer the signal will be available for MR observation. Significant chemical shift differences should exist between the substrate and its metabolic products to allow observation of separable MRI signals. Other requirements include fast transport across a cell's plasma membrane and lack of toxicity. In summary, a potential candidate for a hyperpolarized imaging agent needs to provide information of biological importance within a feasible imaging time.

The hyperpolarization process described above naturally excludes the use of macromolecules such as proteins, because the extremely low temperature during the

polarization transfer and the high temperature during the dissolution process can denature these molecules. This is not a concern for small molecules, such as metabolites in the glycolytic pathway and tricarboxylic acid (TCA) cycle. Despite its abundance in these metabolites, ^{1}H is not a good target for hyperpolarization because of its relatively short T_1 when compared to other nuclei, such as ^{13}C. A shorter T_1 means more polarization loss during dissolution as well as during the transfer and perfusion processes, where the hyperpolarized agent is relocated to the imaging object, injected, brought to the target region by the circulation, and taken up by the cells. Carbon is the second most abundant element in human body. ^{12}C, the dominant isotope of carbon, does not possess spin and therefore does not give rise to an MR signal, whereas ^{13}C, a spin-1/2 nucleus, has a natural abundance of only ~1%. The relatively long ^{13}C T_1 in many important metabolites allows for efficient hyperpolarization of ^{13}C-labeled metabolites and has made possible imaging of relatively low concentrations of these molecules in vivo with sufficient SNR at a sub-second frame rate. Most of the dissolution DNP based MRI experiments have been performed with the ^{13}C nucleus, although a study has also been conducted with hyperpolarized H_2O [25]. This thesis focuses on the studies with [1-^{13}C]pyruvate, but many other possible imaging agents for hyperpolarized ^{13}C MRI have also been introduced and are described in the following.

[1-^{13}C]pyruvate

The most widely used agent so far has been [1-^{13}C]pyruvate [26], which has already been used in clinical experiments [27-29]. Pyruvate plays an active role in the hyperpolarized MRI field because it is the end product of glucose metabolism, and glucose metabolism in tumours is usually altered such that a large proportion of the pyruvate is converted into lactate, even in the presence of oxygen [9], rather than entering the TCA cycle, as in most normal tissues. This phenomenon is known as the Warburg effect or aerobic glycolysis [30]. This altered pathway, provides a large pool of glycolytic intermediates for biosynthetic purposes, which can be used to drive tumour cell proliferation, and it also regenerates NAD+ from NADH through the conversion of pyruvate to lactate, which allows continued operation of the glycolytic pathway [31]. Aerobic glycolysis also contributes, via the pentose phosphate pathway, to the production of NADPH,

which is a reducing equivalent for anabolic reactions and which maintains redox balance in tumour cells [32]. Aerobic glycolysis results from the upregulation of many of the glycolytic enzymes [33], including lactate dehydrogenase (LDH), which catalyses the exchange of hyperpolarized ^{13}C label between pyruvate and lactate, as well as a decrease in the rate of entry of pyruvate into the TCA cycle via pyruvate dehydrogenase (PDH). PDH activity is suppressed by pyruvate dehydrogenase kinase, whose expression is promoted by HIF-1, otherwise PDH would divert pyruvate into the TCA cycle [34].

Brindle and colleagues showed that MRI measurements of the exchange of hyperpolarized ^{13}C label between injected [1-^{13}C]pyruvate and the endogenous lactate pool enabled immediate monitoring of changes in LDH activity after tumour treatment with etoposide [35]. Later studies by the same group [36] and Saito et al [37] demonstrated similar results with hyperpolarized [1-^{13}C]pyruvate imaging in different tumour models treated with radiotherapy. Treatments targeting phosphatidylinositol 3-kinase (PI3K), which lowers LDH activity, have been shown to be assessable using hyperpolarized [1-^{13}C]pyruvate MRI [38,39] and Bohndiek et al [40] and Park et al [41] showed that hyperpolarized [1-^{13}C]pyruvate could also be used to detect early response to anti-vascular treatments. Imaging with hyperpolarized [1-^{13}C]pyruvate has also been shown capable of detecting occult lesions [27] and for monitoring tumour progression [42,43]. In addition to these applications in tumour imaging, [1-^{13}C]pyruvate has also been used to assess diabetic heart [44] and kidney [45], to measure pH in heart [46], as well as acute changes in renal metabolism induced by soft drinks [47].

Other ^{13}C labelled imaging agents

Numerous hyperpolarized^{13}C labelled imaging agents have been developed. Brindle and colleagues suggested that hyperpolarized [5-^{13}C]glutamine could be used to detect hepatocellular carcinoma detection because its rapid consumption in proliferating tumour cells [48]. They also showed that hyperpolarized ^{13}C bicarbonate could be used for pH mapping, which is important in studies of the tumour microenvironment [49,50], [1,4-$^{13}C_2$]fumarate can be used for imaging cell death, providing an immediate metric of tumour treatment response [51,52], ^{13}C vitamin C has been used to probe tumour cell redox status

[53,54], [1-^{13}C]glutamate to study tumour energy and amino acid metabolism [55], and ^{13}C labelled glucose to study glycolytic flux and pentose phosphate pathway (PPP) activity in tumours [56,57]. Chaumeil et al studied the isocitrate dehydrogenase 1 (IDH1) mutation in glioma with hyperpolarized [1-^{13}C]α-ketoglutarate, which can be converted into [1-^{13}C]2-hydroxyglutarate and [1-^{13}C]glutamate in IDH1 mutated glioma cells [58,59]. Mzauel et al demonstrated the intracerebral synthesis of [1-^{13}C]glutamine from [1-^{13}C]glutamate when the blood-brain-barrier was compromised [60]. Hyperpolarized [1-^{13}C]acetate, the precursor of acetylCoA, was used by Koellisch et al as a probe of carnitine acetyltransferase activity in diabetic rat heart [61]. [U-^{13}C]α-ketobutyrate has been proposed as a probe to image LDH-B activity in heart [62]. Hyperpolarized [2-^{13}C]pyruvate provides information on TCA cycle activity in addition to LDH activity [63], although it suffers from a shorter T_1. Recently, Marco-Rius et al studied glucose and fructose loading effects in the liver using hyperpolarized [2-^{13}C]dihydroxyacetone [64].

1.4. MRI

MR experiments manipulate magnetization, the macroscopic overall net magnetic moment of nuclear spins in a given volume. The original magnetization M_0 is determined by the spin density in the volume and the polarization and is given by [65]:

$$\mathrm{M}_0 = \rho\left(\frac{\gamma\hbar}{2}\right)\mathrm{Polarization} \qquad 1.3$$

M_0 points along the B_0 field direction (the longitudinal direction, or z direction in the context of this thesis). Here ρ is the number of spins per unit volume, γ is the gyromagnetic ratio and $\hbar$ is the Planck constant (in J∗s/rad). When a radio frequency (RF) oscillating magnetic field is applied in the form of a pulse (producing a B_1 field), the original z magnetization is tipped into the transverse xy plane, which is perpendicular to the B_0 field, as illustrated in Figure 1.2.

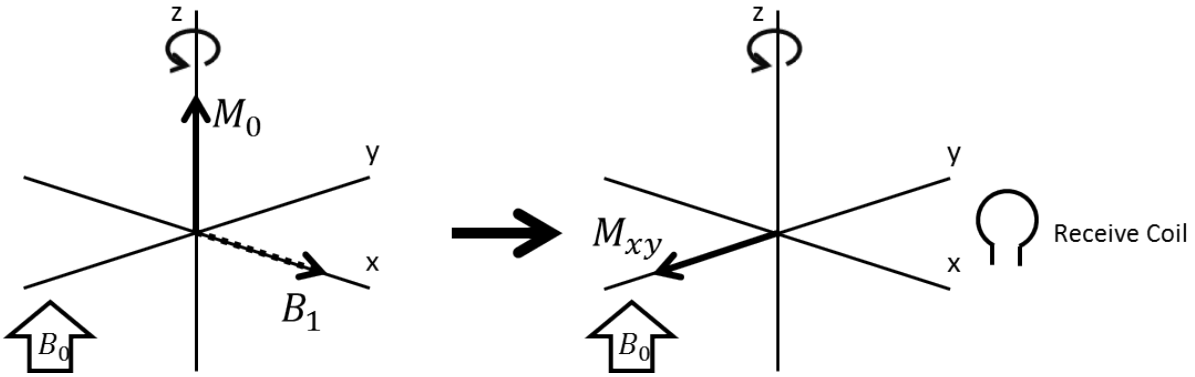

Figure 1.2: Excitation and reception of MR signal
In the presence of a static external magnetic field B_0, the original magnetization M_0 is along the B_0 field direction. An instantaneous additional B_1 field (from the RF pulse) flips the original magnetization M_0 into the transverse plane. The transversal magnetization M_{xy} then rotates about B_0 at its resonance frequency (~75 MHz for ^{13}C at 7T, for example) and generates an electric current in the receiver coil, which is positioned perpendicular to the transverse plane. The figures are plotted in the rotating frame for simplicity, which rotates about the B_0 field at the same frequency as the observed magnetization. The B_1 field should be applied at the same frequency (on-resonance with the target magnetization) to achieve an efficient flip. The figure is plotted following the right-hand rotation tradition in NMR.

Due to the fluctuation of the local field experienced by each spin, several phenomena affect the observed magnetization immediately after the excitation pulse, including spin-lattice relaxation (T_1 relaxation), spin-spin relaxation (T_2 relaxation), T_2^* decay, chemical shift, and J-coupling. MRS and MRI exploit these processes to produce signal contrast.

T_1 and T_2 relaxation

The spin-lattice relaxation, as introduced in Section 1.2, brings the longitudinal magnetization back to its thermal equilibrium value. The cause of spin-lattice relaxation is the fluctuating magnetic fields generated by the thermal motion of the molecules, which induces transitions between the spin energy states [21]. In the non-hyperpolarized case, spin-lattice relaxation means recovery of the longitudinal magnetization back to M_0, as shown in Figure 1.3A. For a hyperpolarized spin system, spin-lattice relaxation leads to decay of the hyperpolarized magnetization back to its thermal equilibrium value, as shown in Figure 1.3B. Spin-spin relaxation describes decay of the transverse plane magnetization (Figure 1.3C) due to the spins becoming out-of-phase as a result of the oscillating fields experienced by each spin, which is also the cause of the spin-lattice relaxation, and by

inhomogeneous local fields [66]. The time constants used to describe the spin-lattice and spin-spin relaxations are T_1 and T_2 respectively. Note that T_1 is determined by the transition probability between the two spin energy levels and is the same for the thermal equilibrium and hyperpolarized MRI experiments. T_1 relaxation is one of the key factors in the design of hyperpolarized MRI experiments because all the images need to be acquired before the polarization decays back to its thermal equilibrium value.

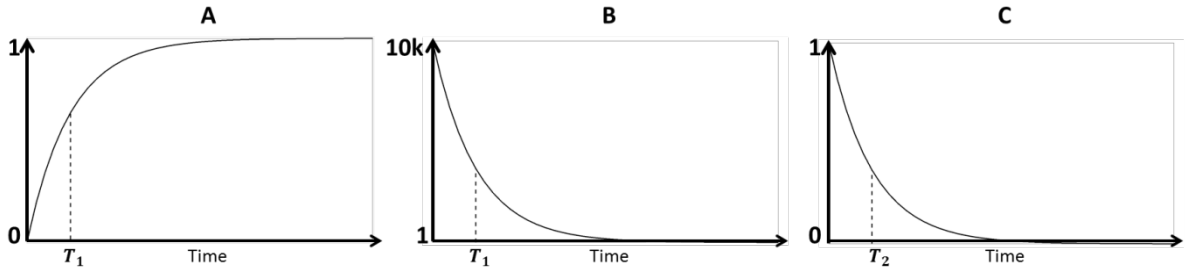

Figure 1.3: T_1 and T_2 Relaxations
(A) T1 relaxation leads to the return of the longitudinal magnetization back to M_0 in the thermal equilibrium MR experiment. (B) T_1 relaxation leads to polarization decay to M_0 in the hyperpolarized MR experiment. (C) Decay of transverse magnetization due to T_2 relaxation.

T_2^* decay

In addition to T_2 decay, transverse magnetization can be lost by a more macroscopic field inhomogeneity across an image voxel [67]. Clusters of spins experiencing slightly different magnetic fields can gradually become out of phase and signals from different clusters cancel each other. The overall magnetization decay, including the T_2 contribution, is termed T_2^* decay ($T_2^* < T_2$). Note that the macroscopic field inhomogeneity contribution to T_2^* decay could be refocused by a refocusing RF pulse. In MRI experiments, the signals are usually acquired as soon as possible after the excitation pulse in order to reduce signal loss due to T_2 or T_2^* decay.

Chemical shift

In the presence of an external magnetic field, electron currents are induced in the molecule, resulting in a change in the local field experienced by the nucleus. The same nuclei in different compounds, or at different positions in the same compound, have different local electronic environments and thus experience slightly different microscopic

local magnetic fields [21]. In a spectrum this is represented as more than one peak at different frequencies. This phenomenon is termed chemical shift. For example, in a 7 T magnetic field, the ^{13}C nucleus in [1-^{13}C]lactate is about 916 Hz from the ^{13}C nucleus in [1-^{13}C]pyruvate due to the differences in the chemical structure of these molecules. Since chemical shift is induced by the external field, it is linearly proportional to the external field strength [68]. Chemical shift is widely used to separate the signals from different molecules in MRI (for example, water and fat separation in clinical MRI [69]).

J-coupling

J-coupling describes indirect spin-spin coupling via the electrons in covalent bonds between nuclei [70]. While chemical shift is influenced by the overall local electronic microenvironment, J-coupling exists only intramolecularly, independent of the external field, but depends on the presence of other nuclear spins in the same molecule. J-coupling splits the peak of an affected nucleus and modifies its phase evolution in a MR experiment. For example, J-coupling alters the ^{13}C spectrum of [1-^{13}C]lactate, as shown in Figure 1.4.

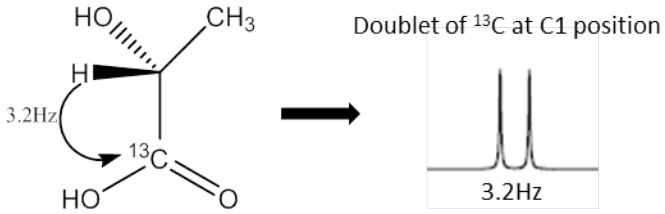

Figure 1.4: Heteronuclear J-coupling between ^{13}C and C2 position ^{1}H in [1-^{13}C]lactate
Coupling between the ^{13}C and C2 position ^{1}H splits the ^{13}C resonance into two peaks that are 3.2 Hz apart.

MRS, MRI, and MRSI

MR Spectroscopy (Figure 1.5A) acquires a spectrum from a localized volume in the study object, and the main resolution in the spectrum comes from the chemical shift. J-coupling may or may not be observed in the MRS experiment, depending on how large the J-coupling is compared to the B_0 field inhomogeneity. The MRS experiment is usually conducted in a magnetic with relatively wide bore (~12 cm for small animals and ~50 cm for human), where the B_0 field may not be very homogeneous. In MRS experiments the effects

of J-coupling can be eliminated by using decoupling pulses, which refocus the phase evolution due to J-coupling while leaving untouched the chemical shift phase evolution. MR imaging (Figure 1.5B), in contrast, acquires spatial information. MR Spectroscopic Imaging (MRSI, Figure 1.5C) maps the spatial volume into multiple voxels and acquires a spectrum at each of the voxels. The difference in these three MR techniques is in the use of magnetic field gradients, which are magnetic fields with spatially varying strength in different directions.

Gradients are generally used for three different purposes. The gradient in the slice direction, which is applied together with the RF pulse, is used to selectively excite spins in a slice and is thus termed a slice selection gradient. The gradient in a second spatial dimension applied during signal acquisition is termed the frequency-encoding gradient. The gradient used to encode the spins in the third spatial dimension, which is applied and varied between different acquisitions, is termed the phase encoding gradient. The frequency and phase encoding gradients induce different phases for spins at different spatial positions in the gradient and hence the spatial resolution of the spins arises from their spatially varying phases. In contrast, chemical shift encoding induces different phase evolutions for spins at different resonances and hence the spectral resolution of chemical shifts.

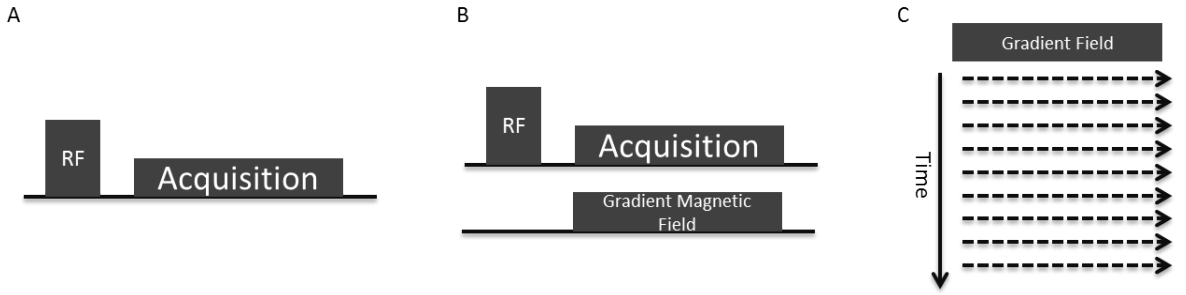

Figure 1.5: MRS, MRI, and MRSI
(A) MR spectroscopy explores the inherent chemical shift information of the study object. (B) MR imaging exploits additional spatially-varying magnetic fields to obtain spatial information from the study object. (C) A combination of chemical-shift encoding and gradient field encoding leads to MR spectroscopic imaging, providing both chemical-shift and spatial information.

For MRS the spin phase evolution is driven by the chemical shift (neglecting B_0 field inhomogeneity and J-coupling) and is given by:

$$s(t) = \int \rho(f) e^{-i2\pi tf} df \qquad 1.4$$

where s(t) is the acquired signal at time t and ρ(f) is a resonance from the imaging object at frequency f (relative to the acquisition central frequency). The exponential term describes the phase evolution caused by the offset from the central frequency. For MRI, where the frequency offset caused by the magnetic field gradient is much greater than that caused by chemical shift, the acquired signal is given by:

$$s(t) = \int \rho(\vec{r}) e^{-i\gamma t \vec{r}\cdot\vec{G}} d\vec{r} \qquad 1.5$$

where s(t) is the signal acquired at time t. $\rho(\vec{r})$ is a resonance from the imaging object at position $\vec{r}$, where $\vec{r}$ is a vector defining the spatial position. $\vec{G}$ is a vector describing the magnetic field gradients in different spatial directions. The exponential term describes the phase evolution, which is dominated in this case by the applied gradients. Signal in the MRSI experiment is given by:

$$s(t) = \int \rho(\vec{r}, f) e^{-it(\gamma \vec{r}\cdot\vec{G} + 2\pi f)} d\vec{r} df \qquad 1.6$$

where the phase of a cluster of spins depends on both its spatial location and its chemical shift.

In MRS, MRI, and MRSI, the signals s(t) are sampled in k-space. It is intuitively obvious from Equations 1.4-1.6 that the imaging object, ρ, could be recovered from k-space via a Fourier transform and the resulting image or spectrum has a resolution determined by the encoding scheme. The signal with a zero phase term is at the centre of k-space, which represents the time when all the spins are in-phase, and hence contributes the largest signal in k-space.

In reality, zero phase signal could only be acquired when a refocusing RF pulse is used because of the multiple frequency components in the imaging object. The refocusing RF

pulse flips the spins in the transverse plane about the B_1 field direction and hence reverses the phase evolution that takes place before the pulse. At the time when the phase evolution is fully reversed a spin echo is formed, and this time point is termed the Echo Time (TE). Since T_2* decay is a result of phase evolution under the influence of an inhomogeneous B_0 field, this process could be reversed by a refocusing pulse. T_2 decay, however, cannot be reversed as it involves transitions in spin energy states. In the absence of a refocusing pulse, a truly refocused echo can never be formed, and only the phase induced by gradients can be re-wound by another set of gradients, to form a gradient echo.

1.5. MR pulse sequences

A MR pulse sequence (or simply sequence in this thesis) is a series of RF pulses and gradient waveforms that excite and encode the magnetization and are used to acquire data. The sequence determines the k-space trajectory, which describes how the k-space is filled. Some sequences widely used in clinical MRI include Spin Echo (SE) [71], Fast Spin Echo (FSE) [72], Gradient Echo (GRE) [73], and Echo Planar Imaging (EPI) [74]. All these sequences acquire Cartesian k-spaces, where only a simple Fourier transform is needed for image reconstruction. Some less widely used sequences include spiral [75], radial [76], and half-radial [77], all acquiring non-Cartesian k-spaces, which are relatively computationally intensive in image reconstruction and are prone to blurring and artefacts in the reconstructed images due to the non-uniformity of k-space sampling [78-80].

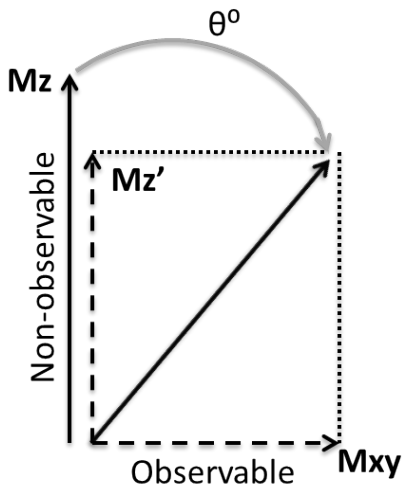

Figure 1.6: RF depletion of hyperpolarization
Each RF pulse turns part of the unobservable magnetization into observable magnetization, reducing the available hyperpolarization.

Not all clinical sequences used to image protons at thermal equilibrium are suitable for hyperpolarized MRI. A first concern in sequence design for hyperpolarized MRI is RF exposure [24]. A common workflow for all clinical sequences is that the proton magnetization is excited from its thermal equilibrium value, rotates at its Larmor frequency in the transverse plane and induces signal, while, at the same time, recovering to its thermal equilibrium value in a reasonably short period of time when it is ready for the next excitation. This is however not the case for hyperpolarized imaging, where the signal is dominated by the hyperpolarization. Hyperpolarization, as introduced in Section 1.2, is an excited state built up outside the imaging object before imaging commences. During the imaging process the polarization decays to its thermal equilibrium value in a T_1-dependent process, where it is >10000-fold smaller, yielding effectively no signal at the end of this period. In addition to T_1 decay, each excitation pulse consumes some hyperpolarization, as shown in Figure 1.6, and a 90° flip angle RF pulse depletes all the hyperpolarization. Refocusing pulses with a 180° flip angle are widely used in clinical imaging sequences to eliminate T2* decay, but their use in hyperpolarized MRI needs particular caution. While a perfect 180° pulse only inverts the polarity of the polarization, the transition bands in the frequency response of the 180° pulse can flip the polarization with any angle and hence quickly deplete the polarization. Moreover, since the B_1 field is inhomogeneous, it is

challenging to achieve a 180° flip covering all the hyperpolarized spins in the sample. Another concern in sequence design for hyperpolarized MRI is the requirement for high temporal resolution. Altered metabolism in cancer is controlled by abnormal enzyme activity, changes in which before and after treatment can be used in assessment of treatment response. A study of enzyme kinetics requires acquisition of dynamic information on metabolite labelling, which, in our case, relies on fast acquisition of metabolite images at a series of time points within a very tight imaging window that is determined by the metabolites' T_1s [24]. High spatial resolution is also needed because the heterogeneous nature of tumour metabolism means that metabolite changes may vary spatially within the tumour. The fourth concern in imaging the metabolism of hyperpolarized labelled metabolites is the need for sufficient spectral resolution. Signals from different metabolites need to be separated in the resulting images. The acquisition or excitation components of the sequence should be designed to resolve the metabolite chemical shifts.The techniques described below have been designed to match the requirements listed above.

Chemical Shift Imaging (CSI)

Chemical shift imaging [81] can be used to acquire a 2D image with a spectrum at each pixel and has been used in many hyperpolarized ^{13}C imaging studies [35,49,51,52,82]. There is no frequency encoding gradient, instead both two spatial dimensions are phase encoded, followed by signal acquisition when the spins are allowed to precess at their own frequencies in the absence of a magnetic field gradient. The main drawbacks of CSI are the slow imaging speed and the need for a relatively large number of excitations. These problems persist even if a compressed sensing technique is used [83]. Compressed sensing recovers an image from a k-space that is pseudo-randomly encoded with a reduced sampling rate [84]. Parallel imaging techniques could also be used to reduce the number of excitations by reducing the number of phase encode steps [85]. Parallel imaging replaces part of the phase encoding with the spatial encoding that is inherent in a multichannel phased array receive coil [86-88]. The CSI sequence is depicted in Figure 1.7.

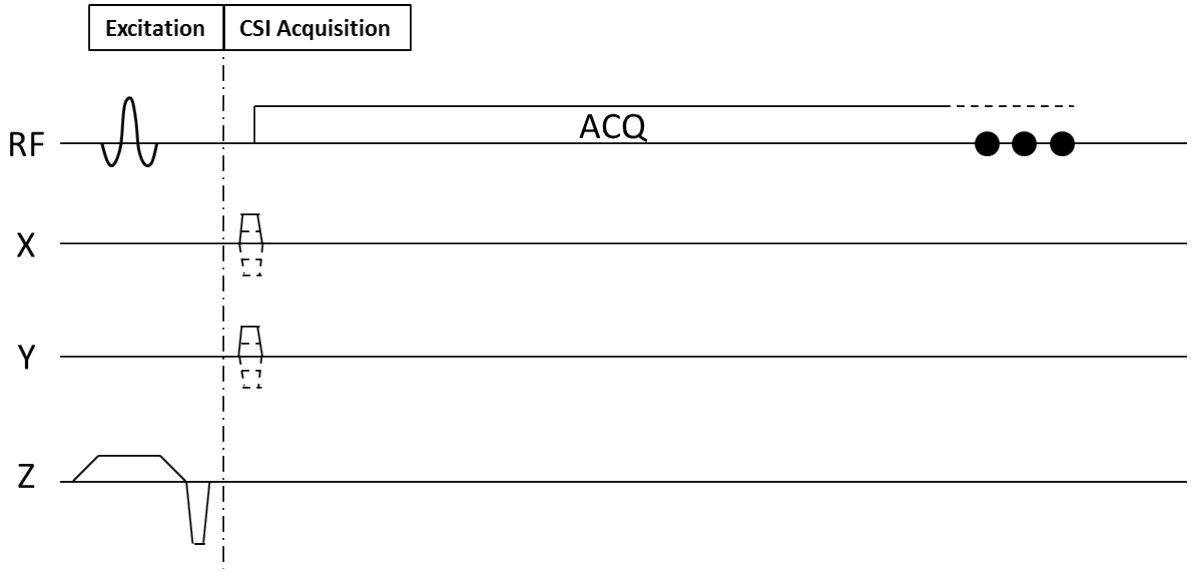

Figure 1.7: Schematic plot of CSI sequence
A representative CSI sequence. Phase encoding gradients on both X and Y axes are used, following excitation with a slice selective sinc pulse.

Echo Planar Imaging

Echo planar imaging is widely used in clinical proton imaging because it is fast, acquiring a 2D k-space in a fraction of second. A consequent benefit is its insensitivity to motion. Both benefits can be exploited in hyperpolarized ^{13}C imaging, where high speed imaging is needed to achieve a high temporal resolution and motion insensitivity is desirable as it suppresses the potential imaging artefacts arising from perfusion of the injected imaging agent. Another property of EPI is the low RF pulse exposure, the acquisition of a 2D image requiring only a single RF pulse, which is beneficial for preservation of the polarization.

MRI needs to balance imaging time and image quality. The EPI sequence, as a fast imaging technique, suffers from two major problems. One concern with EPI is image distortion in the phase encoding direction, resulting from a low sampling rate in the presence of B_0 field inhomogeneity [89]. The same kx position in each ky line is sampled every echo, where adjacent echoes are usually a few milliseconds apart. B_0 field inhomogeneity, either endogenous or from eddy currents [90], induces extra phase accumulation during each echo spacing, leading to mis-encoding of the spin locations and

hence image distortion. For hyperpolarized MRI, an intuitive workaround to limit image distortion is to reduce the echo spacing. Alternatively, Geraghty et al used a dual-echo EPI sequence where a phase error map could be calculated to correct for image distortion [91]. Cunningham et al, on the other hand, removed image distortion with two acquisitions where blipped gradients were of opposite polarity and where the resulting distortions were in opposite directions [92].

Another major concern in EPI is Nyquist ghosting. The bi-polar readout gradients result in bi-polar eddy currents and hence opposite phase errors in odd and even k-space lines, leading to Nyquist ghosts in the result image [93]. Nyquist ghosting is also called a FOV/2 ghost because it appears as the imaging object shifted by FOV/2, in addition to the object at its original position. In proton imaging at thermal equilibrium, this ghosting is usually corrected by acquiring a separate reference scan, where the phase encoding gradients are turned off [94,95]. This approach, however, is less preferable in the case of hyperpolarized MRI as it sacrifices a time point for either one or more of the metabolites, which is particularly undesirable for metabolites with short T_1 and hence limited imaging window. A workaround is to acquire a few reference echoes in the same imaging sequence before the regular readout train [96,97]. However, this may decrease the SNR as a result of the prolonged TE and hence is less preferable for metabolites with short T_2s. Cunningham et al proposed an asymmetric design for the readout gradient [98,99], where all the signals are acquired with the same gradient polarity and ghosting is naturally avoided [100]. This method was also adopted by Koelsch et al [101] and Marco-Rius I et al [102] in their studies. By doing this, however, the echo spacing is prolonged as the signal is now acquired at every two gradient lobes, introducing extra image distortion. Due to this decrease in imaging efficiency, the SNR is also reduced with an extended length of the readout train. In light of this, Gordon et al acquired the reference scan on the ^{1}H signals at thermal equilibrium, calculated the phase correction coefficients, and then applied them to the correction of the hyperpolarized ^{13}C images [103].

EPI can also suffer from image blurring due to signal decay throughout the echo train, which is equivalent to low-pass windowing in k-space [104]. This is fortunately less of a concern in hyperpolarized MRI as the echo train is usually shorter than in regular MRI.

EPI is usually used together with Spectral-Spatial (SpSp) selective pulses to selectively excite a specific spectral component in a specific slice [105], otherwise components with different chemical shifts can lead to their mis-position in the resulting images, as was explained above in the introduction to distortion artefacts. However, sometimes hyperpolarized ^{13}C EPI has also been used with multiband SpSp pulses, which can simultaneously excite metabolites with different resonance frequencies [106]. For example, Geed et al simultaneously imaged [1-^{13}C]pyruvate and [1-^{13}C]lactate using EPI and then separated the two metabolites by exploiting their different locations in the resulting image resulting from their different chemical shifts [107]. This method was extended by Shin et al to incorporate parallel imaging algorithms in the separation of multiple metabolites signals [108].

A typical 2D EPI sequence is depicted in Figure 1.8 below, and this could be extended into a 3D sequence by adding extra phase encoding in the Z direction [97].

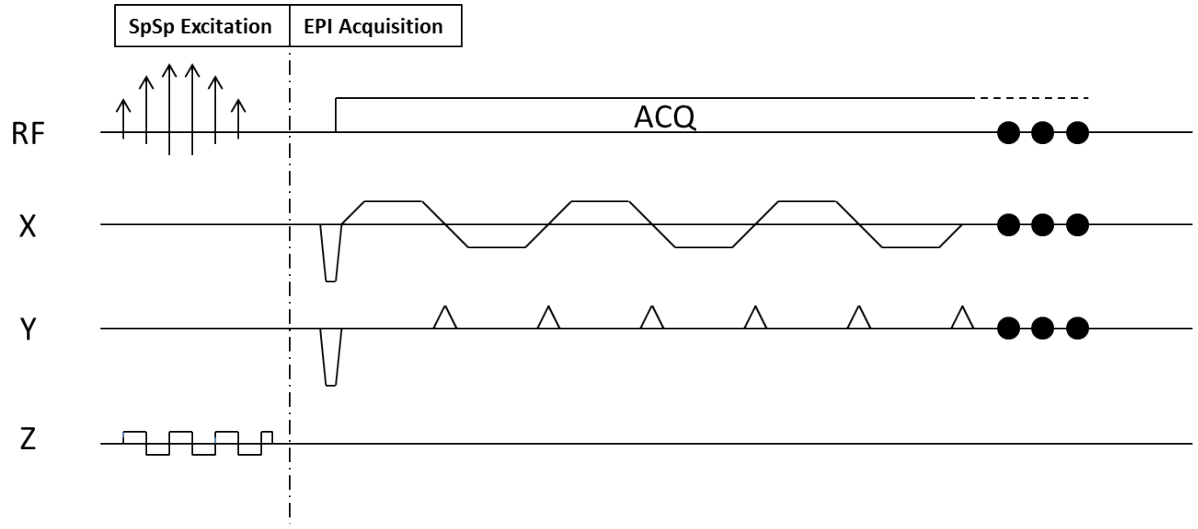

Figure 1.8: Schematic plot of EPI sequence
A representative 2D EPI sequence. A SpSp pulse is used to excite the target metabolite resonances, and the excited magnetizations are then encoded in two dimensions after a single excitation.

Echo Planar Spectroscopic Imaging (EPSI)

While EPI acquires an image with only spatial dimensions, EPSI acquires an image with a spectrum in each voxel [109]. The EPSI sequence was introduced by Sir Peter Mansfield

and his colleagues, originally named as PEEP (Phase-Encoded Echo-Planar) [110], together with two forerunners of this sequence that were proposed earlier by the same group [111]. Blipped gradients in the Y direction are replaced with regular phase encoding gradients before the readout gradient train, leaving signals in the latter encoded by their chemical shifts. EPSI has been used in hyperpolarized MRI to simultaneously map the signals from multiple metabolites [98,106,112-114]. The benefit of this technique over EPI with SpSp pulses is that it does not require prior knowledge of the metabolites, as all the resonances in the spectrum can be resolved. However, this benefit is degraded by the bandwidth of the acquired spectrum, which is usually a few hundred Hertz and is limited by the echo spacing in the readout train. This could result in a folded spectrum, where metabolites with relatively large chemical shifts are wrapped around to give an incorrect location. In addition, regular phase encoding in the Y direction leads to multiple excitations to cover a full k-space in that direction, which makes it less desirable as each excitation consumes hyperpolarization. This problem is exacerbated when the technique is extended to 3D EPSI (3D spatial 1D spectral imaging), where another set of phase encoding gradients are required in the 3rd spatial dimension. Hence, compressed sensing is usually used in conjunction with 3D EPSI [115-117] to reduce the number of excitations and further accelerate imaging speed. Another solution to the demanding number of excitations is to use parallel imaging, where the number of phase encode steps could be reduced based on the number of receiver channels present [118-120]. Parallel imaging with EPSI may further benefit from a calibrationless technique described by Shin et al [121]. Calibration information is difficult to acquire in hyperpolarized ^{13}C MRI due to the sparse nature of the signal. Although it has been proposed [122], parallel imaging may not be of significant benefit to hyperpolarized EPI, because phase encoding in EPI can be achieved with a train of blipped gradients following a single excitation pulse. EPSI sequences have already been applied in clinical experiments with hyperpolarized [1-^{13}C]pyruvate in prostate [27,29]. A typical 2D EPSI sequence is illustrated in Figure 1.9.

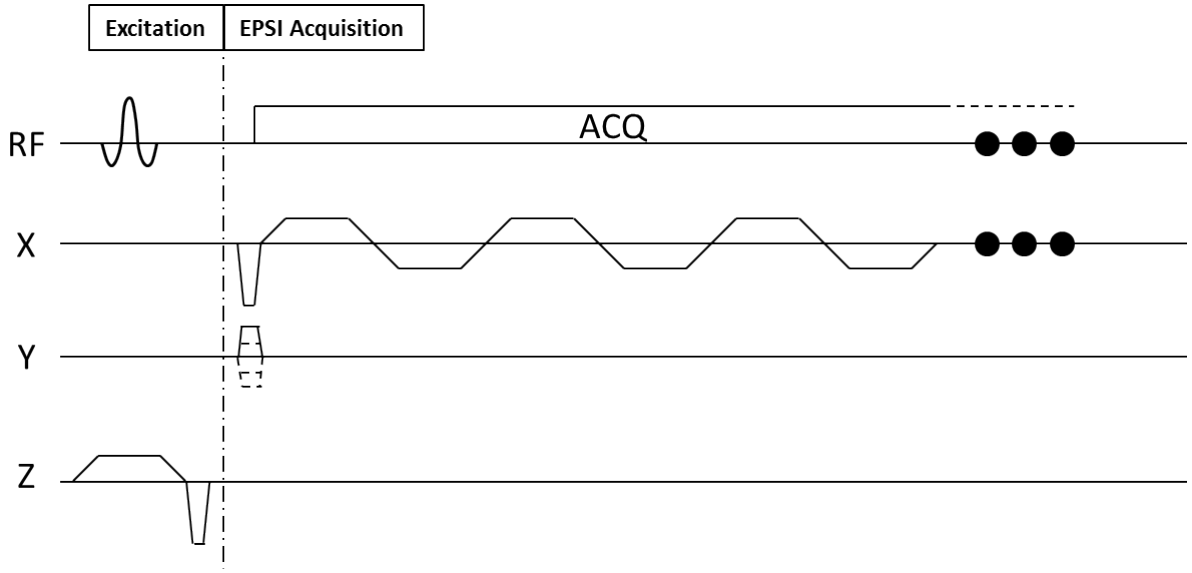

Figure 1.9: Schematic plot of EPSI sequence
A representative 2D EPSI sequence. Compared to EPI, a blipped gradient train on the Y axis is replaced with a set of step-wise phase encode gradients, each step requiring an extra excitation. Similar phase encoding could be added to the Z axis to acquire a 3 dimensional image. Chemical shift encoding takes place in the readout gradient train on the X axis.

Spiral based sequences

While all the sequences above acquire a Cartesian k-space, the spiral based sequences acquire signal to fill a spiral k-space [123]. Spiral trajectories cover k-space in a more SNR efficient way when compared to EPI because they sample the centre of k-space more densely, where most of the signal is located [124]. This benefit can be further enhanced by using a variable density spiral trajectory [125-128]. Compared to EPI, spiral trajectories have even faster switched gradients. The resulting eddy currents, together with B_0 field inhomogeneity, can result in image rotation and blurring. However, these can usually be corrected retrospectively using measured B_0 maps or k-space trajectories [129-131]. Variable density spirals, when under-sampled in outer k-space, can introduce aliasing artefacts that appear as streaks and swirls in the image [124], which are different from the wrap-around artefacts observed when a Cartesian k-space is acquired.

Since a 2D k-space can be covered after a single excitation, spiral sequences are also widely used in hyperpolarized MRI. Lau et al used a single-shot spiral acquisition to image [1-^{13}C]pyruvate and ^{13}C bicarbonate in the heart, where the metabolites were excited

alternately using SpSp pulses [132]. Spiral readouts preceded by motion-sensing gradients can be used to image metabolites within target tissues while suppressing signals from blood vessels [133-135]. The single-shot 2D spiral acquisition can be extended to 3D imaging by phase encoding on the third dimension, one excitation per phase encoding step [46]. A spiral CSI sequence [136] can be used to acquire spectra at each image voxel, where a train of spirals is acquired after a single excitation, such that each spiral encodes a 2D image and all the spirals in total are chemical shift encoded. A similar sequence has been used extensively by Meyer and colleagues for hyperpolarized ^{13}C MRI as a 2D spatial and 1D spectral dataset could be acquired in less than a second following a single excitation [137-142]. The benefit of spiral CSI over EPSI is that there is no need for multiple excitations, while the drawback is a narrower spectral bandwidth, which is limited by the duration of each spiral. Another way of acquiring spectral information is to use the Dixon method [143-145], where, instead of acquiring a full spectrum, a few echoes (spirals) are acquired at different echo times to resolve a known number of resonances. This method has been adopted in hyperpolarized ^{13}C MRI to acquire extremely simplified spectra for known metabolites [61,146-148]. A potential problem is signal contamination from unexpected metabolites that were not included in the image reconstruction. Outlines of the spiral and spiral CSI sequences are depicted in Figure 1.10.

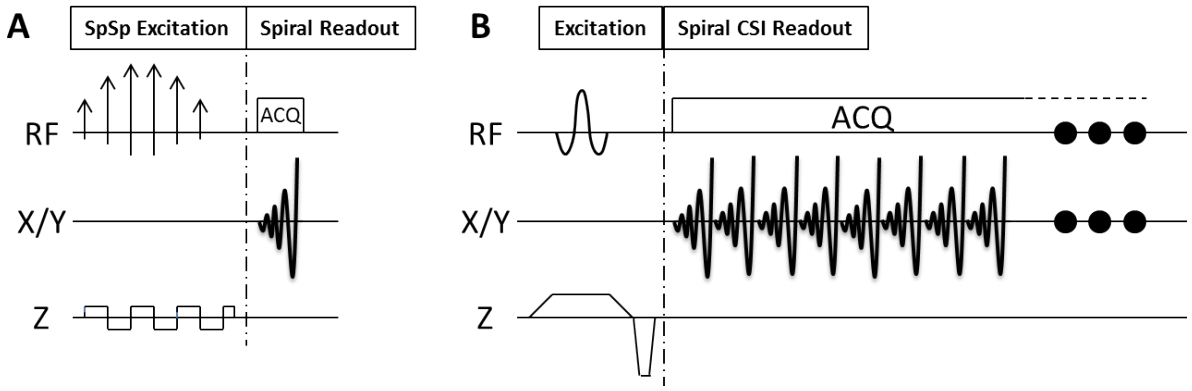

Figure 1.10: Schematic plot of spiral and spiral-CSI sequences
Spiral sequence families. (A) Spiral sequence for single metabolite with spectral-spatial excitation. (B) Spiral CSI sequence to map multiple metabolites with spectral resolution. A Spiral Dixon sequence could simply replace the slice-selective excitation in (B) with a multi-band SpSp pulse and add the desired delays between the subsequent spiral readouts in order to obtain chemical shift information.

Other imaging trajectories

Although less popular, some other imaging sequences have also been used for hyperpolarized ^{13}C MRI experiments, including the examples given below. Leupold et al exploited the balanced Steady-State Free Precession (bSSFP) sequence to image the hyperpolarized ^{13}C metabolites based on their chemical shifts [149]. This technique was expanded to 3D fast mapping by Shang et al [150]. The principle behind these techniques is that a train of RF excitation pulses excite resonances at certain frequencies while others are saturated. A drawback is the possibility of excitation of unwanted metabolite resonances by the replicating excitation bands as well as the transition bands, as the frequency response profile of the RF train is much worse than for a regular SpSp pulse. Another concern is the large number of excitation pulses used to build up the pseudo-steady state signals as well as to acquire the 2D and 3D images. Laustsen et al used a radial FSE sequence with sinc refocusing pulses for T_2 mapping of ^{13}C urea in diabetic kidney [151]. Although a radial FSE sequence enables fast T_2 mapping [152], the imperfect refocusing pulses may deplete the polarization very quickly. Ramirez et al modified EPSI to cover k-space with a radial trajectory [153]. This design has higher SNR efficiency when compared to Cartesian k-space EPSI because each excitation leads to an acquisition that crosses the centre of k-space. The downside is that each radial spoke requires an excitation, resulting in considerable RF

exposure. To minimize RF exposure, Frydman and colleagues acquired 2D spatial and 1D spectral information after a single excitation [154] using spatiotemporal encoding, however this naturally resulted in a low SNR.

1.6. Aim

The fundamental challenge in hyperpolarized ^{13}C MRI is to obtain high spatial and temporal resolution from a signal that decays relatively rapidly and is depleted by excitation. The aim of my PhD project was to develop imaging techniques for hyperpolarized ^{13}C-labeled metabolites that can improve on the current state-of-the-art in one or more of these aspects.

2. A single shot 3D sequence for hyperpolarized ^{13}C MRI

2.1. Introduction

As introduced in Chapter 1, the enormous gain in spin polarization afforded by dissolution Dynamic Nuclear Polarization has enabled dynamic measurements of tissue metabolism in vivo using ^{13}C magnetic resonance spectroscopic imaging following intravenous injection of hyperpolarized ^{13}C-labeled substrates. Measurements of the labeled substrates and their products can be used to measure various metabolic fluxes and enzymatic processes. However, this is demanding in terms of imaging speed due to the short lifetime of the hyperpolarization. In addition, heterogeneity is an intrinsic property of tumours [155], and can be directly correlated with the effectiveness of treatment [156]. Three-dimensional imaging is desirable, therefore, both to investigate tumour heterogeneity and to fully monitor the response of a tumour to treatment. In Chapter 1 I reviewed the fast imaging techniques in the literature for hyperpolarized ^{13}C MRI. An inherent limitation of the imaging techniques described above is that, for full 3D coverage, they require several excitations for each image, which will deplete the polarization and thus accelerate signal decay. This is the case for 3D imaging techniques, where an extra excitation is required for each phase encoding step in the slice direction and is also true for 2D imaging techniques, where slice cross-talk, due to an imperfect excitation profile, can accelerate polarization decay. I have developed a novel single-shot 3D imaging sequence with SpSp excitation and a hybrid dual-spin-echo-spiral readout. The sequence was designed to minimize loss of polarization by reducing the number of excitation pulses required, while maintaining high spatial and temporal resolutions. The sequence was demonstrated on both phantoms and mice and its robustness to B_0 field inhomogeneity, a common challenge for fast imaging techniques, was also demonstrated theoretically.

2.2. Methods

Tumour model

Animal experiments were performed in compliance with a project license issued under the Animals (Scientific Procedures) Act of 1986. Protocols were approved by the Cancer

Research UK, Cambridge Institute Animal Welfare and Ethical Review Body. Female C57BL/6J mice were injected subcutaneously in the lower flank with $5x10^5$ EL4 lymphoma cells. The tumours were allowed to grow for 8-11 days, when they achieved a size of 1-1.7 cm in diameter. The mice were fasted for 6-8 hours before imaging [157]. Tumour-bearing animals were prepared by Richard L. Hesketh and De-en Hu.

Hyperpolarized [1-^{13}C]pyruvate

The sample contained 44 mg [1-^{13}C]pyruvic acid (CIL, Tewksbury, MA, USA), 15 mM OXØ63 (GE Healthcare, Amersham, UK) and 1.4 mM gadoterate meglumine (Dotarem; Guerbet, Roissy, France) and was hyperpolarized using a Hypersense Polarizer (Oxford Instruments, Abingdon, UK) at 1.2 K in a magnetic field of 3.35 T, with microwave irradiation at 94.126 GHz. The sample was then rapidly dissolved in 6 mL buffer containing 40 mM Tris, 185 mM NaOH and 100 mg/L EDTA heated to 180 ^{o}C and pressurized to 10 bar.

MRI scanner

Experiments were performed at 7 T (Agilent, Palo Alto, CA). The maximum gradient strength was 0.4 T/m and slew rate 3000 T/m/s. A 42 mm diameter bird-cage volume coil for ^{1}H transmission and , with an integrated quadrature-bird-cage (42mm) volume coil for ^{13}C detection were used (Rapid Biomedical GMBH, Rimpar, Germany).

Spectral-spatial pulse

The SpSp pulse (Figure 2.1A) was designed to detect [1-^{13}C]pyruvate and [1-^{13}C]lactate, without disturbing the polarization of alanine and pyruvate-hydrate. The pulse had a bandwidth at half maximum of 350 Hz and the centre-centre distance between the excitation bands of 1645 Hz (Figure 2.1B). The pulse design followed the small tip-angle approximation [158] to give a flip angle of 15^{o} with a peak B_1 of 21.85 μT. The flip angle could be increased to 90^{o} when a peak B_1 of 131.11 μT was used (Figure 2.1C). The RF profiles in the spectral and the spatial dimensions were designed using the SLR algorithm [159]. The pulse duration was 10.056 ms and the sampling time for both RF and gradient waveforms was 4 μs. Since the pulse was designed for 3D imaging, it relaxed the design demands on minimum slice thickness, which was set to 1.2 cm to leave more flexibility in

other parameters, such as sub pulse excitation profiles and spectral stopband width. Simulations showed a full width at half maximum (FWHM) for the RF response of 1.3 cm. A fly-back design enhanced the pulse's robustness to system imperfections, where only the positive gradient lobes, at maximally 0.19 T/m, were accompanied by the RF sub pulses. The negative gradient lobes were designed to have the smallest duration, with a maximal gradient strength of -0.29925 T/m. The sub pulse had a time-bandwidth product of 6. For the spectrally selective pulse this was 3.52. The RF pulse and gradient waveforms were generated using custom-written Matlab (The Math Works, Natick, MA, USA) scripts.

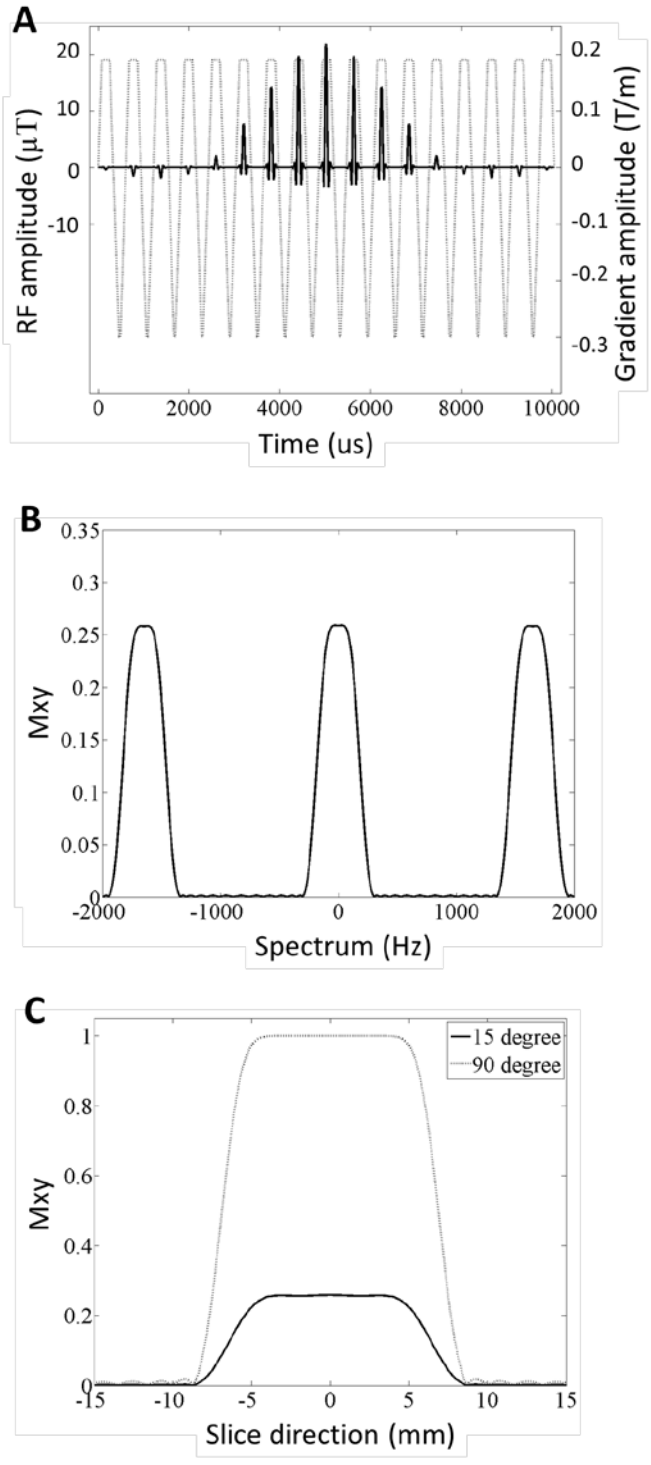

Figure 2.1: SpSp pulse design

Spectral-Spatial excitation pulse to excite alternately the [1-^{13}C]pyruvate and [1-^{13}C]lactate resonances. (A) RF profile (in μT) and oscillating slice selection gradient (in T/m). (B) Frequency response (15° at 0Hz). (C) Slice profiles for 15° and 90° flip angles. Note that although the design target of the pulse was 15°, the quality of the excitation profile was maintained for the 90° flip angle pulse.

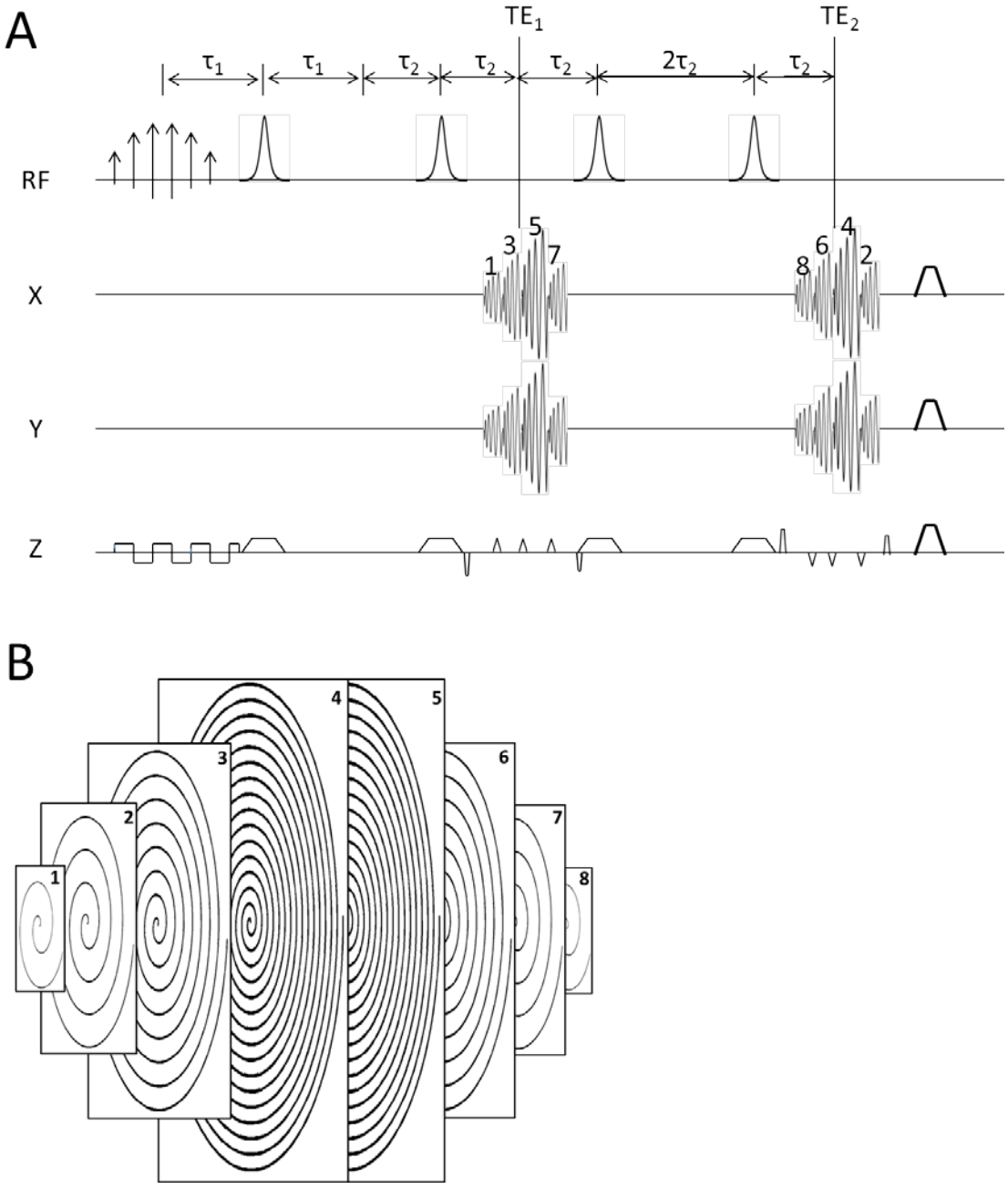

Figure 2.2: Single-shot 3D sequence

The pulse sequence (A) and its 3D k-space trajectory (B). The pulse sequence includes a spectral-spatial excitation pulse and two pairs of adiabatic inversion pulses. All phase encoding steps in the z-direction were completed after a single excitation by using blipped gradients. Two spin echoes were acquired in two groups of spiral readouts, resulting in dual-T_2 weighted contrast. The gradients within each acquisition interval were self-refocused, and the sequence ends with spoiler gradients along all three axes. The whole of k-space was acquired as a stack of interleaved spirals. The 1^{st}, 3^{rd}, 5^{th}, and 7^{th} spirals were acquired in the first group, while the 8^{th}, 6^{th}, 4^{th}, and 2^{nd} spirals were acquired in the second group. The kx-ky matrix size is larger in the centre of the kz-direction and smaller in the peripheral planes, resulting in a spherical 3D k-space.

Pulse sequence

The pulse sequence (Figure 2A) acquires a spherical stack of spirals in 3D k-space (Figure 2B), such that each kx-ky plane has a spiral-out trajectory. Two groups of 4 spirals are acquired, where the 4 spirals in the first group acquire data for the 1^{st}, 3^{rd}, 5^{th}, and 7^{th} positions in the kz-direction, while the second group acquires the 8^{th}, 6^{th}, 4^{th}, and 2^{nd} positions. For spirals 1 to 8, the corresponding Cartesian matrix sizes were 4 x 4, 8 x 8, 16 x 16, 32 x 32, 32 x 32, 16 x 16, 8 x 8, and 4 x 4, respectively. The duration of the 4 x 4, 8 x 8, 16 x 16, and 32 x 32 spirals (including the rewinding gradients) were 0.656, 1.344, 3.240, and 8.580 ms respectively and were designed to achieve the same field-of-view (FOV) [160]. To encode spatial information in the slice direction, each blip between spirals traverses two steps in the kz-direction. There are pre- and re-phasing gradients so that the z-axis gradient, in each acquisition interval, is self-refocused. Since each spiral is also self-refocused on the x and y axes, the encoding gradients on all 3 axes are fully balanced in each acquisition interval.

Imperfect refocusing pulses, due to B_0 and B_1 field inhomogeneity, can deplete the polarization very quickly. Therefore adiabatic pulses with a Hyperbolic-Secant (HS) profile were used. Since a single HS adiabatic inversion pulse would leave a non-linear phase across the swept frequency band, this requires the HS pulse to be played out in pairs, hence the sequence shown in Figure 2A. For the spiral trajectory in Figure 2B, τ_1 was 10 ms and τ_2 was 15 ms. The two central spirals (4^{th} and 5^{th}) were acquired at the time of the spin-echo so that the centre of k-space was free from the effects of B_0 field inhomogeneity. This resulted in 2 TE times, where TE_1 was 50.6 ms and TE_2 was 110.504 ms. Spoiling gradients on all three axes at the end of the sequence de-phase residual transverse magnetization.

The pulse sequence can be adapted to other k-space trajectories, depending on the required resolutions in the xy plane and z-direction. Two alternative designs were tested. A 16x16x8 design (compared to the original 32x32x8 design) consisted of 8 spirals (again 2 sets of 4) where each had a 16x16 matrix in the xy plane. In the second design (16x16x12), 12 spirals were divided into 2 groups to achieve 12 phase encoding steps in the z-direction, while each spiral encoded a 16x16 matrix in the xy plane. In these alternative designs the

overall 3D k-spaces are cylindrical, in contrast to the more-spherical k-space in the original sequence.

Theoretical Point Spread Functions (PSF), ignoring relaxation, were simulated as described by Durst et al [161]. A constant k-space was sampled by each of the proposed acquisition schemes and a 3D Fourier transform was performed to yield the PSFs. The sampled k-spaces were zero-filled (32x32x8 to 512x512x128, 16x16x8 to 512x512x256, 16x16x12 to 512x512x384) before Fourier transform.

Phantom imaging

All three sequences were tested on a cylindrical phantom (7 mm inner-diameter) filled with thermally polarized 8.5M [1-^{13}C]lactate. For each design, a series of FOVs in the z-direction (16 mm, 20 mm, 24 mm, 32 mm, and 40 mm) were acquired to determine the slab profile. The nominal in-plane resolutions were 1.25 mm, 2.5 mm, and 2.5 mm for the 32x32x8, 16x16x8 and 16x16x12 designs, respectively. The nominal slice thickness could be calculated as the z-direction FOV divided by the number of phase encoding steps. The SpSp pulse was increased to a flip angle of 90^{o} to excite a slab of 13 mm in all phantom experiments. Each acquisition was accompanied by a reference image in which the encoding gradients on the z axis were turned off.

T_2 weighted proton images were acquired with a FSE sequence, to provide a positional frame of reference, with a FOV of 40 mm and matrix size 256 x 256, with 8 slices covering 20 mm in the z-direction.

Dynamic imaging in vivo

Pyruvate and lactate images were acquired in alternating order and 30 pairs of images were acquired in total (60 s total acquisition time). The excitation pulse was set alternately at the pyruvate and lactate resonance frequencies. Each pair of acquisitions were 1 second apart, to give a 'frame rate' of one every 2 s per metabolite. The z-axis blipped gradients and their pre-phasing and rewinding gradients were turned off for the 8th pair of acquisitions and the data used as a phase-reference. Hyperpolarized [1-^{13}C]pyruvate was injected after the first image was acquired. A flip angle of 15^{o} was used for pyruvate and 90^{o} for lactate so

that the lactate acquisition followed a saturation-recovery scheme [162]. The FOV in the xy plane was 40 mm, with a matrix size of 32 x 32. The FOV in the z-direction was 20 mm, resolved into 8 pixels. The nominal spatial resolution was therefore 1.25 x 1.25 x 2.5 mm^3. The nominal excitation slab thickness was 13 mm, smaller than the z-direction FOV, in order to avoid image wrap-around in the z-direction. The frequencies of the selective excitation pulses were calculated from the measured water proton frequency, based on prior measurements of the [1-^{13}C]lactate, [1-^{13}C]pyruvate and water proton resonance frequencies. The [1-^{13}C]pyruvate resonance frequency was at -916 Hz from the [1-^{13}C]lactate resonance frequency.

T_2 weighted proton images were acquired for positional reference. These were 40 x 40 mm^2 (256 x 256) FSE images with a slice thickness of 2.5 mm. 2D spoiled gradient echo proton images with varying TEs (1.6, 1.7, 1.8, and 1.9 ms, respectively) were also acquired with the same FOV and slice thickness, and a matrix size of 32 x 32. A 3D phase unwrap was applied across the xy plane and the slice axis and the phase maps converted to a ΔB_0 map based on the differences in TE. These were used to estimate the B_0 field homogeneity in the imaging volume of the hyperpolarized ^{13}C experiment.

Image reconstruction

A phase correction was performed, similar to that described in [163]. Inter-spiral phase variations were measured by comparing the leading data points between spirals in the reference scan. The measured phase variations were then subtracted from the regular imaging spirals. Corrected data for each spiral were gridded onto a Cartesian plane [79], and a 3D Fourier transform was applied. Phase correction and image reconstruction were performed in Matlab.

2.3. Results

Proton images, and ^{13}C images acquired using the pulse sequence designs described in the methods section, of a [1-^{13}C]lactate-containing phantom, are shown in Figure 2.3. The ^{13}C images appear less homogeneous due to the use of a surface receive coil. Since the ^{13}C

excitation slice thickness was only 13 mm, smaller than the 20 mm FOV in the z-direction, the signal drops off towards the ends of the phantom.

The slab profiles for a series of FOVs in the z-direction, for all three spiral trajectory designs, are presented in Figure 2.4. These represent the combined effects of the excitation pulse, receive coil sensitivity profile, and the encoding schemes in both the xy plane and z direction. While both the 16x16x8 and 16x16x12 designs more closely resemble the excitation profile than the 32x32x8 design, the difference is small and is probably due to the more spherical shape of the 3D k-space in the 32x32x8 design. All three acquisition schemes produced an acceptably accurate image of the excited signal in the z-direction. The theoretical point spread functions are shown in Figure 2.5.

Dynamic hyperpolarized ^{13}C images were acquired from three tumour-bearing mice using the 32x32x8 design. Figure 2.6A shows representative [1-^{13}C]pyruvate images of the 4^{th} slice overlaid on a T_2 weighted ^{1}H image; Figure 2.6B shows the corresponding [1-^{13}C]lactate image. The [1-^{13}C]pyruvate and [1-^{13}C]lactate images from all the slices at 6 s and 7 s are shown in Figures 2.6C and 2.6D, respectively. The artefacts in the lactate images at 1 and 3 s were due to some excitation of the very intense pyruvate signal in the aorta of this animal (Figure 2.6B). These artefacts were not observed in the images from the other two mice.

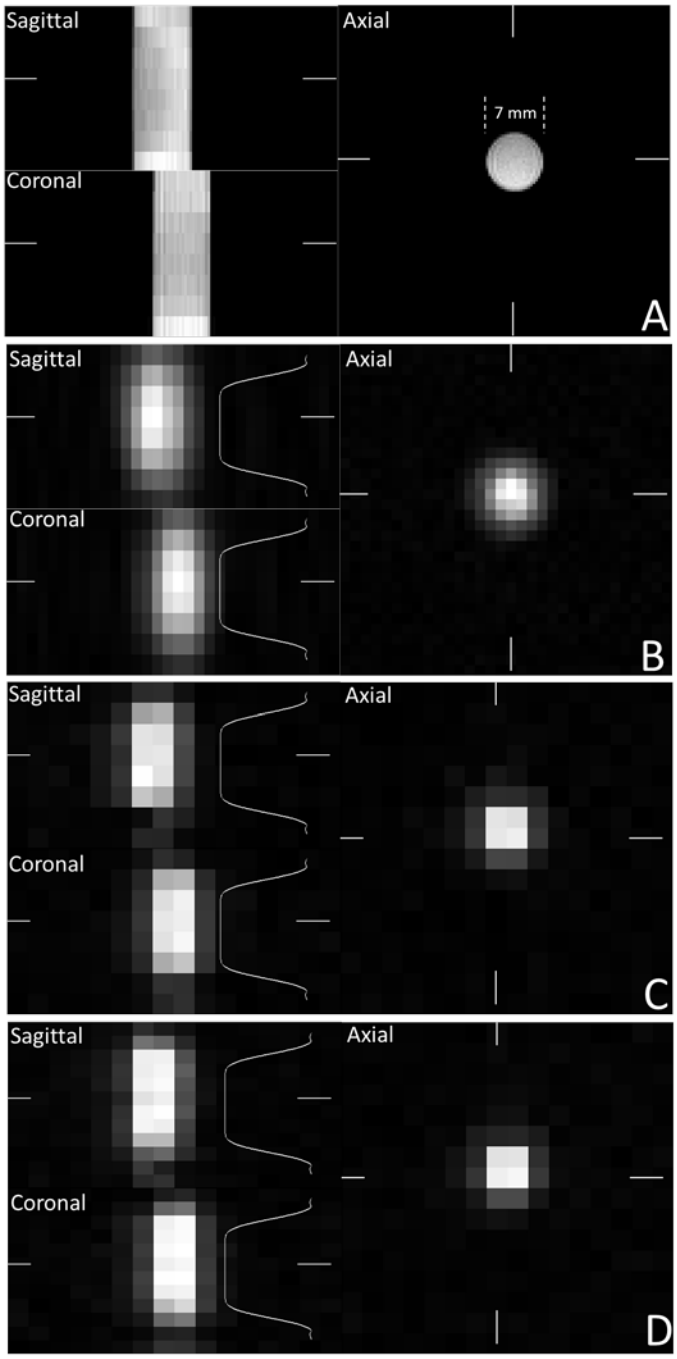

Figure 2.3: Phantom images with single-shot 3D sequence
^{1}H and ^{13}C images (FOV of 40 x 40 x 20 mm^{3}) acquired from a cylindrical phantom (inner diameter 7 mm) containing 8.5 M [1-^{13}C]lactate. Proton T_2 weighted images (A). ^{13}C images acquired using the 32x32x8 sequence (B), 16x16x8 sequence (C), and 16x16x12 sequence (D). The white bars at the periphery of the images relate the position of the sagittal and coronal slices to the displayed axial slice. The white curves in the sagittal and coronal views of the ^{13}C images indicate the excitation profile and its location.

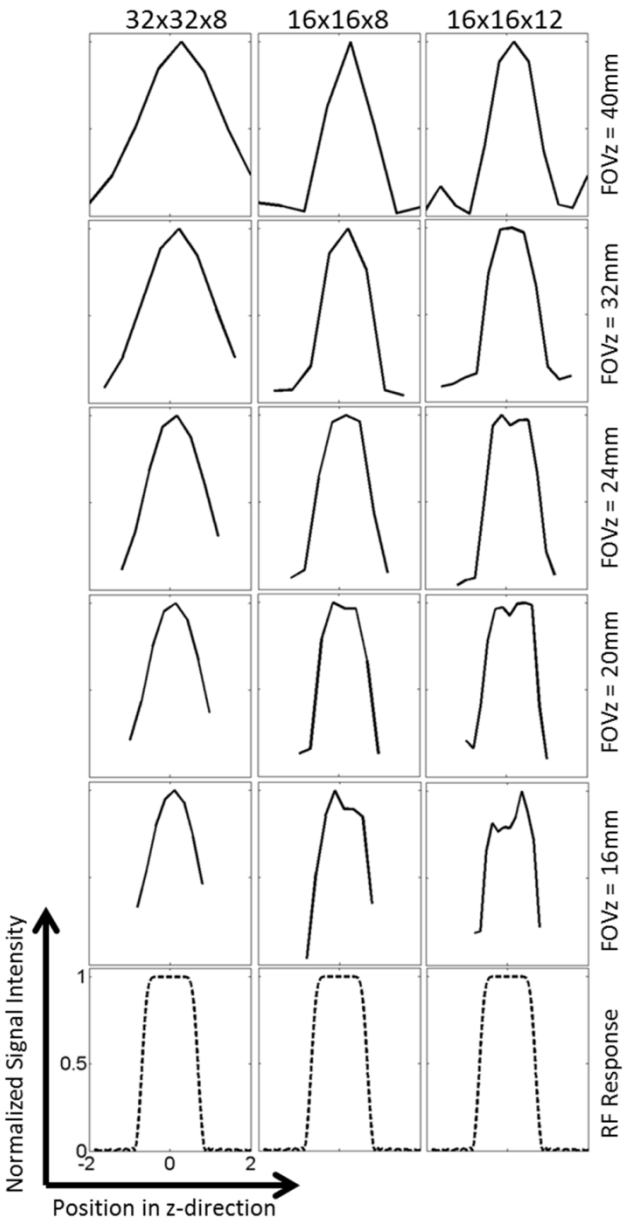

Figure 2.4: Measured slab profile

Slab profiles for a series of FOVs in the z-direction for the three k-space trajectory designs, compared to the simulated excitation pulse response. The slab profiles were obtained by summing signal intensities over the xy plane for images at each z position for each 3D dataset. For each subplot, the horizontal axis represents position in the z-direction, in centimetres, and the y axis represents the signal intensity normalized to the maximum value.

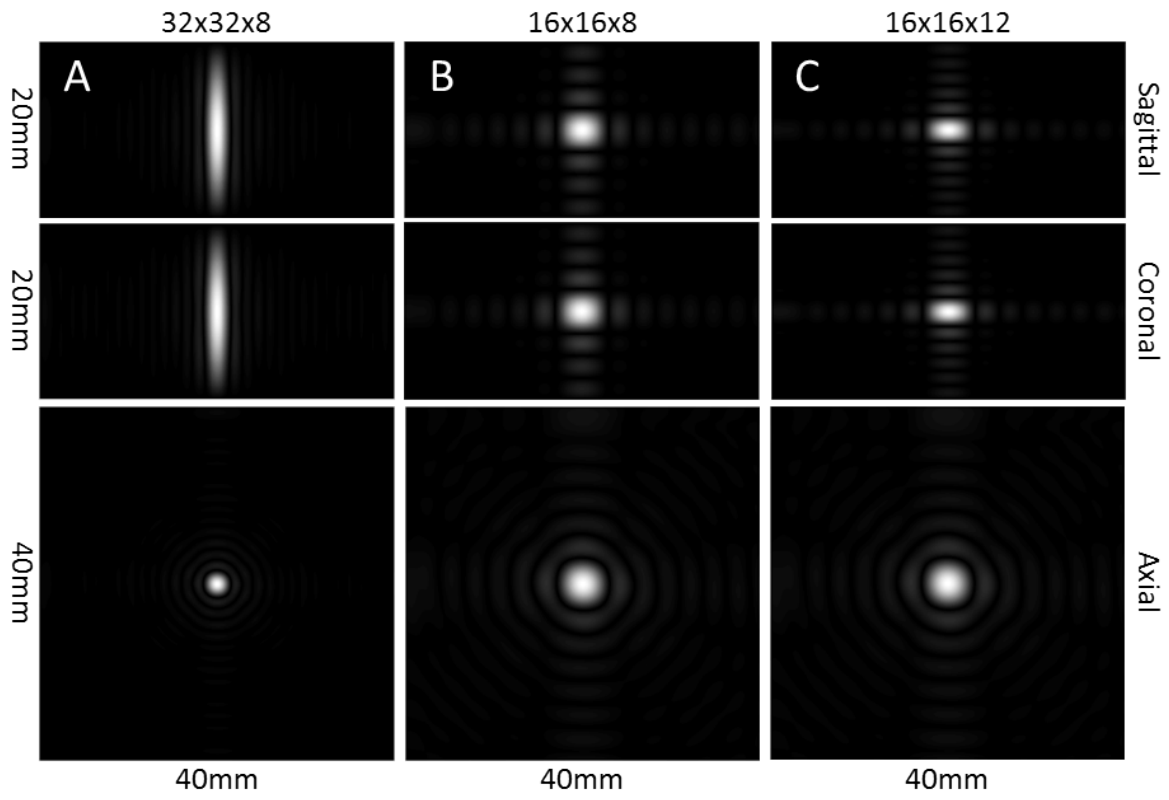

Figure 2.5: PSFs of different trajectory designs

3D point spread functions for sagittal, coronal and axial views for the 32x32x8 (A), 16x16x8 (B) and 16x16x12 (C) designs. The PSF of the 16x16x12 design shows a sharp improvement in the z-direction when compared to the 32x32x8 design, at the expense of reduced xy plane resolution.

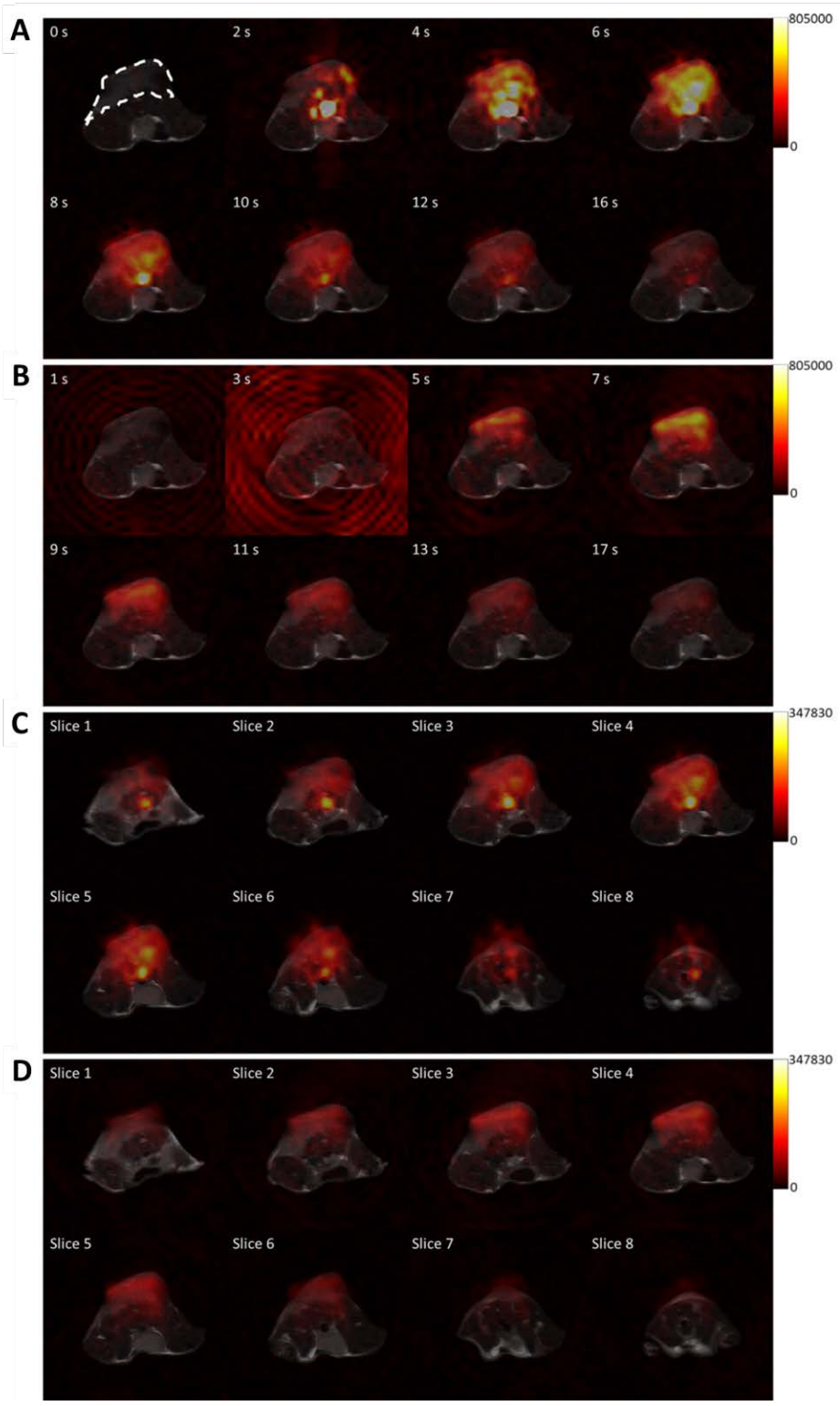

Figure 2.6: In vivo images with single-shot 3D sequence

Representative dynamic hyperpolarized [1-^{13}C]pyruvate (A) and [1-^{13}C]lactate images (B) acquired using the 32x32x8 design from a single slice (4th), overlaid on the corresponding T_2 weighted ^{1}H image. The ^{13}C images were interpolated to give a 256x256 in-plane matrix, which was then overlaid on the ^{1}H image, which had the same matrix size. The tumour

region is outlined in the pyruvate image acquired at the first time point (A). Images from all 8 slices at 6 s and 7 s are shown for pyruvate (C) and lactate (D), respectively. The images at 14 s (pyruvate) and 15 s (lactate) were acquired with the encoding gradients on the z axis turned off and were used as a reference and are not displayed. The signal intensity at each pixel is indicated with a separate colour scale for each panel, with the maxima indicated in arbitrary units.

The signal time courses for all three mice are shown in Figure 2.7. These were calculated by summing the signals from all the pixels in all the slices at each time point. The profile for the lactate signal was different from those widely reported in the literature because the 90º flip angle pulse on the [1-^{13}C]lactate resonance prevented accumulation of hyperpolarized ^{13}C signal. The first two time points were discarded from the lactate time course for the 3rd mouse because of contamination with signal from [1-^{13}C]pyruvate and [1-^{13}C]pyruvate-hydrate (see Figure 2.6b). The quality of the three dimensional ^{13}C images is dependent on B_0 homogeneity over the tumour region. B_0 maps, expressed as ^{13}C frequency variations (in Hz), are shown in Figures 2.8a and 2.8b. Frequency variations in the 3D FOV covering the whole animal are shown in Figure 2.8c. These frequency variations are relatively small and consistent with the quality of the images shown in Figure 2.6. The change in B_0 with z position, averaged over each slice, for all three mice, is shown in Figure 2.9.

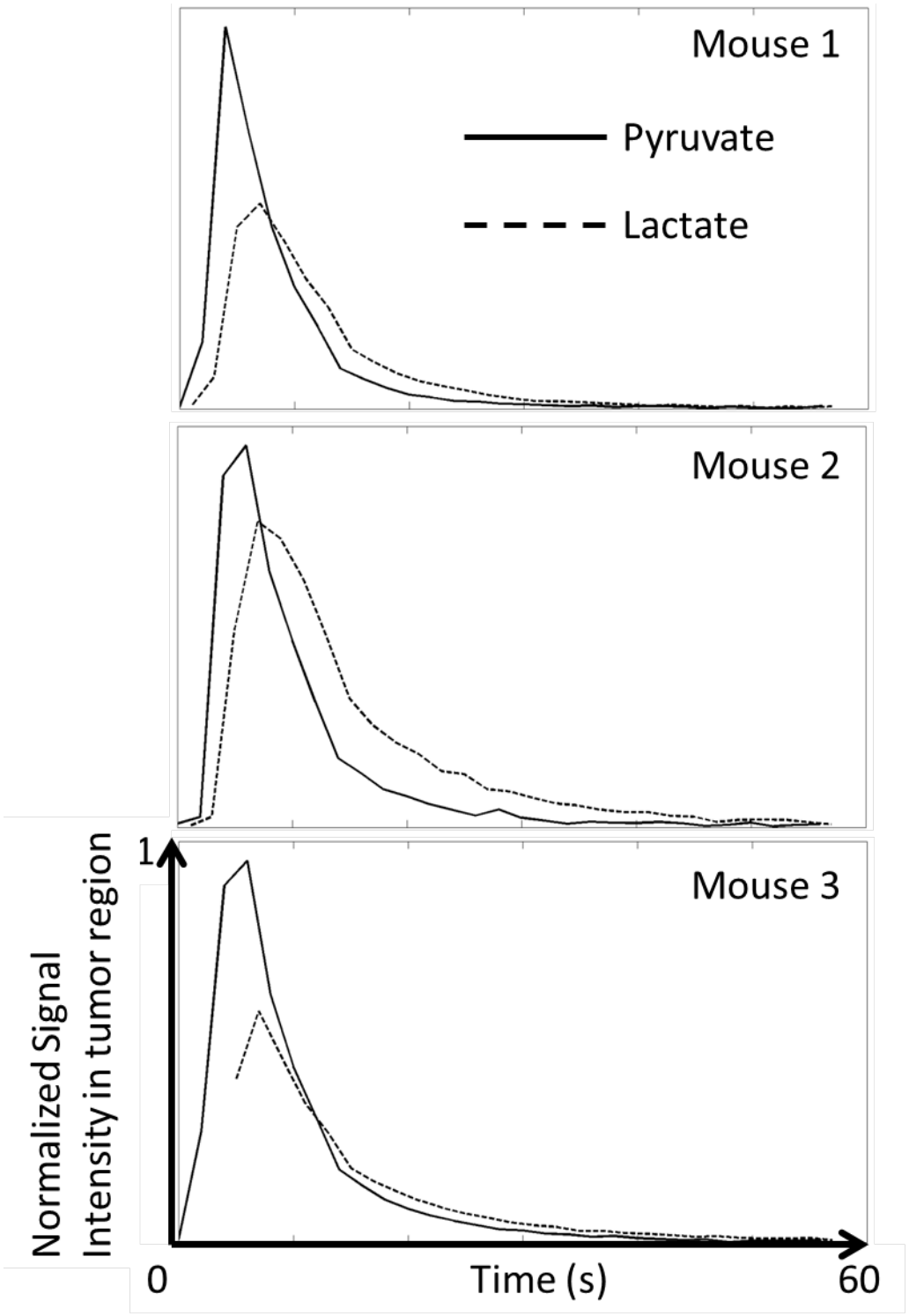

Figure 2.7: Time courses of the in vivo data

Time course of the hyperpolarized ^{13}C signals from pyruvate and lactate in the tumours of three EL4 tumour-bearing mice. The signals were summed across all the slices, for both pyruvate (solid line) and lactate (dashed line).

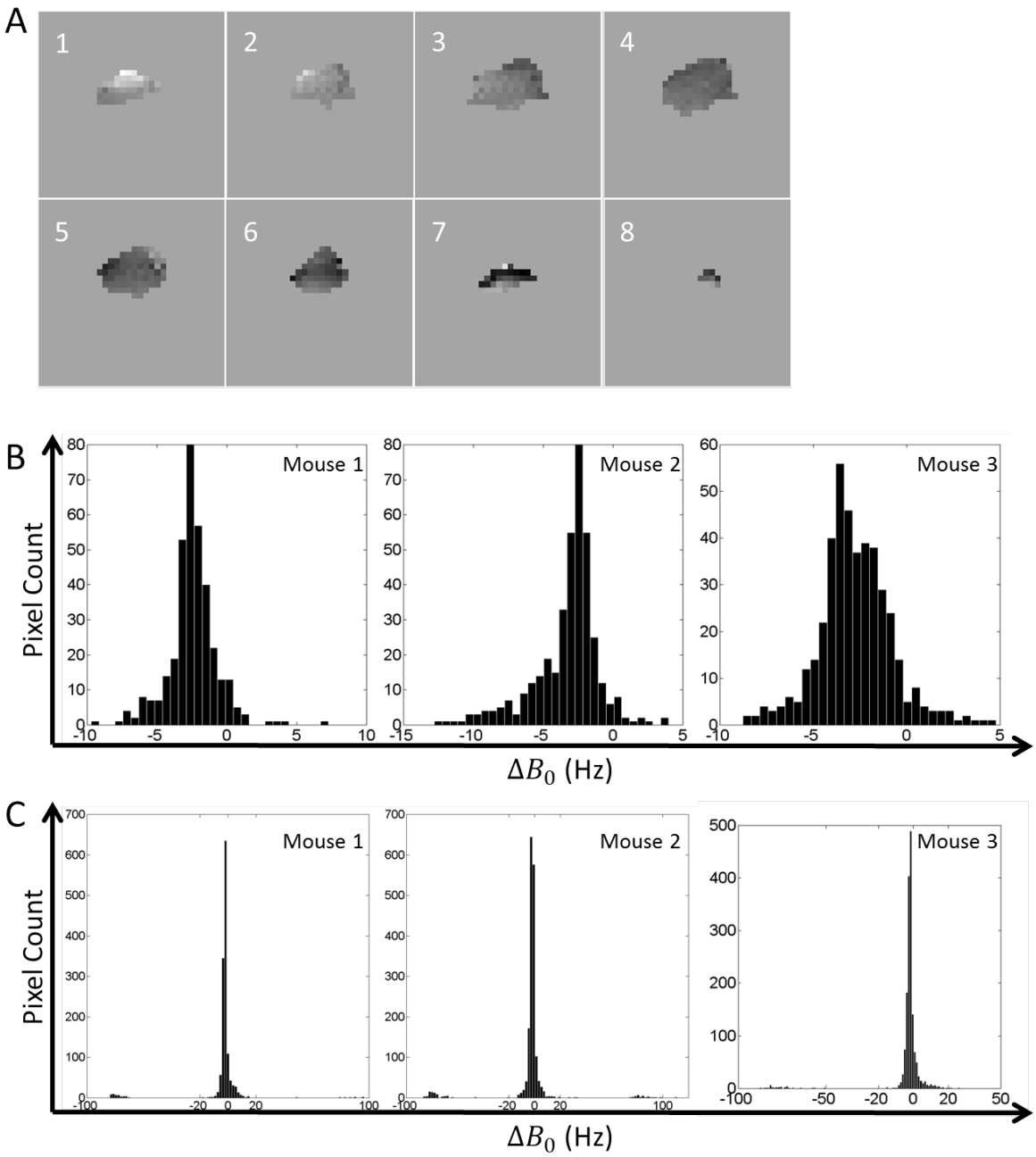

Figure 2.8: B_0 maps in in vivo experiments

Analysis of B_0 homogeneity. A) Representative B_0 maps, expressed as ^{13}C frequency variations, of the tumour region in a single mouse at all 8 slice positions. The frequencies varied from -10 Hz to +5 Hz, which is well below the limit of ±77.16Hz (see the Discussion section). B) Histogram analysis of the B_0 maps in the tumour regions from all three mice and for all 8 slice positions. C) Histogram analysis of the B_0 maps for regions of the whole animal covered by the 3D FOV. The B_0 maps were acquired using the water proton resonance and then converted to ^{13}C frequency variations based on the ^{1}H and ^{13}C gyromagnetic ratios.

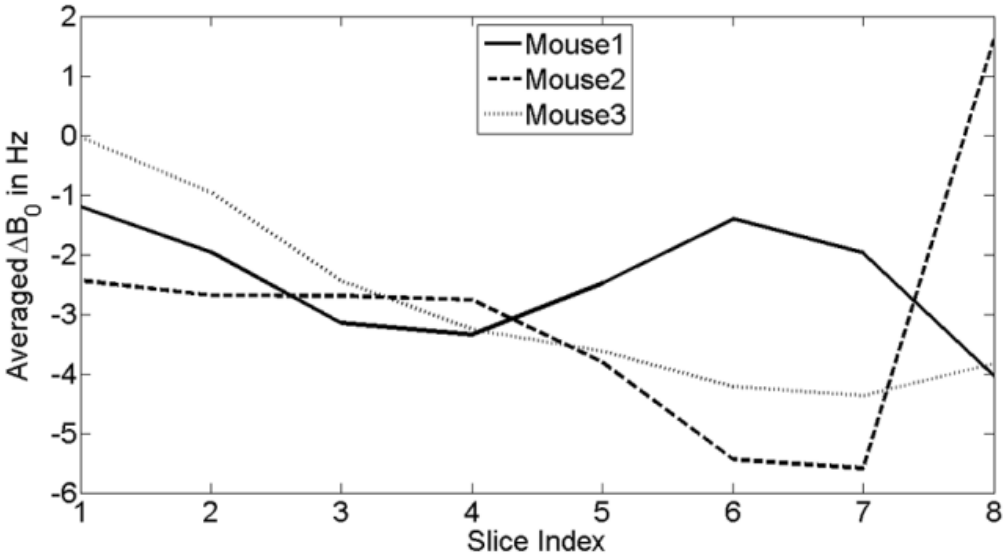

Figure 2.9: Cross-slice B_0 variations
Averaged ΔB_0 variation in the z-direction, for all three mice. The ΔB_0 values were averaged within the tumour region for each slice. These curves show a smooth transition of ΔB_0 between adjacent slices and thus minimal signal modulation in the z-direction.

2.4. Discussion

The pulse sequence is capable of capturing three-dimensional information in hyperpolarized MRI experiments, after a single excitation. Compared to multi-shot 3D imaging techniques for hyperpolarized MRI, it minimizes the number of excitation pulses, which helps preserve polarization, and gives a 3D image in less than 125 ms, which is faster than two previously published 3D sequences that used similarly high gradient strengths (780 ms/3D image in [97], 2.78 s/3D image in [142]). With the sequence described here the pyruvate and lactate polarizations can be sampled every second, which is beyond the capability of these other sequences. The sequence described here also provides comparable spatial resolution. While the nominal spatial resolutions in Ref [97] and Ref [142] were 2 x 2 x 3.8 mm^3 (matrix size 32 x 32 x 12) and 5 x 5 x 5 mm^3 (16 x16 x 12) respectively, the 32 x 32 x 8 design used here achieved a resolution of 1.25 x 1.25 x 2.5 mm^3, with the 16 x 16 x 12 design achieving 2.5 x 2.5 x 1.6 mm^3. When compared to multi-slice 2D imaging methods, this 3D sequence benefits from fewer excitation pulses. Although excitation pulses in 2D imaging sequences selectively excite specific slices, imperfect excitation profiles can lead to slice-cross-talk which further reduces the polarization in adjacent slices. Given the same flip

angles, this single shot 3D imaging sequence also provides an SNR benefit over multi-slice 2D methods by a factor of $\sqrt{N}$ (where N is the number of phase encode steps in the z-direction) [164], although signal decay due to T_2 /T_2* will compromise this benefit to some extent. This is unlike multi-shot 3D techniques [97], where the main SNR limitation comes from the flip angles used for each excitation. The SNR of this single shot 3D sequence could potentially be further enhanced when used with multiple averages, reduced flip angles and short TRs. The SNR enhancement in the latter case will be approximately $\sqrt{N} \times \sqrt{M} \times \frac{\sin \partial}{\sin \theta}$, where ∂ is the flip angle for each average in the 3D experiment, θ is the flip angle for the 2D experiment, and M is the number of averages. If $(\cos \partial)^M \approx \cos \theta$ then depletion of the polarization will be similar in the two experiments. A single-shot 3D technique has been proposed previously that exploits a hybrid acquisition scheme employing both fast spin echoes and an echo planar readout [165]. However, when compared with the technique described here, it can have a prolonged acquisition train, due to the less efficient echo-planar readout, and a hybrid phase error, where the stimulated echoes are mixed with the echo planar readout train.

B_0 inhomogeneity

Spiral readouts can suffer from off-resonance effects. Since different z-direction phase encoding information is involved in different spiral planes, there is no straightforward way to perform a self-navigated spiral phase correction. The reference scan data with z-direction phase encoding turned off was used here to correct for phase variations between spirals, and may also help to correct for off-resonance effects within each spiral. However, all the spirals used here were very short and therefore accumulate only a small phase error. These ultra-short spiral readouts make off-resonance effects less of a problem in the resulting images.

The second potential image quality problem resulting from B_0 inhomogeneity is unique to the sequence described here. Traverses between kz steps are separated by spirals, which gives a low sampling bandwidth in the kz-direction and can make the sequence prone to image distortions in the z-direction. Moreover, since the spirals are of different durations, the phase errors accumulated between kz steps are different, resulting in varying distortion

effects in the final image. The image distortion problem is relieved in two ways. The kz acquisition is split into two interleaved groups, which doubles the bandwidth in the kz-direction and thus halves potential image distortions. Secondly, the central two spiral planes are acquired at the spin echoes, which eliminates the phase error at the centre of k-space in the kz-direction. At the same time, the variable duration design for the spirals in the 32 x 32 x 8 sequence keeps approximately the same image distortion, while maximizing image resolution in the xy plane. Nevertheless, B_0 inhomogeneity is still a potential concern but can be analyzed quantitatively as follows.

Assume that the average phase error accumulated during a spiral due to B_0 inhomogeneity is $\theta(x, y, z)$, where x, y, and z specify spatial positions (in cm) with a certain B_0 shift. We need to ensure that image distortion lies within a single pixel such that image splitting is not observable. For this sequence, the presence of B_0 inhomogeneity ($\theta(x, y, z) \neq 0$) causes a division in the z-direction to give two images distorted by (see Section 2.6)

$$\pm \frac{FOVz}{2\pi} * \frac{\theta(x, y, z)}{2} \qquad 2.1$$

where FOVz is the field-of-view in the z direction. If this difference in position is less than a single pixel then splitting will not be observed. There is therefore a requirement that

$$\left| \frac{FOVz}{2\pi} * \frac{\theta}{2} \right| < \frac{FOVz}{L} \qquad 2.2$$

where the right hand side is the pixel size in the z-direction (L is the total number of encoding steps in the z-direction – here 8 or 12 spirals). This requirement translates to

$\left| \frac{L}{2\pi} * \frac{\theta}{2} \right| < 1$, or, $|\theta| < \frac{4\pi}{L}$; when $L = 8$, as was used in the mouse images, this becomes

$$|\theta| < \frac{\pi}{2} \qquad 2.3$$

As the largest spirals in the kz-direction, the 4th and 5th , are aquired close to the spin echoes, and because the spiral durations vary, then it is reasonable to assume that the phase errors accumulated during the 3rd or the 6th spiral, both of which are 3.24 ms in duration, will be the most likely source of this z-dimension artefact. This then puts a limit on the acceptable B_0 shift in each single voxel

$$|\Delta B_0(x,y,z)| < \frac{\frac{\pi}{2}}{3.24\ ms} = 77.16\ Hz \qquad 2.4$$

To check whether this condition was satisfied, spoiled gradient echo images were acquired with varying TEs and B_0 maps calculated. The B_0 maps of the tumour region of one mouse (Figure 2.8A) showed that the B_0 field was generally homogeneous and the variation was well under 77 Hz. This was the case for all three mice, as illustrated by histograms of the B_0 field distributions (Figure 2.8B). When moving to the clinic, with systems with more moderate gradient strengths, the sequence will need to be used with techniques such as a restricted excitation volumes to improve B_0 homogeneity.

While image distortion and ghosting are determined by the absolute value of B_0, the signal will also be modulated by the gradient of B_0 inhomogeneity in the z-direction. Figure 2.9 shows the through-slice changes of ΔB_0 in the tumour regions, where ΔB_0 was averaged within each slice. The overall through slice ΔB_0 was less than 5 Hz, which the equations given in Section 2.6 show would give a per pixel signal modulation of less than 5%.

Point spread function

For a single shot 3D sequence, the PSF in the z-direction determines the slice profile of the final image. A finite number of phase encoding steps in the z-direction leads to signal leakage across the slices, and this phenomenon is exaggerated when the number of phase encoding steps is small [163]. In the sequence described here the PSF is determined not only by the number of phase encoding steps but also by the spherical shape of 3D k-space. The gridding process used in image reconstruction can also alter the PSF. Overall, the 3D PSF resulting from the acquisition and reconstruction schemes used in the 32x32x8 implementation is shown in Figure 2.5A, for the sagittal, coronal, and axial views. The

FWHM of the PSF in the z-direction was approximately 7 mm, implying that for each slice there was significant signal contribution from other slices. In the xy plane, the PSF has a FWHM of about 1.8 mm, which is similar to other sequences in the literature [161]. Despite the compromised slice profile, the spherical-shaped 3D k-space has been widely used in the literature because of its high imaging efficiency [166-171], especially in cases where ultra-fast imaging is required.

The PSF in the z-direction could be improved by trading-off resolution in the xy plane. Figures 2.5B and 5c show the PSF of the cylindrical stack of spiral trajectory designs, with a matrix size of 16x16 in all kx-ky planes and 8 or 12 phase encoding steps in the kz-direction. The FWHMs of the PSFs are sharply truncated to about 3 mm and 2mm in the z-direction for the 16x16x8 and 16x16x12 designs respectively, while in the xy plane the FWHMs of the PSFs are more than 3 mm. The blurring of the signal in the z-direction for each acquisition scheme can be seen in the z-axis profiles shown in Figure 2.4. Each profile is principally the result of convolution of the experimental PSF, which depends on the ordering of the k-space acquisitions in the kz-direction, T_2 and T_2* decays and B_0 inhomogeneity, with the RF excitation profile. Ideally, an acquisition scheme will result in a z-axis profile that mimics the RF excitation profile. However, in practice all these factors will affect the experimental PSF along the z-axis leading to a stretched z-axis profile. In the sequence implemented here Figure 2.3 shows a comparable z-axis resolution for all three acquisition schemes, with minimal broadening resulting from their different theoretical PSFs. Therefore the acquisition scheme selected here for mouse imaging provides a practical compromise for acquiring dynamic 3D images from subcutaneous tumour models in mice.

Limitation of the excitation pulse

The water proton resonance frequency was used to set the central frequencies of the ^{13}C SpSp pulses. The wide spectral bandwidth (350 Hz) and the response profile of these excitation pulses enabled robust excitation of [1-^{13}C]lactate and [1-^{13}C]pyruvate. For example, a 50 Hz error in the central frequency of the [1-^{13}C]pyruvate excitation pulse will lead to only a 0.1% signal loss. However, if excitation pulses with smaller bandwidths were used, a real time frequency measurement may be needed to achieve the desired flip angle.

A problem of using SpSp pulses to image different metabolites alternately is cross contamination of signal between the metabolites. This phenomenon is more obvious when a spiral trajectory is used for signal acquisition, as can be seen from the lactate images acquired at 1 and 3 s (Figure 2.6B). The artefact in these two images, which has been observed previously [162], is the result of the SpSp pulse at the lactate resonance frequency also causing some excitation of the much more intense resonance from pyruvate (and probably from pyruvate-hydrate as well) in the aorta. This is despite the fact that excitation of the [1-^{13}C]pyruvate and [1-^{13}C]pyruvate-hydrate resonances is only 1% of that of the [1-^{13}C]lactate resonance. The [1-^{13}C]pyruvate signal in the aorta in this particular mouse was between 3 and 10 times more intense than the pyruvate signal in the other two mice, and hence this artefact was not observed in these other mice. The artefact was only observed in the early images, when the pyruvate signal in the aorta was much more intense than the lactate signal. However, it could be avoided altogether by using a coronal imaging slice or an excitation pulse with restricted FOV. The SpSp pulse could also be modified to further reduce cross-talk between the pyruvate and lactate resonances, however this could come at the expense of wider transition bands and the pulse would be less robust to the effects of B_0 offset.

Effects of relaxation

For the three sequence designs, the second echo is delayed by 46 - 59 ms compared to the first echo. In the [1-^{13}C]lactate phantom this resulted in an approximately 5% signal decrease in the second echo. In the images acquired in vivo the intensity of the second echo for pyruvate was 28.1±8.7% lower than that of the first echo; for lactate the decrease was 12.1±5.9%. These decreases in echo intensity are in agreement with the reported T_2 values for ^{13}C-labelled pyruvate (~170 ms) and lactate (~210 ms) in vivo [172]. If necessary, this signal loss in the second echo can be corrected for in the image reconstruction or signal analysis stages, since the echo intensities can be measured from the reference scan. As with other multi-echo sequences, T_2 and T_2*-dependent decay of the metabolite resonances broaden the PSF [104] by modulating the acquired signal in the kz direction, which is also determined by the ordering of the k-space acquisitions. This resulted in the signal leakage observed in Figures 2.6C and 2.6D, where signal from a central slice was observed in a

peripheral slice, which was evident from the presence of signal outside of the body of the animal in the peripheral slices. Although T_2* for each metabolite resonance could be estimated from the reference image this may be smaller than the true T_2* because of the effects of noise, eddy currents, and gradient/RF delays and therefore I did not include relaxation in calculation of the theoretical PSFs. The sequence will give higher slice resolution when used to image metabolites with longer T_2 and T_2*.

Translation to clinical imaging

The sequence was designed for pre-clinical imaging. However, it may also find clinical applications provided that the spirals can be kept short enough to avoid image distortion in the z-direction. With the much lower gradient strengths and slew rates used on clinical systems, this may require excitation pulses with a restricted FOV in the xy-plane so that the desired FOV can still be fully covered by short-duration spirals. This could be used, for example, to monitor tumour responses to treatment, where the location(s) of the tumours are already known and the excitation pulses could be focused at these sites. Spiral durations could also be kept short by extending the technique into a multi-shot sequence. This would still require far fewer excitations when compared to published multi-shot methods.

2.5. Conclusion

I have developed a single-shot 3-dimensional pulse sequence, based on spatial spectral pulse excitation and a stack-of-spirals acquisition in a multi spin echo train, for hyperpolarized ^{13}C MRI. The sequence was capable of imaging exchange of hyperpolarized ^{13}C label between injected hyperpolarized [1-^{13}C]pyruvate and endogenous lactate in a subcutaneous tumour model with a temporal resolution of up to 250 ms and a spatial resolution of up to 1.25 mm (32x32x8 design) in the xy plane and up to 1.7 mm (16x16x12 design) in the z-direction, given a 4 cm FOV in xy plane and 2 cm FOV in z direction. The sequence was robust to moderate B_0 field inhomogeneity. The use of a single excitation pulse allowed for a more efficient use of the hyperpolarized magnetization. Since the sequence length was much shorter than the TR there is a possibility for further optimization. Although the sequence was developed for pre-clinical imaging it nevertheless has the

potential to be used on clinical systems when the parameters are optimized for the lower gradient capabilities of these systems.

2.6. Appendix

In this section I give an analysis of the sequence's tolerance to B_0 inhomogeneity. Define:

$$\begin{cases} E_x \; the\; phase\; accumulated\; by\; encoding\; in\; x\; direction \\ E_y \; the\; phase\; accumulated\; by\; encoding\; in\; y\; direction \\ E_z \; the\; phase\; accumulated\; by\; encoding\; in\; z\; direction \end{cases}$$

where

$$E_z = e^{-i*2\pi*\frac{l}{FOVz}*z} \tag{2.5}$$

and FOVz is the FOV in the z-direction. l denotes the phase encoding index in this dimension.

$$l = -\frac{L-1}{2}, -\frac{L-3}{2}, \dots, \frac{L-1}{2} \tag{2.6}$$

The division by 2 in Equation 2.6 comes from the fact that the kx-ky plane at kz = 0 is not acquired. Instead, the kx-ky planes at kz = -0.5Δkz and 0.5Δkz are covered by the central two longest spirals.

For $\rho(x,y,z)$, which represents the ideal image, the acquired signal in this sequence (without phase error) can be written as

$$S(m,n,l) =$$

$$0.5 * \left[\iiint \{\rho(x,y,z) * E_x * E_y * E_z\} dxdydz\right] * \left[1 + e^{-i*\pi*(l-0.5)}\right] \tag{2.7}$$

$$+ 0.5 * \left[\iiint \{\rho(x,y,z) * E_x * E_y * E_z\} dxdydz\right] * \left[1 - e^{-i*\pi*(l-0.5)}\right]$$

where m and n denote the encoding index in the x and y directions, respectively. The two terms to sum in the equation above come from the two interleaved groups of spirals. In an acquisition with B_0 inhomogeneity, the acquired signal becomes

$$S'(m,n,l) =$$

$$0.5 * \left[\iiint \left\{\rho(x,y,z) * e^{-i*\frac{\theta}{2}*(-l+0.5)} * E_x * E_y * E_z\right\} dxdydz\right] * \left[1 + e^{-i*\pi*(l-0.5)}\right] \quad 2.8$$

$$+0.5 * \left[\iiint \left\{\rho(x,y,z) * e^{-i*\frac{\theta}{2}*(l+0.5)} * E_x * E_y * E_z\right\} dxdydz\right] * \left[1 - e^{-i*\pi*(l-0.5)}\right]$$

The average phase error $\theta(x,y,z)$ is divided by 2 because of the interleaved kz-dimension acquisition. In Equation 2.8, the phase error accumulation for the first group of spirals ($l = -3.5, -1.5, 0.5, 2.5$) is maximum for the 1st spiral, less for the 2nd spiral, fully refocused at the 3rd spiral (where the spin echo is formed), and greater again for the 4th spiral. The same trend is maintained for the second group of spirals ($l = 3.5, 1.5, -0.5, -2.5$). Equation 2.8 can be rewritten as the summation of 4 terms

$$S'(m,n,l) =$$

$$0.5 * \left[\iiint \left\{\rho(x,y,z) * E_x * E_y * e^{-i*2\pi*\frac{l}{FOVz}*\left(z-\frac{\theta/2}{2\pi}*FOVz\right)} * e^{-i*\frac{\theta}{4}}\right\} dxdydz\right]$$

$$+0.5 * \left[\iiint \left\{\rho(x,y,z) * E_x * E_y * e^{-i*2\pi*\frac{l}{FOVz}*\left(z-\frac{\theta/2}{2\pi}*FOVz+\frac{FOVz}{2}\right)} * e^{-i*\frac{\theta}{4}} * e^{i*\frac{\pi}{2}}\right\} dxdydz\right] \quad 2.9$$

$$+0.5 * \left[\iiint \left\{\rho(x,y,z) * E_x * E_y * e^{-i*2\pi*\frac{l}{FOVz}*\left(z+\frac{\theta/2}{2\pi}*FOVz\right)} * e^{-i*\frac{\theta}{4}}\right\} dxdydz\right]$$

$$-0.5 * \left[\iiint \left\{\rho(x,y,z) * E_x * E_y * e^{-i*2\pi*\frac{l}{FOVz}*\left(z+\frac{\theta/2}{2\pi}*FOVz+\frac{FOVz}{2}\right)} * e^{-i*\frac{\theta}{4}} * e^{i*\frac{\pi}{2}}\right\} dxdydz\right]$$

Each term in Equation 2.9 can be reconstructed into a separate image modulated from the ideal image, similar to the analysis in Xu et al [173]. For the first term of the four terms in Equation 2.9, let

$$z' = z - \frac{\theta/2}{2\pi} * FOVz = \beta(z) \tag{2.10}$$

we then have

$$z = \beta^{-1}(z') \tag{2.11}$$

Let $S'_1(m,n,l)$ represent the first term in Equation 2.9. We can now rewrite this first term as a function of z'

$$S'_1(m,n,l) = \iiint \left\{ \rho[x,y,\beta^{-1}(z')] * E_x * E_y * e^{-i*2\pi*\frac{l}{FOVz}*z'} * e^{-i*\frac{\theta}{4}} * \frac{\partial\beta^{-1}(z')}{\partial z'} \right\} dz'dydx \tag{2.12}$$

A 3D Fourier Transform of $S'_1(m,n,l)$ yields the first separate reconstructed image

$$\rho'_1(x,y,z') = \rho[x,y,\beta^{-1}(z')] * \frac{\partial\beta^{-1}(z')}{\partial z'} * e^{-i*\frac{\theta}{4}} \tag{2.13}$$

By substituting variable z (Equations 2.10 and 2.11) back into Equation 2.13 we get

$$\rho'_1\left(x,y,z - \frac{FOVz}{2\pi} * \frac{\theta}{2}\right) = \rho(x,y,z) \Big/ \left[1 - \frac{FOVz}{2\pi} * \frac{\partial\theta(x,y,z)/2}{\partial z}\right] * e^{-i*\frac{\theta}{4}} \tag{2.14}$$

Similar operations can be performed on the rest of the three terms in Equation 2.9, giving Equation 2.15.

$$\begin{cases} \rho'_1\left(x,y,z-\frac{FOVz}{2\pi}*\frac{\theta}{2}\right)=\rho(x,y,z)/\left[1-\frac{FOVz}{2\pi}*\frac{\partial\theta(x,y,z)/2}{\partial z}\right]*e^{-i*\frac{\theta}{4}} \\ \rho'_2\left(x,y,z-\frac{FOVz}{2\pi}*\frac{\theta}{2}+\frac{FOVz}{2}\right)=\rho(x,y,z)/\left[1-\frac{FOVz}{2\pi}*\frac{\partial\theta(x,y,z)/2}{\partial z}\right]*e^{-i*\frac{\theta}{4}}*e^{i*\frac{\pi}{2}} \\ \rho'_3\left(x,y,z+\frac{FOVz}{2\pi}*\frac{\theta}{2}\right)=\rho(x,y,z)/\left[1+\frac{FOVz}{2\pi}*\frac{\partial\theta(x,y,z)/2}{\partial z}\right]*e^{-i*\frac{\theta}{4}} \\ \rho'_4\left(x,y,z+\frac{FOVz}{2\pi}*\frac{\theta}{2}+\frac{FOVz}{2}\right)=-\rho(x,y,z)/\left[1+\frac{FOVz}{2\pi}*\frac{\partial\theta(x,y,z)/2}{\partial z}\right]*e^{-i*\frac{\theta}{4}}*e^{i*\frac{\pi}{2}} \end{cases} \quad 2.15$$

The overall reconstructed image (or, observed image) $\rho'(x,y,z)$ is the summation of the four separately reconstructed images

$$\rho'(x,y,z)=0.5*[\rho'_1(x,y,z)+\rho'_2(x,y,z)+\rho'_3(x,y,z)+\rho'_4(x,y,z)] \quad 2.16$$

In an ideal case, where the B_0 field is absolutely homogeneous ($\theta(x,y,z)=0$ for any x, y, and z), the observed image is identical to the ideal image (or, $\rho'(x,y,z)=\rho(x,y,z)$). This can be proved by substituting Equation 2.15 into Equation 2.16 with $\theta=0$. In the presence of B_0 inhomogeneity ($\theta(x,y,z)\neq 0$ and θ varies with x, y, and z), the observed image is split (in the z-direction) into two images, distorted by the term given in Equation 2.1 in the main text and each has a ghost at the $\frac{FOVz}{2}$ position in the z direction. Note that the ghostings from the split images have opposite signs. As long as the condition in Equation 2.4 is met, the image distortion is within a single pixel such that the image splitting is unobservable and the ghosts from the split images will cancel each other.

3. Single shot 3D sequence with doubled resolution

3.1. Introduction

In Chapter 2 I proposed a single-shot 3D sequence that makes efficient use of the transverse magnetization after each excitation. The sequence exploits the B_1-insensitivity of adiabatic pulses, following a dual-spin-echo (DSE) scheme that is widely used in other hyperpolarized MRI applications [101,106,108,112,115,174]. Although this sequence provided relatively high spatial resolution, further increases in resolution are desirable in view of the considerable metabolic heterogeneity displayed by tumours. Combined PET (positron emission tomography) and hyperpolarized ^{13}C MRI measurements can provide complementary information on tumour metabolism and could enrich significantly the information content of the imaging exam [175-177]. However, preclinical PET studies typically produce images with isotropic image resolutions of less than 2 mm, whereas the best resolution of the DSE scheme used previously was anisotropic (nominally 1.25x1.25x2.5 mm^3), and therefore requires image reformatting to co-register with a PET image. The DSE design could be modified to provide isotropic voxels [178], but at the cost of lower overall spatial resolution. Here I describe an enhanced single-shot 3D sequence that uses the hyperpolarization more efficiently, doubling resolution in the phase encode dimension and producing image voxels with nominally isotropic resolution. I also describe an alternative design that can significantly enhance the SNR, at the expense of a shorter imaging time window.

3.2. Methods

Tumour imaging

Tumours were obtained by subcutaneous implantation of EL4 murine lymphoma cells, as described in Section 2.2. Mice were fasted for 6-8 hours before imaging [157]. Images were acquired at 7T and the [1-^{13}C]pyruvate was hyperpolarized as described previously.

Pulse sequence

Target metabolite resonances were excited using the same 10.016 ms Spectral-Spatial (SpSp) pulse as in Chapter 2, with a bandwidth of 350 Hz and 1645 Hz (centre-to-centre) between replicate excitation bands. A 90° pulse required a B_1 field of 131.11 μT and used a fly-back trajectory to reduce vulnerability to eddy currents, with maximum gradient strengths of 0.19 and 0.2993 T/m at positive and negative polarities, giving a 1.2 cm minimum slab thickness. A fast spin echo train, with 4 refocusing pulses (Hyperbolic-Secant adiabatic pulse), followed the excitation pulse, with a stack of 4 spiral acquisitions during each spin echo (Figure 3.1A). Removal of slice selection gradients from the refocusing pulses used previously in Chapter 2 allowed signal acquisition from both even and odd echoes. Previously spirals were not acquired from odd echoes because a fully refocused spin echo, in the presence of slice selection gradients, requires a pair of HS adiabatic pulses [179], otherwise a quadratic phase is left across the swept frequency range, as illustrated in Figure 3.2C. This non-linear phase generated by an unpaired HS pulse results in signal loss as each k-space point is the summation of signals from a range of frequencies. When this range of frequencies is large, as is the case when a slice selection gradient is used, then signal loss is considerable. In the absence of a slice selection gradient the frequency range over which there is phase variation depends only on local B_0 field variation. In a reasonably well-shimmed B_0 field this frequency range is much smaller (of the order of ±50 Hz as compared to ±5 kHz when a slice selection gradient is present) and moreover shows a smooth variation leading to only mild signal loss (Figure 3.2D). Each spiral is encoded in the xy plane, and each stack of spirals is phase encoded in the z direction with blipped gradients such that a 3D k-space is acquired. The z dimension information is phase encoded in an interleaved manner and the kz index of each spiral (Figure 3.1C) in each stack is given in the following:

Stack 1: 15, 11, 7, 3

Stack 2: 16, 12, 8, 4

Stack 3: 2, 6, 10, 14

Stack 4: 1, 5, 9, 13

The phase encoding gradients on the z axis are self-refocusing in each acquisition interval in order to comply with the Carr-Purcell-Meiboom-Gill (CPMG) condition. In each acquisition interval the spiral dimensions in the kxy plane are 4x4, 16x16, 32x32, 8x8, in the order as displayed in Figure 3.1A, and the spiral dimensions for the 3D k-space are thus (Figure 3.1B, from kz1 to kz16): 4x4, 4x4, 8x8, 8x8, 16x16, 16x16, 32x32, 32x32, 32x32, 32x32, 16x16, 16x16, 8x8, 8x8, 4x4, 4x4. The durations for the 4x4, 8x8, 16x16, 32x32 spirals are 0.552, 1.216, 3.120, and 8.500 ms respectively. Each spiral encodes a FOV of 4x4 cm in the xy plane. This sequence is referred to as FSE-I hereafter. An alternative sequence (hereafter referred to as FSE-II) can be constructed such that the same z dimension phase encoding as in Figure 3.1A is repeated in additional stacks 5 to 8 and the sampled points are averaged with the datasets acquired through stacks 1 to 4 (see Figure 3.1B).

Imperfect refocusing pulses can dramatically deplete the polarization, especially within their transition bands. Therefore adiabatic inversion pulses with hyperbolic-secant modulation (HSn, n = 8) [180] were used for refocusing, where each had a duration of 10 ms (Figure 3.2A) and a bandwidth of 10000 Hz (Figure 3.2B shows the effect of the pulse on the longitudinal magnetization at a B_1 field strength of 100 μT). The pulses were designed to achieve perfect inversion (>99.9% of the longitudinal magnetization inverted) when the B_1 field was between 100 to 6400 μT. The large time-bandwidth product also ensured insensitivity to B_0 inhomogeneity and that there was only a small and smooth phase variation in the frequency response so that signal loss was minimized. The phase response of the pulse, when applied along the y axis, on the y magnetization is shown in Figure 3.2C. The central part of this phase response is expanded in Figure 3.2D.

To preserve the CPMG condition, the delay τ in Figure 3.1A was 15.284 ms, which was determined by the durations of the excitation and inversion pulses and the spirals. Since there are two spirals (8^{th} and 9^{th}) acquired at the centre of the kz direction, the resulting contrast is contributed by two different TEs (61.136 and 122.272 ms), which, in the FSE-II sequence, are averaged with another two echoes at 183.408 and 244.544 ms.

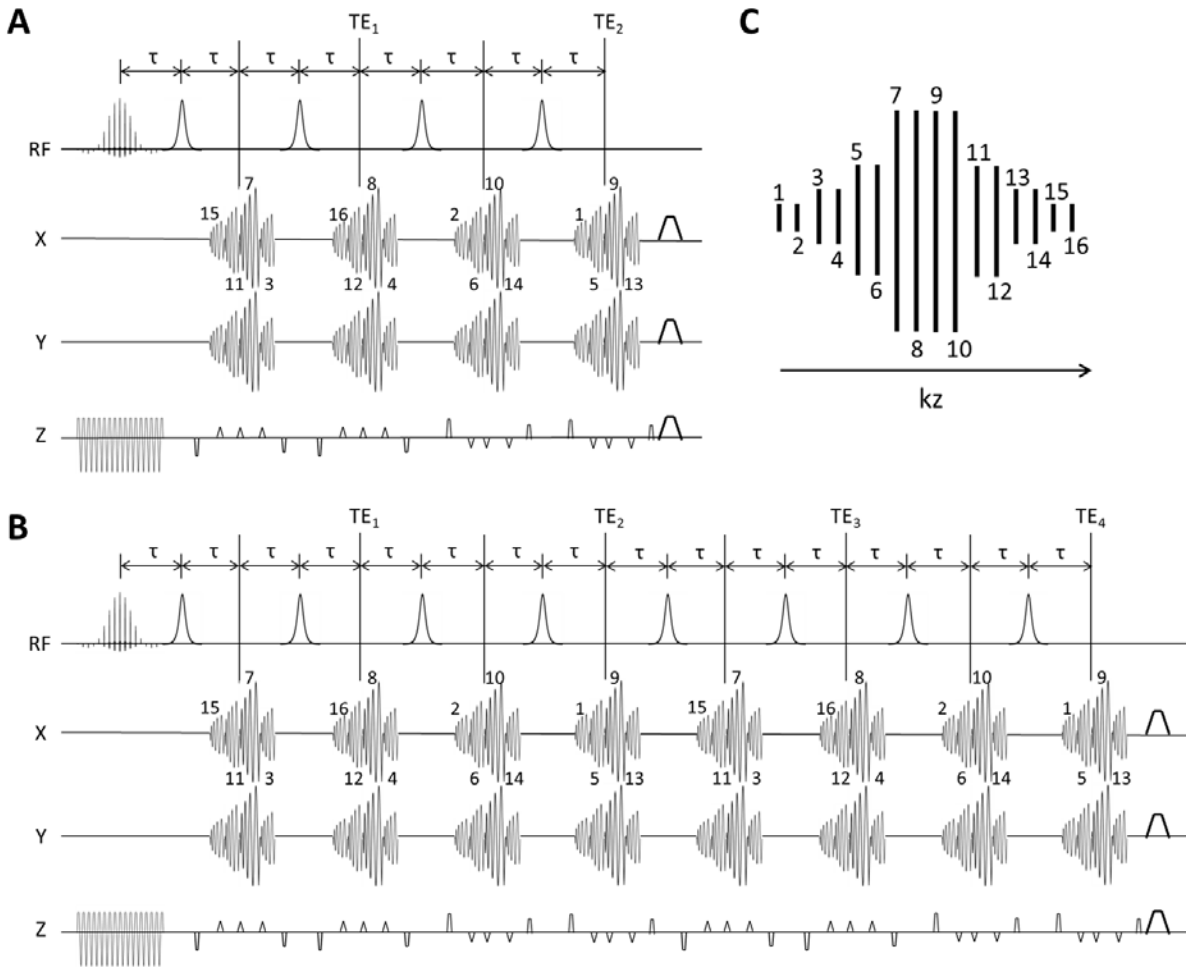

Figure 3.1: Single-shot 3D sequences with doubled resolution

The proposed pulse sequences and their k-space trajectories in the kz direction. (A) FSE-I pulse sequence, which starts with a spectral-spatial excitation pulse and a train of 4 adiabatic refocusing pulses. A stack of 4 spiral acquisitions is acquired after each refocusing pulse, and each spiral is phase encoded in the z direction by blipped gradients on the z axis. (B) FSE-II pulse sequence. Four extra stacks of spiral acquisitions are acquired following an extra 4 adiabatic refocusing pulses. These 4 extra stacks of spiral acquisitions have the same phase encodings in the z direction as in the first 4 stacks and the signals are then averaged in order to improve SNR. The FSE-II sequence hence shares the same k-space trajectories as the FSE-I pulse sequence. (C) k-space trajectory in the kz direction. Each spiral index in the sequences in (A) and (B) corresponds to a kz position in (C).

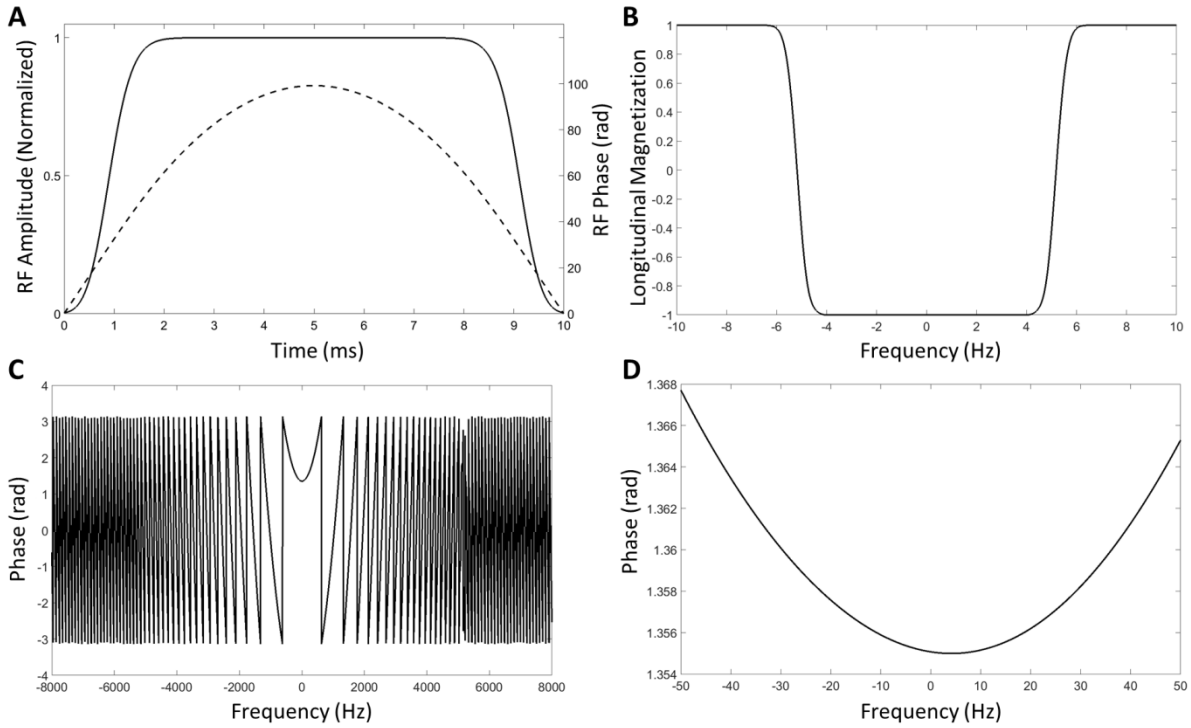

Figure 3.2: Adiabatic inversion pulse design
Adiabatic pulse design. (A) B_1 (solid line) and phase (dashed line) waveforms. (B) Simulation of the inversion profile. The pulse was designed to have a bandwidth of 10 kHz and to achieve >99.9% inversion over a frequency band of ±4 kHz at a B_1 field strength between 100 to 6400 µT. (C) The quadratic phase induced in transverse magnetization when the pulse is applied to magnetization lying on the y axis. The same quadratic phase could be observed across the whole slice when a slice selection gradient was applied. (D) The quadratic phase variation is small within a frequency band of ± 50 Hz of the frequency offset of the pulse.

Simulations

The PSF of the acquisition trajectory was simulated for the proposed sequences, where a constant k-space was sampled by the proposed k-space trajectory and 3D Fourier transformed into the image domain [161]. This was then compared with the PSF obtained using the forerunner of these sequences, the DSE sequence. When relaxation was taken into account, the k-space points of each spiral were weighted by the T_2 or T_2* decay at the centre of each kxy plane and then 3D Fourier transformed. Despite additional signal obtained from the later echoes, the FSE-II sequence has the same k-space trajectory and hence the same PSF as the FSE-I sequence when relaxation is ignored.

Pulse calibration

The adiabatic pulse was calibrated on a cylindrical phantom (7 mm inner-diameter) filled with 5 M [1-^{13}C]lactate at thermal equilibrium. A pulse-acquire sequence without any gradients was used, where 2048 data points were acquired at 4 μs intervals immediately after the pulse. The sequence swept a range of frequencies (from 0 Hz to 4500 Hz offset, with 300 Hz step size) and B_1 field strengths (from 40 to 470 μT). The inversion pulses were also tested on a cylindrical phantom of the same size injected with hyperpolarized [1-^{13}C]pyruvate and imaged using both the FSE-I and FSE-II sequences. All the gradients were turned off except for the slice selection gradient for the SpSp excitation pulse. To mimic the RF exposure in experiments in vivo, the SpSp pulse was targeted alternately to the [1-^{13}C]pyruvate and [1-^{13}C]lactate resonance frequencies, with flip angles of 7° and 45° respectively, a slice thickness of 20 mm, and a TR of 1 s (hence 2 s TR at each frequency). The whole acquisition lasted for 90 s.

Phantom imaging

The DSE sequence and the FSE-I sequence were tested on the cylindrical phantom containing thermally polarized [1-^{13}C]lactate. One end of the phantom was positioned at the iso-centre (also the centre of the FOV in the z direction) to examine the definition of the resulting images. The FOVs for both sequences were 4x4x2 cm^3 in x, y, and z dimensions, acquiring a 32x32x8 matrix with the original DSE sequence and a 32x32x16 matrix with the FSE-I sequence. Identical spiral designs were used for the DSE sequence, which were the same as those described in Chapter 2, except for the optimized refocusing lobe at the end of each spiral. The flip angle was 90° for both sequences, exciting a slab of 12 mm. The excited slab was thinner than the z direction FOV to avoid wrap-around artefacts from both the transition band of the excitation pulse and the side lobes of the PSF in the z direction. The phantom was then repositioned with the centre of the phantom at the iso-centre in order to compare the SNR between the three sequences. To investigate signal loss caused by the quadratic phase imparted by unpaired adiabatic pulses, signal was acquired using the DSE and FSE-I sequences with the encoding gradients turned off on all three axes. The PSFs of the FSE-I and FSE-II sequences were simulated again by adding a weighting factor for signal

decay to each kz plane using the measured signal loss due to unpaired adiabatic pulses, the [1-^{13}C]lactate T_2 value measured in the phantom (1 s), and a T_2 value (300 ms) estimated in vivo at 7 T [174]. The simulation was then repeated using a T_2* decay of 12 ms measured at 7T [153].

FSE proton images were acquired as 16 slices to cover the same volume as the ^{13}C images, with a 4x4 cm^2 FOV, 1.25 mm slice thickness, and 256x256 matrix size.

Imaging of hyperpolarized [1-^{13}C]pyruvate and [1-^{13}C]lactate in vivo

Acquisition of [1-^{13}C]pyruvate images (FSE-I was used with 2 mice and FSE-II with 3 mice) started 2 s after tail vein injection of hyperpolarized [1-^{13}C]pyruvate. Five [1-^{13}C]pyruvate images were acquired at a 2 s frame rate before the first [1-^{13}C]lactate image was acquired, 1 s after the 5th [1-^{13}C]pyruvate image. [1-^{13}C]pyruvate and [1-^{13}C]lactate images were acquired in alternate order thereafter, hence there was a temporal resolution of 2 s/frame for each metabolite. The flip angles on [1-^{13}C]pyruvate and [1-^{13}C]lactate were 7° and 45° respectively. For [1-^{13}C]pyruvate this helps to preserve the polarization and for [1-^{13}C]lactate enhances the image SNR. The 8th pair of acquisitions was used as a reference scan, where the z-axis gradients were turned off except for the slice selection gradient and the spoiler. The FOVs in all 3 dimensions were 4x4x2 cm^3 and the acquisition matrix was 32x32x16, giving a nominal resolution of 1.25x1.25x1.25 mm^3. The excitation bandwidth was 12 mm at half maximum to avoid wrap-around artefacts in the z direction. The total acquisition window was 90 s. The water proton frequency was used to estimate the ^{13}C [1-^{13}C]pyruvate and [1-^{13}C]lactate resonance frequencies. T_2 weighted proton images (FSE, 128x128 matrix, 16 slices, 1.25 mm slice thickness) were acquired for positional reference.

Image reconstruction

^{13}C MRI images were reconstructed in Matlab (The Math Works, Natick, MA), as described in Section 2.2.

3.3. Results

The adiabatic pulses achieved almost complete inversion at ±3500 Hz when the B_1 field was greater than 120 μT, matching their expected performance (Figure 3.3A). Signals acquired from a phantom injected with hyperpolarized [1-^{13}C]pyruvate, using both the FSE-I and FSE-II sequences, are shown in Figure 3.3B. Fitting the time course of signal decay gave a T_1 of 50 s for the FSE-I sequence and 48 s for the FSE-II sequence, indicating that additional polarization depletion, incurred by doubling the number of inversion pulses in the FSE-II sequence, was negligible.

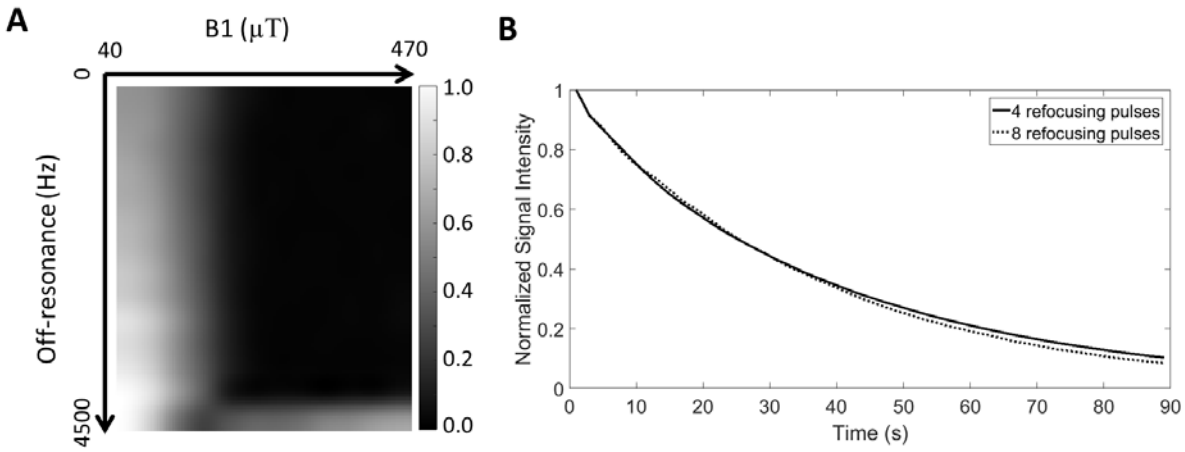

Figure 3.3: Calibration of adiabatic inversion pulse
Adiabatic pulse calibration. (A) A pulse-acquire sequence was used to calibrate the adiabatic pulse on a phantom filled with 5 M thermally polarized [1-^{13}C]lactate. The pulse was applied over a range of frequency offsets (0 to 4500 Hz) with varying B_1 field strengths (40 to 470 μT). Higher signal indicates worse inversion performance of the pulse. The signals were normalized to the maximum. (B) The FSE-I and II pulse sequences, which use 4 and 8 refocusing pulses respectively, were used to acquire signal from a phantom injected with hyperpolarized [1-^{13}C]pyruvate, where the pulses were set at the [1-^{13}C]pyruvate and [1-^{13}C]lactate resonance frequencies in alternate acquisitions, which were 1 s apart. The gradients were turned off except for the slice-selection gradient accompanying the excitation pulse.

The simulated PSFs in the xy plane (Figure 3.4A) for the DSE and FSE sequences were slightly different because of differences in the 3D k-space trajectories. However the FSE sequences halved the bandwidth in the z direction when compared to the DSE sequence (Figure 3.4B), which doubled the z direction resolution in the resulting image. This improved

resolution on the z axis was confirmed experimentally with images acquired from a phantom containing 5 M [1-^{13}C]lactate at thermal equilibrium (Figure 3.5). There was almost no signal outside the excited slab in the FSE-II image, whereas signal could be observed in the DSE image. Axial images acquired using the DSE and FSE-II sequences, when the centre of the phantom was at magnet centre (Figure 3.6A), showed that the SNRs of the two central z slices acquired using the FSE-I sequence were 0.86 and 0.83 times the SNRs acquired using the DSE sequence, reflecting the improved resolution, while the SNRs in slices acquired using the FSE-II sequence were 1.12 and 1.07 times the DSE SNRs (Figure 3.6B). Expressing the SNR per unit volume, the FSE-I SNRs were 1.72 and 1.66 times the DSE SNRs and the FSE-II SNRs were 2.25 and 2.13 times greater. The SNR curves in Figure 3.6B show the slab profile for each sequence, which was in agreement with convolution of the slice response of the excitation pulse (Figure 1.1C) with the PSFs in the z direction for each sequence.

Phantom data were also acquired with encoding gradients on all three axes turned off. The two acquired echoes in the DSE sequence and the four acquired echoes in the FSE-I sequence are shown in Figure 3.7A. The T_2 decay curve was obtained by fitting to the amplitude of the even echoes in the FSE-I sequence, as these were formed with paired adiabatic pulses and hence free of a quadratic phase twist and thus loss of signal. Signals from the odd echoes in the FSE sequence were approximately 10% lower than expected from signal decay due to T_2 relaxation, due to the nonlinear phase shift imparted by the adiabatic pulses (Figure 3.7A) as well as imperfections in local B_0 and B_1 fields. As shown in Figure 3.7B, signal loss due to unpaired adiabatic pulse increases slightly the width of the main lobe of the PSF by 2.3% while reducing the amplitude and bandwidth of the side lobes by 12.3% and 5.5% respectively. However, these effects disappear when T_2 decay is taken into account for both FSE-I (Figure 3.7B) and FSE-II sequences (Figure 3.7C). When T_2* decay was considered, the main lobe of the PSF was increased by 2.9% and the side lobe by 3.2%, compared to the T_2 decay only case, for both FSE-I and FSE-II sequences. The echoes from the central k-space in the FSE sequence were smaller in amplitude than their counterparts in the DSE sequence because the timing of the pulse train in the FSE sequence is different from that in the DSE sequence. In the DSE sequence, the minimum interval between the

excitation pulse and the first refocusing pulse is determined solely by the pulse durations, while in the FSE sequence this interval also depends on the durations of the 1st and 2nd spirals.

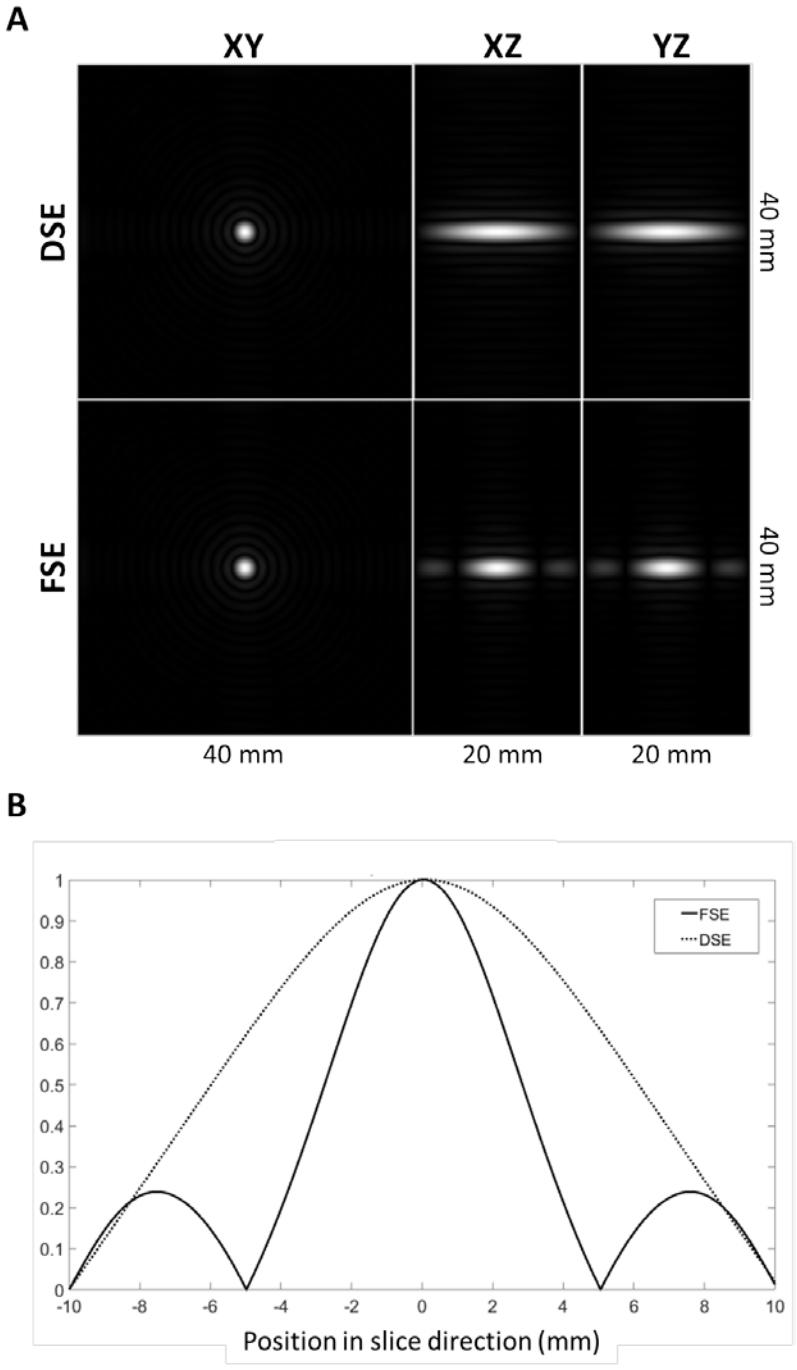

Figure 3.4: PSFs of the improved single-shot 3D sequence
Comparison of the PSFs of the proposed FSE sequences and a dual spin echo (DSE) sequence described previously. (A) PSFs in XY, XZ, and YZ planes. (B) PSF in the z direction.

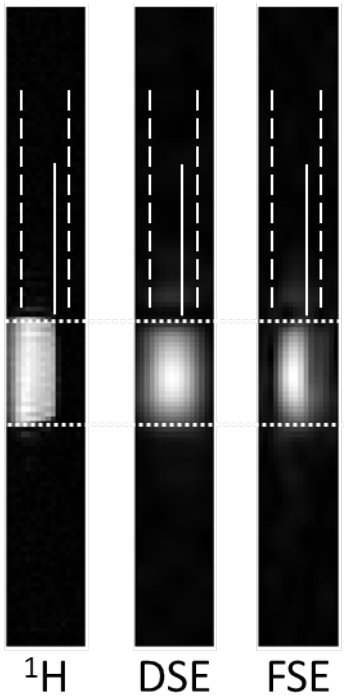

Figure 3.5: High definition in z-direction
The proposed FSE sequences enhance resolution in the z direction from a phantom (7 mm inner diameter) filled with thermally polarized [1-^{13}C]lactate. The dashed lines indicate the position of the excited slab and the solid lines indicate the edge of the phantom in the z direction. The phantom edges in the other dimension are marked by dotted lines. A high-resolution proton image is shown for positional reference.

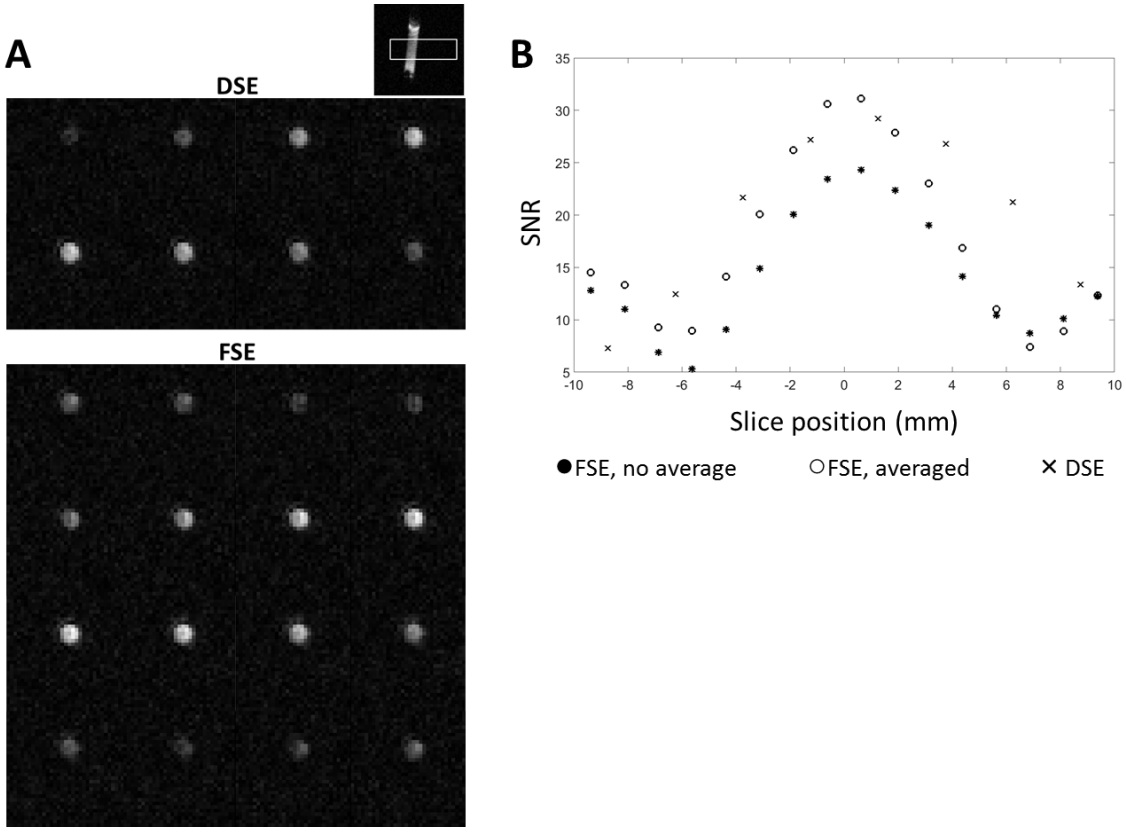

Figure 3.6: Measured slab profile
(A) Images acquired with the DSE and FSE-II pulse sequences from a cylindrical phantom containing 5 M [1-^{13}C]lactate at thermal equilibrium. (B) Signal from the first 4 echoes in the FSE-II pulse sequence (equivalent to the FSE-I pulse sequence) and signal obtained by averaging the signal from the first 4 echoes with the last 4 echoes in the FSE-II pulse sequence.

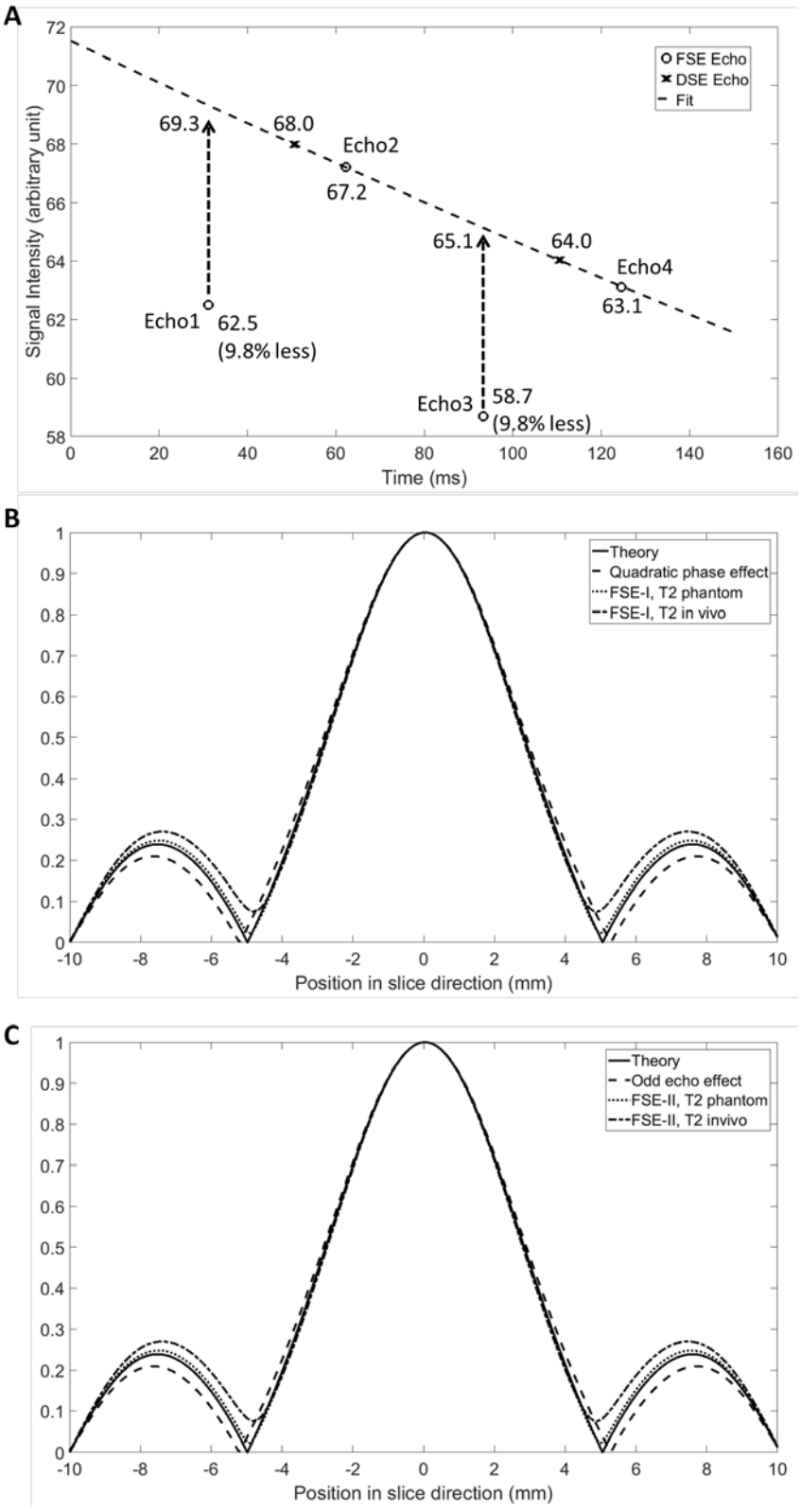

Figure 3.7: PSFs with relaxations and odd echo signal loss

(A) Signal loss in echoes formed with unpaired adiabatic refocusing pulses. DSE and FSE-I sequences were used to acquire signal from the lactate phantom shown in Figure 3.6, with

all encoding gradients turned off. The 2nd and 4th echoes acquired with FSE-I were fitted to give a curve that shows T_2 relaxation. The fitted curve matched well with the echoes acquired using the DSE pulse sequence. The 1st and 3rd echoes in the FSE-I sequence, which were formed by unpaired adiabatic pulses, were 9.8% smaller than the echoes that would have been formed had there been no adiabatic phase twist (as indicated by the curve showing signal loss due to T_2 relaxation). (B) Simulated PSFs for FSE-I sequence, showing the theoretical case (solid line), the effects of signal loss at odd echoes (dashed line) and the effects of T_2 relaxation, as measured in the phantom (dotted line), and in vivo (dash-dotted line). (C) Simulated PSFs for FSE-II sequence.

Representative [1-^{13}C]pyruvate and [1-^{13}C]lactate images acquired using the FSE-II sequence following i.v. injection of hyperpolarized [1-^{13}C]pyruvate in a tumour-bearing mouse are shown in Figure 3.8. [1-^{13}C]lactate images in all 3 planes (axial, sagittal, coronal) show considerable heterogeneity (Figure 3.9). Only the central 10 slices (in the z direction) are displayed in the sagittal and coronal images as the excitation slab was 12 mm. Representative time courses of signal intensities from the whole image and from the tumour region, acquired with the FSE-I and FSE-II sequences from the central 10 slices, are shown in Figure 3.10. The SNR enhancements for lactate in the FSE-II sequence, obtained by averaging signal from the earlier echoes with the later echoes, for the central 4 slices in frames 5 to 9, which were the frames with the highest SNR, were 32±8%, 19±2%, and 1.8±13.7% for the three animals imaged.

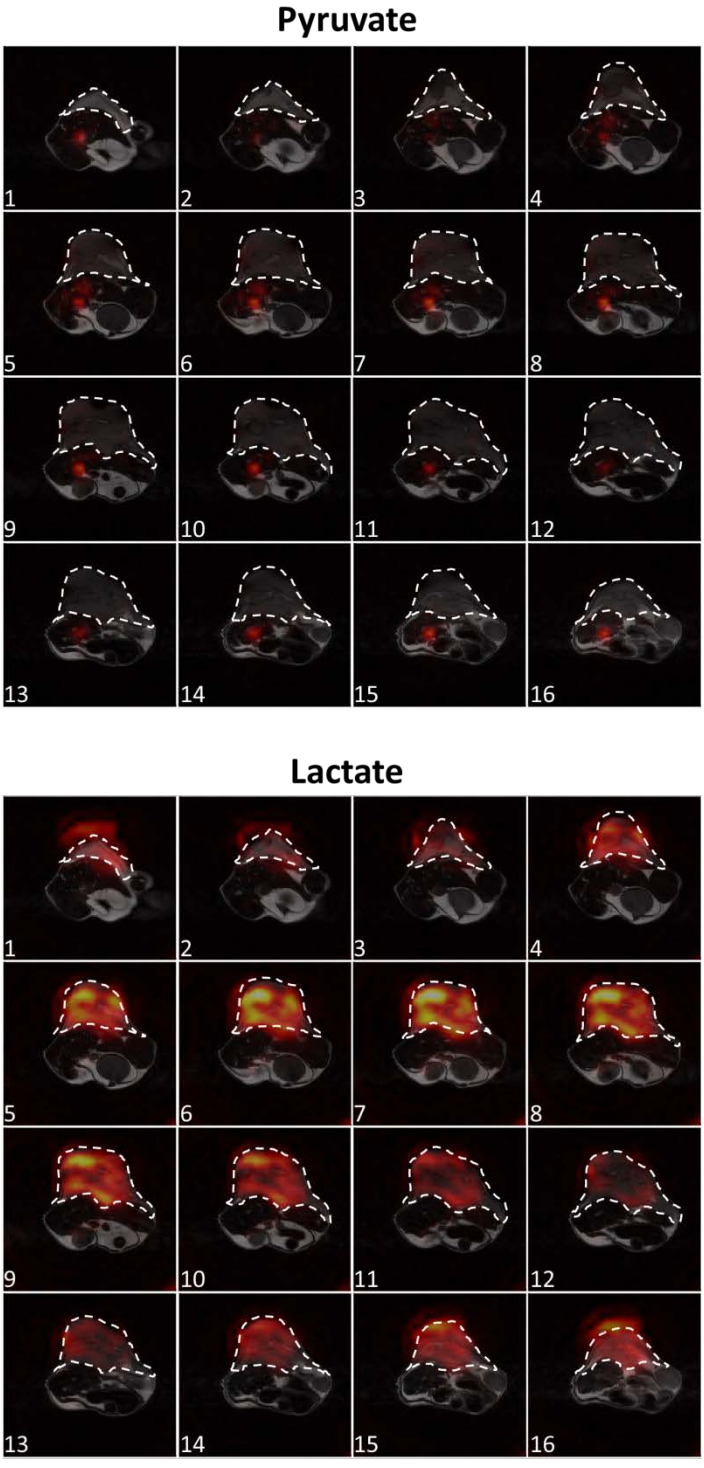

Figure 3.8: In vivo images with improved single-shot 3D sequence
Representative [1-^{13}C]pyruvate and [1-^{13}C]lactate images acquired in vivo using the FSE-II pulse sequence. All 16 z axis slices from a single frame (the 5th pair of lactate and pyruvate images) are shown. The slices are indexed in the tail to head direction. Unwanted signals were observed in slices at both ends in the z direction, due to ripples in the z direction PSF. The location of the tumour is indicated by a dashed white line.

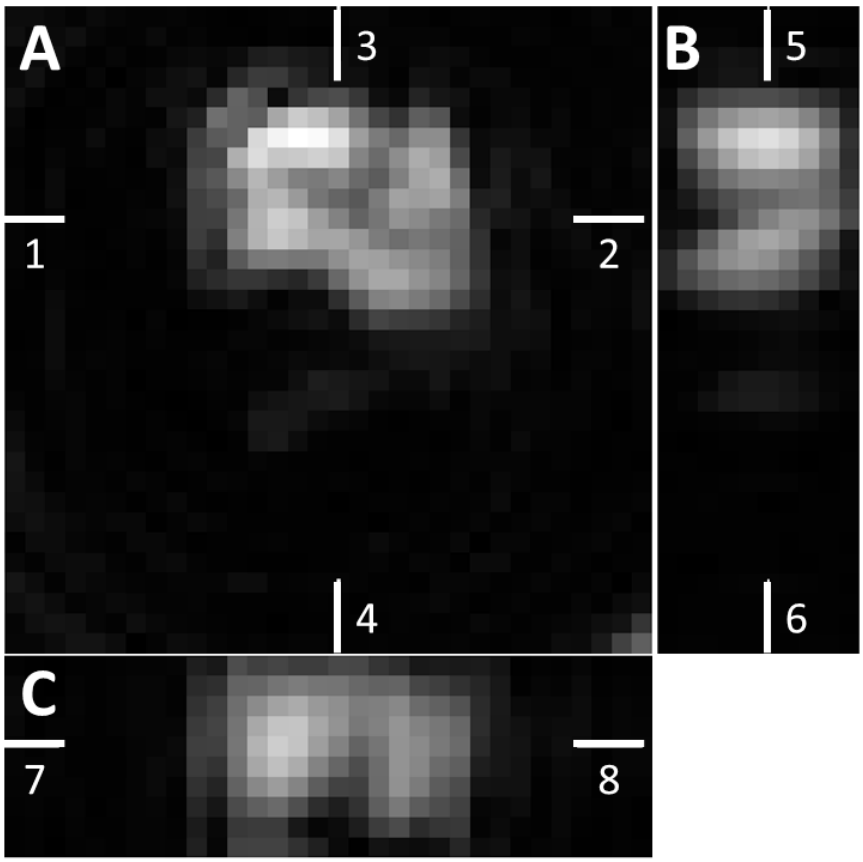

Figure 3.9: Heterogeneity observed in all three dimensions
Sagittal and coronal views reconstructed from the central 10 slices from the [1-^{13}C]lactate images shown in Figure 3.8. The 9th slice is shown as a representative axial plane image. The white bars indicate the positions of each displayed image in the 3D volume. (A) Axial plane, position indicated by bars 5 and 6 in (B) and 7 and 8 in (C). (B) Sagittal plane, position indicated by bars 3 and 4 in (A). (C) Coronal plane, position indicated by bars 1 and 2 in (A). Heterogeneity could be observed in both the xy plane and the z direction.

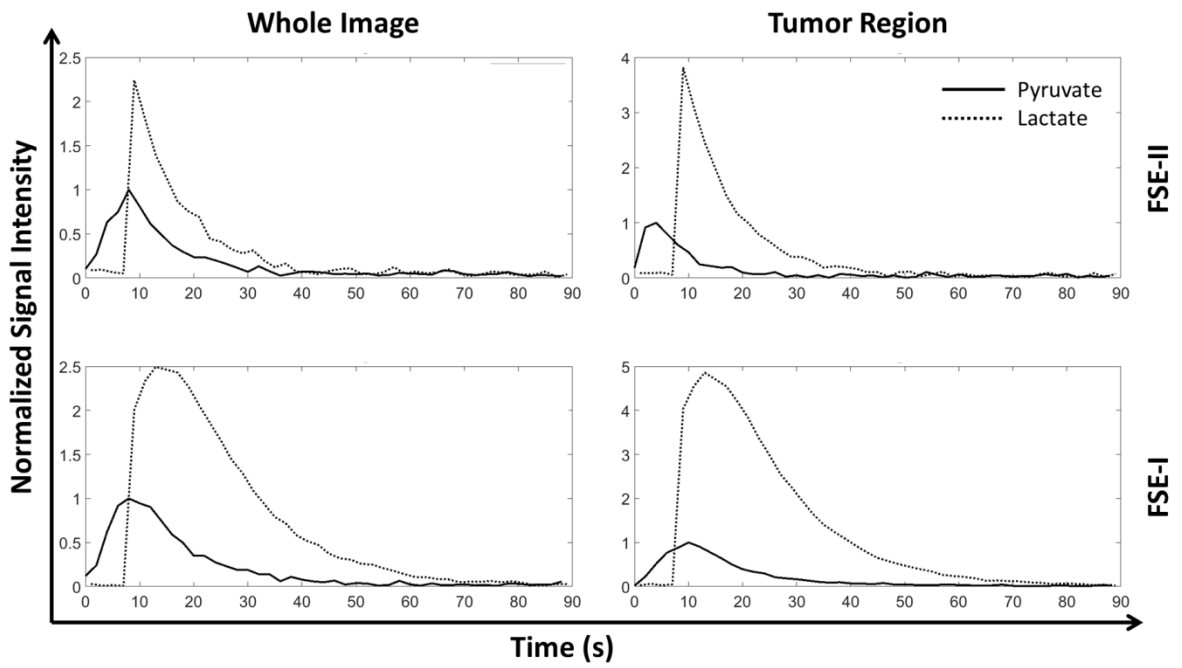

Figure 3.10: Time courses of the in vivo data
Representative pyruvate and lactate signal intensities in images acquired with the FSE-I and FSE-II pulse sequences from tumour-bearing mice injected with hyperpolarized [1-^{13}C]pyruvate. Signal intensities in the whole image and from the tumour region are plotted as a function of time after pyruvate injection. Each dataset was normalized to the peak value in the [1-^{13}C]pyruvate time course.

3.4. Discussion

While the previous DSE sequence provided high temporal and spatial resolution, the FSE sequences described here doubled the spatial resolution in the z direction at no sacrifice of temporal resolution. Although the FSE-II sequence doubled the sequence length from 125 ms to 247 ms, in practice the frame rate is rarely set to below 250 ms/frame as this would lead to fast depletion of the polarization. The doubled spatial resolution in the z direction, which gave nominally isotropic image voxels, could potentially enhance co-registration with PET images, which are naturally isotropic. ^{18}FDG-PET is well established in clinical practice for tumour detection and treatment response monitoring. However, ^{18}FDG shows enhanced uptake in any glucose avid tissue, such as the central nervous system and inflammatory lesions, as well as in tumours. The production of [1-^{13}C]lactate after injection of hyperpolarized [1-^{13}C]pyruvate may provide better specificity for tumour detection by exploiting a characteristic frequently displayed by tumours i.e. a propensity to reduce

pyruvate to lactate rather than oxidize it in the mitochondria, even in the presence of oxygen (known as the Warburg effect). Indeed, spatial discrepancies between the two techniques have already been observed [176]. The [1-^{13}C]lactate/^{18}FDG ratio may, therefore, enable improved detection of tumours in glucose avid tissues such as the brain and better discriminate between inflammation and disease.

Although PSF of the FSE sequences is much sharper in the z direction, it has a pair of side lobes toward the ends of the z direction FOV, which may result in image artefacts. Such artefacts can be observed in Figure 3.8. The slices at both ends of the z direction FOV (20 mm) should show no signal due to the limited thickness of the excitation slab (12 mm). These artefacts are less obvious in images acquired with the DSE sequence as they appear as image blur in the z direction. A window function could be applied to the k-space in the kz direction to reduce these artefacts, but this will render a PSF more similar to that of the DSE sequence and compromise the enhancement in image definition. Alternatively, the end slices could be discarded from the final set of images. Simulations of the PSF in the phantom experiments showed that modulation, caused by both T_2 decay and signal loss in odd echoes, was negligible (Figure 3.7B). Faster T_2 decay in vivo may result in greater modulation of the PSF, which is a common concern for FSE sequences, while the effects of signal acquisition from odd echoes should be relatively minor as the B_0 field is usually well shimmed on pre-clinical systems. In further simulations, the widths of the main lobes of the PSFs of the FSE sequences at a T_2 of 50 ms were half way between the widths in the FSE and DSE sequences when relaxation was ignored, demonstrating a resolution benefit for the FSE over the DSE sequence, even for metabolites with very short T_2s. T_2* decay during each acquisition interval can cause signal variations between the four spirals in each interval, which in general suppresses signals from the edge spirals in the 3D k-space and hence blurring in the z direction. However, the short durations of each spiral reduce this effect considerably. Moreover, simulations with T_2* = 12 ms, which was measured for [1-^{13}C]pyruvate at 7T [153], showed that the effect of a short T_2* on the PSF was negligible. The PSF of the proposed k-space design has a relatively broad FWHM, which is approximately 3 times the nominal resolution of the image. This could be improved, as discussed in Section 2.4, by adopting other 3D k-space shapes. For example, simply replacing all the spirals with the

16x16 spiral results in a 16x16x16 cylindrical k-space with 1.5 mm FWHM in the z direction PSF, which is very close to the nominal z-direction resolution of 1.25 mm, at the cost of a two-fold decrease in resolution in the xy-plane.

The key to implementation of these FSE sequences was the removal of the slice-selection gradients from the adiabatic refocusing pulses. The phantom experiments showed that signal loss caused by residual quadratic phase variation was <10% for both the 1st and 3rd echoes (Figure 3.7). However, this requires that the central frequencies of the adiabatic pulses closely match the resonance frequencies of the target metabolites in order to ensure that the majority of the resonance frequencies fall into the bottom of the phase variation well (Figure 3.2D). Dynamic measurements of the metabolite frequencies would be desirable and these could be embedded between the excitation pulse and the first refocusing pulse.

A concern for these FSE sequences is that off-resonance polarizations, for example, from untargeted metabolites or metabolites located in regions where their frequencies are off-resonance, may be depleted by the transition bands of the inversion pulses. This could be avoided by using adiabatic pulses with larger bandwidths. Initial experiments using adiabatic pulses with a 1.5 kHz bandwidth were much less successful than those using pulses with a 10 kHz bandwidth. The lifetime of the observable signal with a 1.5 kHz bandwidth pulse was only half of that with 10 kHz pulses. Another potential problem is the fringe-field effect [139,181], where the B_1 field drops rapidly at the ends of the transmit coil and results in imperfect adiabatic pulses that quickly deplete spin polarization in these areas. This phenomenon was observed in the experiments performed in vivo (Figure 3.10), where signals acquired using the FSE-I sequence persisted for much longer (60 s as compared to 30 s) than those acquired using the FSE-II sequence, which used double the number of inversion pulses. In contrast, in the phantom experiment, where the hyperpolarized [1-^{13}C]pyruvate remained at the iso-centre, both sequences resulted in signals that decayed at the same rate (Figure 3.3B). The fringe-field effect could again be relieved by using pulses with a wider bandwidth, which would result in greater tolerance to B_1 field inhomogeneity. A representative B_1 map acquired using a Bloch-Siegert sequence [182], with the same coil setup as used for the phantom and in vivo experiments, is shown in Figure 3.11. A larger

bandwidth requires increased RF power and while this was not a problem in our preclinical system, where the B_1 field can go beyond 500 μT, on a clinical system pulse bandwidth may be limited by the available B_1 field.

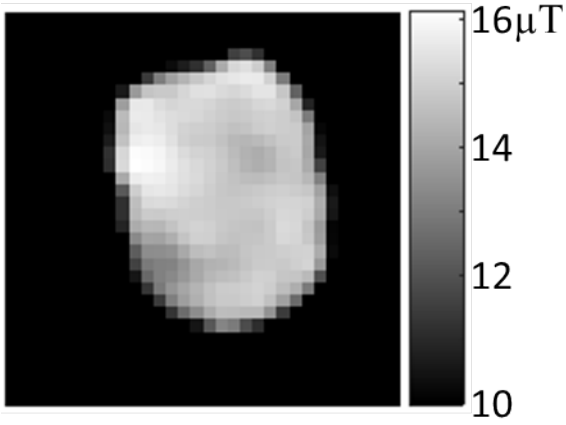

Figure 3.11: Measured excitation B_1 map
B_1 map acquired at the iso-centre in the z direction from a 20 mm slice. The same coil setup was used to acquire the B_1 map as used in the phantom and in vivo experiments. A sphere phantom (17.2 mm inner diameter) filled with thermally polarized 2 M [1-^{13}C]lactate was used. To cover a larger region in y direction, two B_1 maps were acquired when the phantom was positioned in two different locations along the y axis (-2.5 mm and 7.5 mm) and then combined into the displayed one. A RF power of 0.25 W was used for the Bloch-Siegert pulse.

Spiral-based trajectories are relatively insensitive to motion artefacts because of rapid traversal of k-space and dense sampling of the centre but are prone to off-resonance effects. These can arise from B_0 field inhomogeneity and eddy currents and usually lead to blurred and rotated images as a result of phase error accumulation during a single spiral [183]. Moreover, with blipped z gradients, phase error accumulations within each stack of spirals can lead to gross image shifts and distortions. Reference scans [163], where the z encoding gradients were turned off, were used to correct phase errors between spirals in the acquisition train, while the phase error accumulation within each spiral was ignored as all the spirals were very short in duration. Calculations, similar to those used in Chapter 2, showed that the sequences described here are immune to B_0 field inhomogeneity within $\pm\frac{\pi/2}{3.12\ ms} = \pm 80.12$ Hz (3.12 ms is the duration of spirals 5 and 12 in Figure 3.1A, which contribute most to the phase error accumulated at the centre of k-space). Usually a water

proton line width in vivo of 40-70 Hz could be achieved on our system when a spectrum is acquired from the imaging volume, therefore ^{13}C off-resonance frequencies should be much less than ±80 Hz. In addition, eddy current effects could be measured separately and removed retrospectively in the reconstruction process [129].

The lower SNR for the FSE-I pulse sequence, when compared to the DSE sequence, reflects its better resolution (Figure 3.6B). Theoretically the DSE sequence should give an SNR that is $\sqrt{2}$ times that of the FSE-I SNR, if signal loss due to T_2 and T_2*-dependent relaxation is neglected and rectangular slice profiles are assumed. However, the DSE SNR for the central slices was only ~1.2 times that of FSE-I sequence. This is because the signals are also weighted by the PSFs of the two sequences. The DSE/FSE-I signal ratio for the central slice, calculated from the areas under the simulated PSFs, was ~1.7, which is less than the value of 2 expected from the lower nominal spatial resolution. Since twice the number of echoes were acquired in the FSE-I sequence and $\sqrt{2}$ times the noise, the DSE/FSE-I SNR ratio should be $\frac{1.7}{2/\sqrt{2}} \approx 1.2$, in good agreement with what I observed experimentally. Other factors can also contribute to the SNR differences, including the non-linear phase in the FSE-I sequence and imperfect slice selection in the DSE sequence. The FSE-II sequence can be used to further improve the SNR of the FSE-I sequence, although there may be faster polarization decay if there is significant B_1 field inhomogeneity. This need not be a problem for a kinetic analysis if the extra polarization loss due to imperfect refocusing pulses is incorporated into a general RF depletion term in the modified Bloch-equations [184]. The FSE-II sequence improved the SNR substantially in phantom experiments and in two out of the three experiments performed in vivo with hyperpolarized [1-^{13}C]pyruvate. The reason that I failed to see an SNR improvement in the third mouse was not clear but implies that in this animal the T_2 of the [1-^{13}C]lactate resonance was shorter. Faster decaying signals during the echo train may eliminate the benefit of acquiring signal from later echoes in the FSE-II sequence, where the first echo in the repeated echo train appears at 152.84 ms after the excitation pulse. Assuming an echo train with perfectly refocused spin echoes, the T_2 will need to be at least 140 ms for there to be a gain in SNR by averaging signal from the later echoes. A T_2 for [1-^{13}C]lactate in this tumour model was measured to be 170 ms [172].

These pulse sequences have the potential for clinical translation, where they would benefit from the longer T_2s at lower fields. Specific absorption rate (SAR) is a potential problem, however the pulse bandwidth could be reduced and the adiabatic refocusing pulses could be replaced with non-selective composite pulses [185], although obtaining phase uniformity and refocusing performance in inhomogeneous B_0 fields would be challenging [186]. The number of pulses in these sequences is already much smaller when compared to clinical FSE sequences, such as single-shot FSE [187] and CUBE [188]. The repetition rate could also be reduced, for example in a clinical study, where 2D imaging was used, the TR was 5 s [27]. Clinical scanners are usually limited to much lower gradient strengths and slew rates than those used here, which may lead to long spiral durations and hence unacceptable image distortion in the z-direction. However, translation could be still possible if the FOV was kept small to cover a restricted region of interest so that short spirals could be used.

3.5. Conclusion

I have described a single-shot 3D fast spin echo pulse sequence that doubles the z direction resolution achieved by a similar sequence employing a dual spin echo design. An alternative sequence was described that regained the SNR lost due to the improved spatial resolution. Both sequences depend on the use of echoes formed by unpaired adiabatic refocusing pulses, where the quadratic phase twist was minimized by removing slice-selection gradients from the refocusing pulses. Although the primary applications of these sequences will be in pre-clinical studies, unpaired adiabatic pulses have the potential to be used for ^{13}C MRSI measurements in the clinic.

4. Referenceless workflow for Nyquist ghost removal in ^{13}C EPI

4.1. Introduction

As introduced in Section 1.5, echo planar imaging is widely used in hyperpolarized ^{13}C MRI since it is fast (sub-second), minimizes RF pulse exposure (only a single shot is required for a 2D image), produces artefacts that are easier to correct because of the Cartesian k-space, and there are well established methods for image reconstruction. However, a drawback of EPI is Nyquist ghosting in the phase encode direction, caused mainly by eddy currents [93], which result in accumulation of opposite phase errors in odd and even k-space lines [94]. Fly-back designs avoid bi-polar readout gradients and misalignment between alternate k-space lines [99], however they are more prone to geometric distortions and give a lower SNR [103].

EPI Nyquist ghosting can be removed by phase correction using a reference scan. In proton MRI this can be achieved by acquiring a reference data set with the phase encoding gradients turned off [94]. This method, however, is less desirable for hyperpolarized ^{13}C MRI because a time point is sacrificed in the acquisition of a full EPI reference scan. Alternatively a ^{1}H reference image can be acquired before the hyperpolarized ^{13}C image [103] or integrated ^{13}C reference echoes can be acquired by acquiring extra k space lines without phase encoding [97]. I describe here a workflow for Nyquist ghost correction that requires no additional reference acquisition and compare it with these other methods using both phantom and in vivo images.

4.2. Methods

Half-FOV ghosting in EPI images is mainly induced by: 1) group delays between readout gradients and signal acquisition; and 2) eddy currents in the readout direction [94]. These result in a 0th order phase error and a phase error that depends on position in the readout direction (X axis). The overall phase error is:

$$\theta(x) = \alpha + \beta x \qquad 4.1$$

where α is the phase error caused by a 0th order eddy current (e.g. a B_0 shift induced by a gradient pulse), and β is the linear phase error caused by the 1st order eddy current in the X direction. The phase error accumulated due to a group delay is equivalent to the effect of a 1st order short time constant eddy current in the readout gradient and is also included in Eq 4.1. The phase error θ has alternating polarities in even and odd k-space lines, resulting in Nyquist ghosting [94]:

$$\hat{\rho} = \rho(x,y)\cos[\theta(x)] + i\rho\left(x, y - \frac{N}{2}\right)\sin[\theta(x)] \qquad 4.2$$

where ρ is the ideal image, $\hat{\rho}$ is the reconstructed image, N is the number of phase encoding steps, and x / y are the coordinates in the ideal image in the frequency and phase encoding directions respectively. In short, the ideal image splits into a real one, at the original location, and an imaginary one, half a FOV away. This model typically holds for images acquired from non-oblique planes on modern MRI systems where cross-term and higher order term eddy currents are limited.

A reference scan can be used to estimate α and β. Alternatively an exhaustive search for the 0th and 1st order coefficients can be used, which renders a reference scan unnecessary. This concept was proposed initially for proton EPI [189], and then expanded [190] to include a search in the phase encoding direction. My search criterion was to minimize signal intensity in the ghost-containing background. This was identified based on prior knowledge of the location of the majority of the ^{13}C signal, which was obtainable from the proton image. The proposed workflow is illustrated in Figure 4.1A.

Pulse sequences

The proposed workflow was compared to 3 other phase correction methods: 1) direct ^{13}C reference scan [94], 2) integrated ^{13}C reference echoes [96], and 3) ^{1}H reference scan [103]. The pulse sequences used in these experiments are shown in Figures 4.1B and 4.1C. The ^{13}C imaging sequence acquired a 2D EPI k-space, starting with an excitation pulse and slice selection gradient, followed by a train of 20 bipolar readout gradients and, simultaneously, a train of 19 blipped phase encoding gradients. The acquisition matrix was

32 x 32, but only 4 k-space lines were acquired before the centre of k-space in order to minimize TE and enhance SNR, hence only 20 bipolar readout gradients were used (acquiring 62.5% of k-space). For the images acquired in vivo, a 15.936 ms spectral-spatial pulse (200 Hz excitation bandwidth, 1412 Hz between replicate bands) was used for excitation, while for imaging phantoms a 4 ms sinc excitation pulse with a 1600 Hz bandwidth was used. The sinc pulse was designed in Matlab (The Math Works, Natick, MA) using the SLR algorithm [159] with the rftools toolbox (available online at http://rsl.stanford.edu/research/software.html). The envelope-pulse and sub-pulses in the SpSp pulse were also generated using this toolbox and the envelope-pulse was then discretely sampled by the sub-pulse to achieve the desired stopbands between replicated excitation bands. The ^{13}C reference scan was acquired with the same imaging parameters but with the phase encoding gradients turned off. For ^{13}C imaging with integrated ^{13}C reference echoes, 3 extra readout lobes, with no phase encoding gradients, were inserted in front of the regular readout train. Each of the inserted lobes had the same shape as the regular readout lobe. For the ^{1}H reference scan, the same excitation pulse (same pulse width and flip angle) and the same readout gradient train (same amplitude and timing) were used as for ^{13}C imaging but with the phase encoding gradients turned off. The FOV in the readout direction of the ^{1}H reference scan was therefore approximately 1/4 (γ_{13C}/γ_{1H}) of that in the ^{13}C image. The slice selection gradient for the ^{1}H reference scan was reduced from that used for ^{13}C imaging to ensure selection of the same slice.

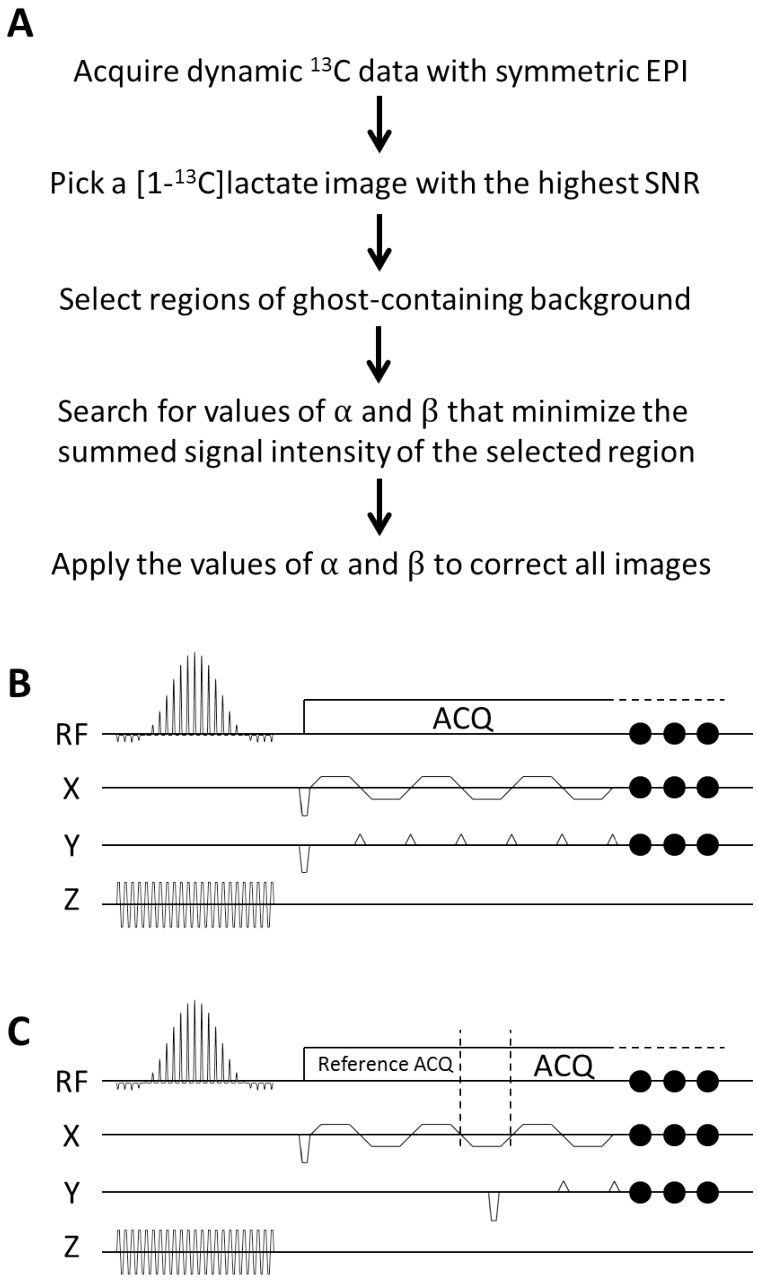

Figure 4.1: The referenceless workflow for Nyquist ghost correction
(A) Flow diagram outlining the proposed workflow for hyperpolarized ^{13}C dynamic MRI with a 2D echo-planar trajectory. The phase correction coefficients α and β can be searched for in individual images, for example the image with the highest SNR, or in summed images from the entire time series. The individual slice phase correction coefficients are then applied to the corresponding slices in the other images in the dynamic acquisition. (B) EPI sequence for ^{13}C imaging. The ^{13}C reference scan used the same sequence except that the phase encoding gradients were turned off. The same gradients for the ^{13}C reference scan were also used for the ^{1}H reference scan. (C) EPI sequence for ^{13}C imaging with integrated reference echoes. Three reference echoes, without phase encoding gradients, were acquired before the regular acquisition train, with a refocusing lobe in between.

Phantom experiments

Phantom experiments were performed on a 7T Agilent scanner (Palo Alto, CA, USA) with a $^{1}H/^{13}C$ transmit, ^{1}H receive volume coil and a 20 mm diameter ^{13}C surface receive coil (RAPID Biomedical, GMBH, Rimpar, Germany). The bore-size of the gradient coil was 120 mm. The maximum gradient strength was 0.4 T/m and the maximum slew rate was 3000 T/m/s.

A 90° flip angle ^{13}C sinc pulse was used in the ^{13}C imaging sequence to excite a 10 mm slice. Proton fast spin echo (FSE) images were acquired with a 256x256 matrix from the same slices and same FOVs as used for ^{13}C imaging, in order to provide a positional reference. The proposed workflow was compared with the other methods for phase correction under a variety of different acquisition conditions. The receiver bandwidth and echo spacing are given below. The former affects the phase error accumulation and the latter determines image distortion.

1. *Comparison with phase correction using a direct ^{13}C reference scan and using integrated ^{13}C reference echoes*

Images were acquired from a cylindrical glass phantom (inner diameter 7 mm) containing ~5 M [1-^{13}C]lactate with a 4 x 4 cm^2 FOV, 125 kHz receiver bandwidth (readout gradient 0.29 T/m), and 552 µs echo spacing. To investigate the effect of a restricted FOV, these experiments were repeated with a glass sphere phantom (inner diameter 17.2 mm) containing ~2 M [1-^{13}C]lactate and a 2.4 x 2.4 cm^2 FOV. The receiver bandwidth in this case was reduced to 100 kHz (readout gradient 0.39 T/m), and the echo spacing was therefore extended to 712 µs. To investigate the effect of multiple signal sources a dual phantom, containing the 7 mm and 17.2 mm diameter phantoms, was imaged using a 4 x 4 cm^2 FOV.

2. *Comparison with ^{1}H reference scan under de-shimmed condition*

The dual phantom described above was used. Images, with a 4 x 4 cm^2 FOV, were acquired in a relatively well shimmed magnetic field (^{13}C linewidth = 21 Hz) and following the imposition of a background XY gradient (approximately 0.006 T/m^2, where the ^{13}C linewidth increased to 25 Hz).

3. Performance of the proposed workflow with different FOVs

To further investigate the tolerance of the proposed workflow to restricted FOVs, images were acquired with different FOVs (20.5, 16.5, 12.5, and 11.5 mm) from a 10.5 mm diameter cylindrical glass phantom filled with 5 M ^{13}C-urea and the processed images were compared with those phase corrected using the direct ^{13}C reference scan method. The receiver bandwidth was 45 kHz, resulting in echo spacings of 931.2, 979.2, 1059.2, and 1091.2 µs respectively (readout gradient strengths 0.21, 0.25, 0.34, and 0.37 T/m). All images were acquired using 8 averages to ensure that there was a sufficient SNR, even for small FOVs.

In vivo imaging

Subcutaneous EL4 lymphomas in C57BL/6J mice [178] were imaged using the same hardware setup as for the phantoms. Female C57BL/6J mice bearing EL4 tumour were prepared by Ricard L. Hesketh and Deen Hu as described in Section 2.2. The tumours were then placed in the centre of the rigid 20 mm diameter surface coil for the imaging experiments. The mice were fasted for 6-8 hours before imaging as this has been shown to lead to more reproducible lactate labeling [157]. [1-^{13}C]pyruvate was hyperpolarized as described in [178] and the imaging pulse sequence started at the time of injection of 400 µL 82 mM [1-^{13}C]pyruvate.

The ^{13}C images covered a 4 x 4 cm^2 FOV, with a receiver bandwidth of 125 kHz, and were from a 6 mm thick slice. The resulting echo spacing was 552 µs. A constant 15° flip angle SpSp pulse was applied alternately to the [1-^{13}C]pyruvate and lactate resonances, with 1 second between, giving a TR of 2 seconds for each metabolite. The 11th pair of acquisitions was used as ^{13}C reference scans. T_2 weighted proton images were acquired using a FSE sequence (4 x 4 cm^2 FOV, 256 x 256 matrix) at the same slice position.

Image reconstruction

Images acquired from phantoms and in vivo were reconstructed in five different ways: using a ^{13}C reference scan [94]; using 3 integrated ^{13}C echoes [96]; using a ^{1}H reference scan [103]; using a 1D search for the optimal phase correction (0th order term and 1st order term

in X direction), which minimized signal in the ghost-containing background; and with a 2D search (including an additional 1st order term in the Y direction) [190]. Where reference data were acquired, a phase unwrap was first conducted in the x-ky hybrid space using Ahn's algorithm [191] and linear fitting was then performed to obtain the pair of phase correction coefficients pair. The missing k-space lines were zero-filled for each partial k-space acquisition prior to Fourier transformation.

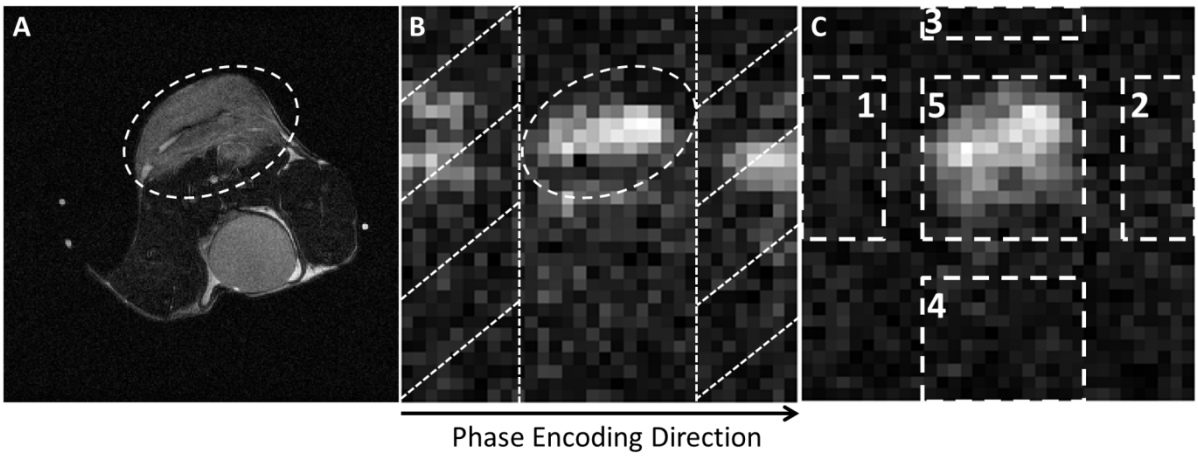

Figure 4.2: Selection of ghost-containing background
Selection of ghost-containing image areas, where the signal should be minimized using the proposed workflow. The tumour region is drawn from the proton image (A), and the resulting ROI was then applied to the [1-^{13}C]lactate image (B). Bands falling outside of the ROI in the phase encoding direction (bands with diagonal hatching in B) were considered as ghost-containing background areas. The image in (C) shows selection of object (5) and background areas (1 – 4) in one frame of the ^{13}C images, which were used for measurement of residual ghosting.

The proposed workflow is shown in Figure 4.1. Selection of ghost-containing regions is illustrated in Figure 4.2. The tumour region was identified from the proton image (Figure 4.2A) and used as the desired object in the [1-^{13}C]lactate image (Figure 4.2B). The selection of these regions for the 1D search method could be simplified as the operator need only specify regions beyond the two edges of the tumour in the phase encode direction, minimizing manual intervention. Nyquist ghost correction need only be calculated for one image in a series of dynamically acquired images (usually the [1-^{13}C]lactate image with the highest SNR) and the calculated coefficients, α and β, can then be applied to all the k-space lines in all the images in that series. For the phantom studies, α and β were calculated for

each individual image, where the proton image was used to identify regions that contain signal. Where there were multiple signal sources, a single region-of-interest (ROI) was drawn to include all sources of signal. Two bands, at both ends of the phase encoding direction (bands with diagonal hatching in Figure 4.2B), were assumed to be ghost-containing areas, and the algorithm minimized signal intensity in these areas. An exhaustive search of every combination of α and β was made between values of $-\pi/2$ and $\pi/2$ (phase error is periodic in π [192]), with 100 increments of each parameter (i.e. 100x100 permutations). This had a typical computation time of 15 s on a laptop PC running Matlab 2016a (The Math Works, Natick, MA, USA) for images with a matrix size of 32x32. For the 2D method the search was also performed between $-\pi/2$ and $\pi/2$, again with 100 increments of each of the three parameters and again in the image with the highest signal intensity. The search was conducted for each line in the frequency encode direction such that signal in the ghost-containing areas of each line was minimized. With both the ^{13}C and ^{1}H reference scans, the 1^{st} and 0^{th} order correction coefficients were calculated for each line in the phase encode direction. For the ^{1}H reference the coefficients were first corrected for the difference in gyromagnetic ratios before being applied to the ^{13}C images. With the integrated ^{13}C echoes, a pair of averaged 1^{st} and 0^{th} order coefficients was calculated and applied to all the phase encode lines. Phase correction was performed in Matlab using custom-written scripts.

Calculation of SNR

For SNR calculations in the phantom images, object and noise regions were identified in images phase corrected using a ^{13}C reference scan and then these regions were used for images corrected using the other methods. For images acquired in vivo, the object region was obtained in a similar way, from the [1-^{13}C]lactate image with the highest signal, and then applied to all images in the series. The noise standard deviation was calculated from the last [1-^{13}C]pyruvate image.

Calculation of ghosting level

$$ghosting\ level = \left|\frac{mean(region\ 1) + mean(region\ 2) - mean(region\ 3) - mean(region\ 4)}{2 \times mean(region\ 5)}\right| \times 100 \quad 4.3$$

Mean values were taken from the magnitude signal. Areas 1/2/3/4/5 are indicated in Figure 4.2C [193]. Area 5 was drawn on an image corrected using ^{13}C reference scan data, to include the whole signal containing area (this region could be different for [1-^{13}C]pyruvate and [1-^{13}C]lactate images in vivo if, for example, there was significant pyruvate signal from the aorta). This area was then moved by half a FOV in the phase encoding direction to define areas 1 and 2, and by half a FOV in the frequency encoding direction to define areas 3 and 4. For phantom images with a restricted FOV and multiple signal sources, all 5 areas were drawn manually.

4.3. Results

Images of the ^{13}C phantoms are shown in Figures 4.3 – 4.5 and a series of [1-^{13}C]pyruvate and [1-^{13}C]lactate images acquired after injection of hyperpolarized [1-^{13}C]pyruvate into a tumour-bearing mouse are shown in Figure 4.6.

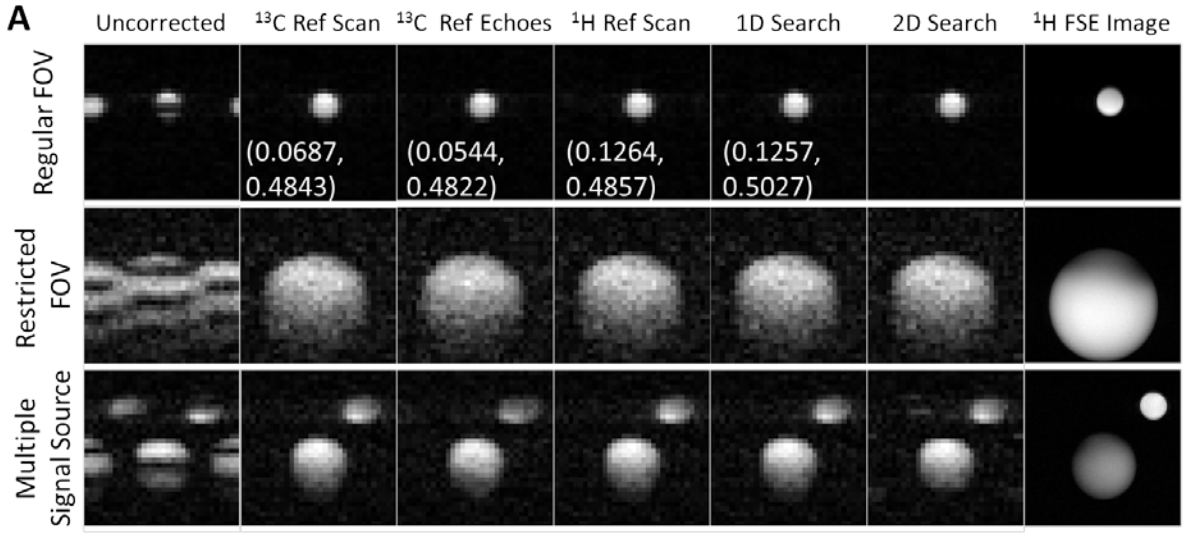
A
Uncorrected
^{13}C Ref Scan
^{13}C Ref Echoes
^{1}H Ref Scan
1D Search
2D Search
^{1}H FSE Image
Regular FOV
Restricted FOV
Multiple Signal Source
(0.0687, 0.4843)
(0.0544, 0.4822)
(0.1264, 0.4857)
(0.1257, 0.5027)

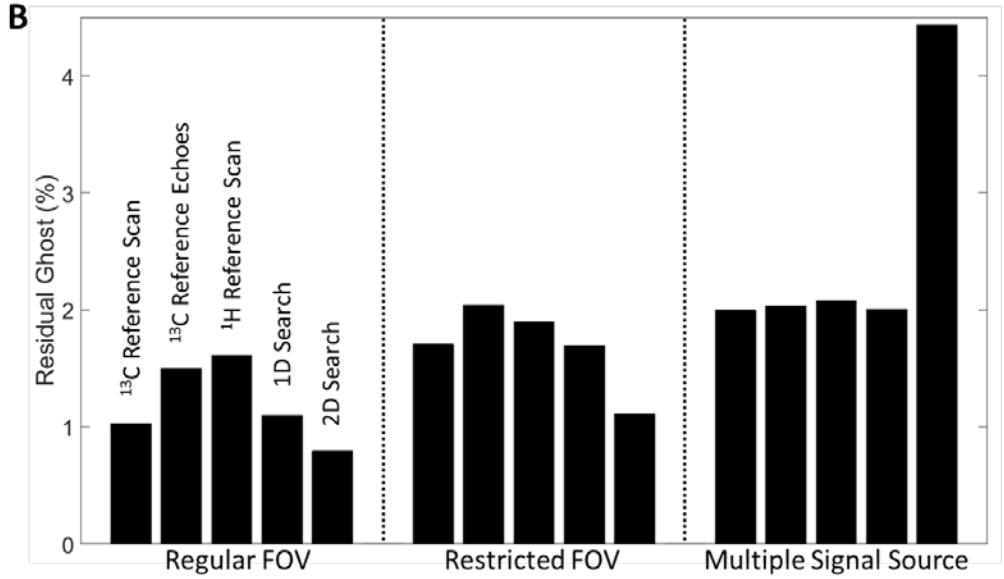
B
Residual Ghost (%)
0
1
2
3
4
^{13}C Reference Scan
^{13}C Reference Echoes
^{1}H Reference Scan
1D Search
2D Search
Regular FOV
Restricted FOV
Multiple Signal Source

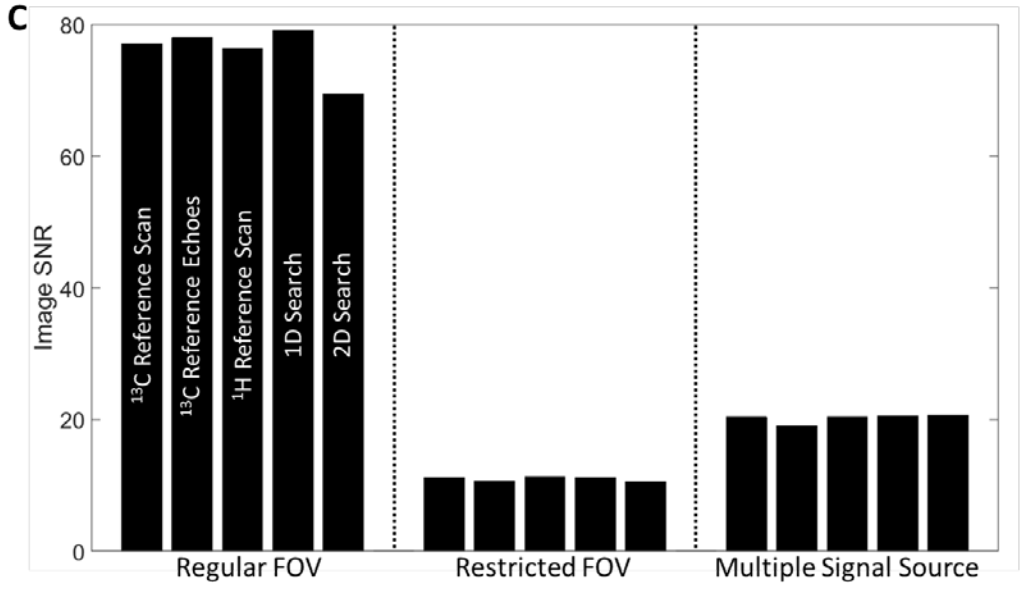
C
Image SNR
0
20
40
60
80
^{13}C Reference Scan
^{13}C Reference Echoes
^{1}H Reference Scan
1D Search
2D Search
Regular FOV
Restricted FOV
Multiple Signal Source

Figure 4.3: Comparison of phase correction methods on phantoms

^{13}C images of [1-^{13}C]lactate-containing phantoms at thermal equilibrium, phase corrected using the proposed work flow (1D and 2D searches) and the indicated methods (^{13}C reference scan, ^{13}C reference echoes, ^{1}H reference scan). (A) Images acquired using a regular FOV, a restricted FOV, and from two separate phantoms, and phase corrected using the indicated methods. The measured values for α, β are shown on the images acquired with a regular FOV, except for that corrected using a 2D search, where a different phase error model was used. The difference in the β values between the 1D search and the other methods resulted from the different step size in the search. B) Residual ghosting and C) SNR were measured for each of the phase correction methods under three different image acquisition conditions. The ghosting levels before correction were 63.2%, 30.8%, and 36.6% for the regular FOV, the restricted FOV, and multiple signal source cases respectively.

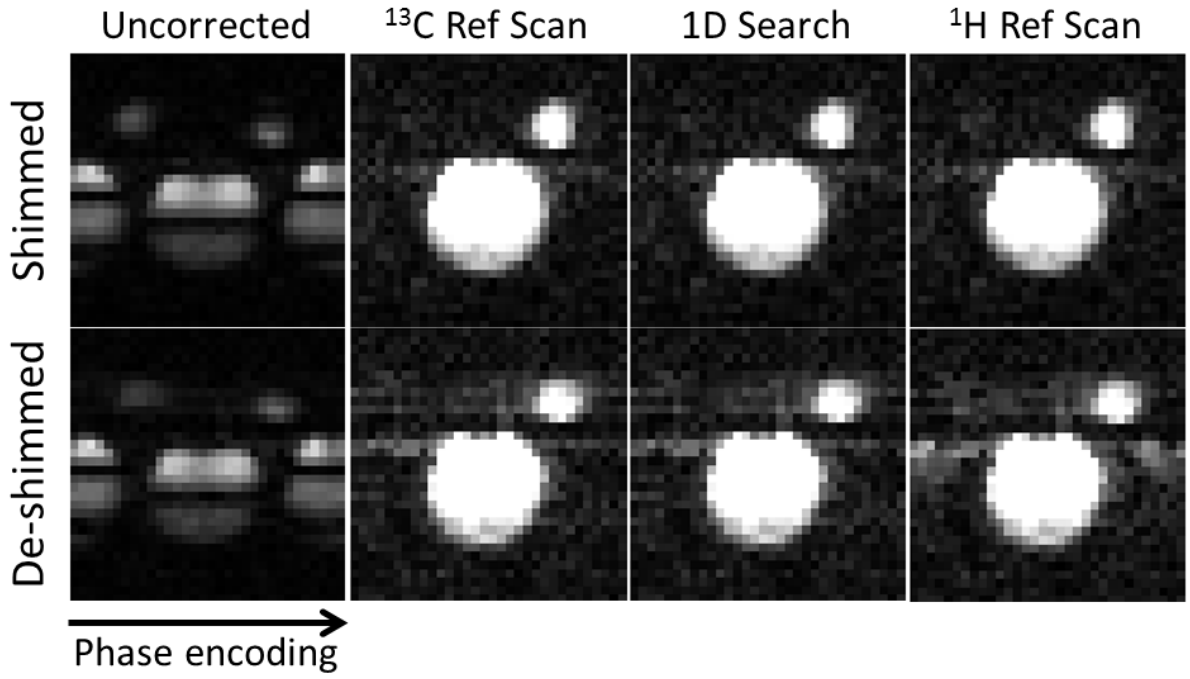

Figure 4.4: Phase correction methods in de-shimmed condition

Comparison between the proposed workflow, the ^{13}C reference scan method, and the ^{1}H reference scan method. Images were acquired from a dual-phantom with a well shimmed magnetic field and in the presence of magnetic field inhomogeneity, where a 6 mT/m^2 XY gradient was applied using the XY shim, and the images were phase corrected using the indicated methods.

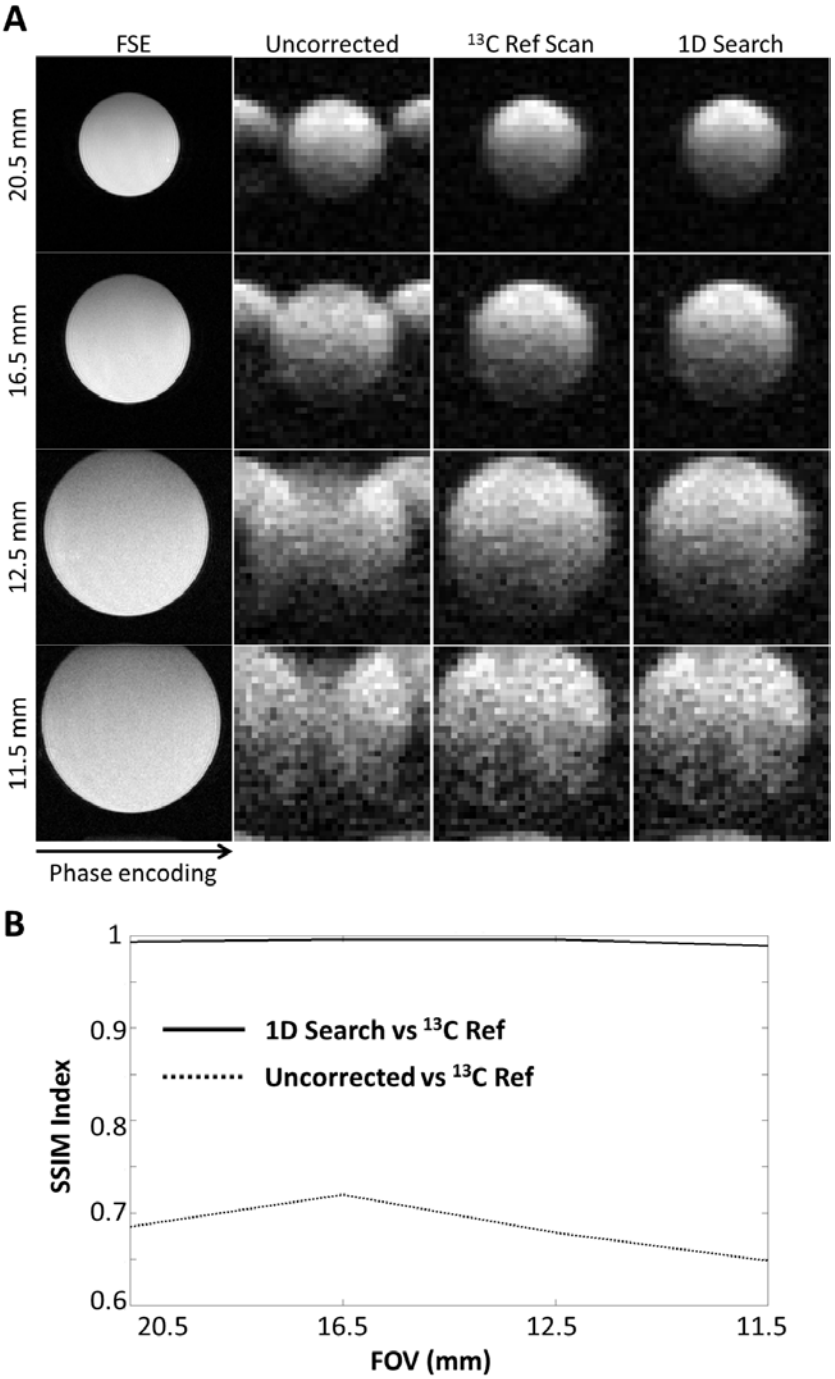

Figure 4.5: Phase correction methods for restricted FOVs

Performance of the proposed workflow with decreasing FOVs (20.5 mm to 11.5 mm) when compared to images corrected using a ^{13}C reference scan (A). Images were acquired from a centrally placed 10.5 mm diameter phantom. The ^{1}H FSE images provided a positional reference. The similarities of images acquired using the workflow and a ^{13}C reference scan were measured using the SSIM index and are shown in (B). SSIM = 1 indicates identical images.

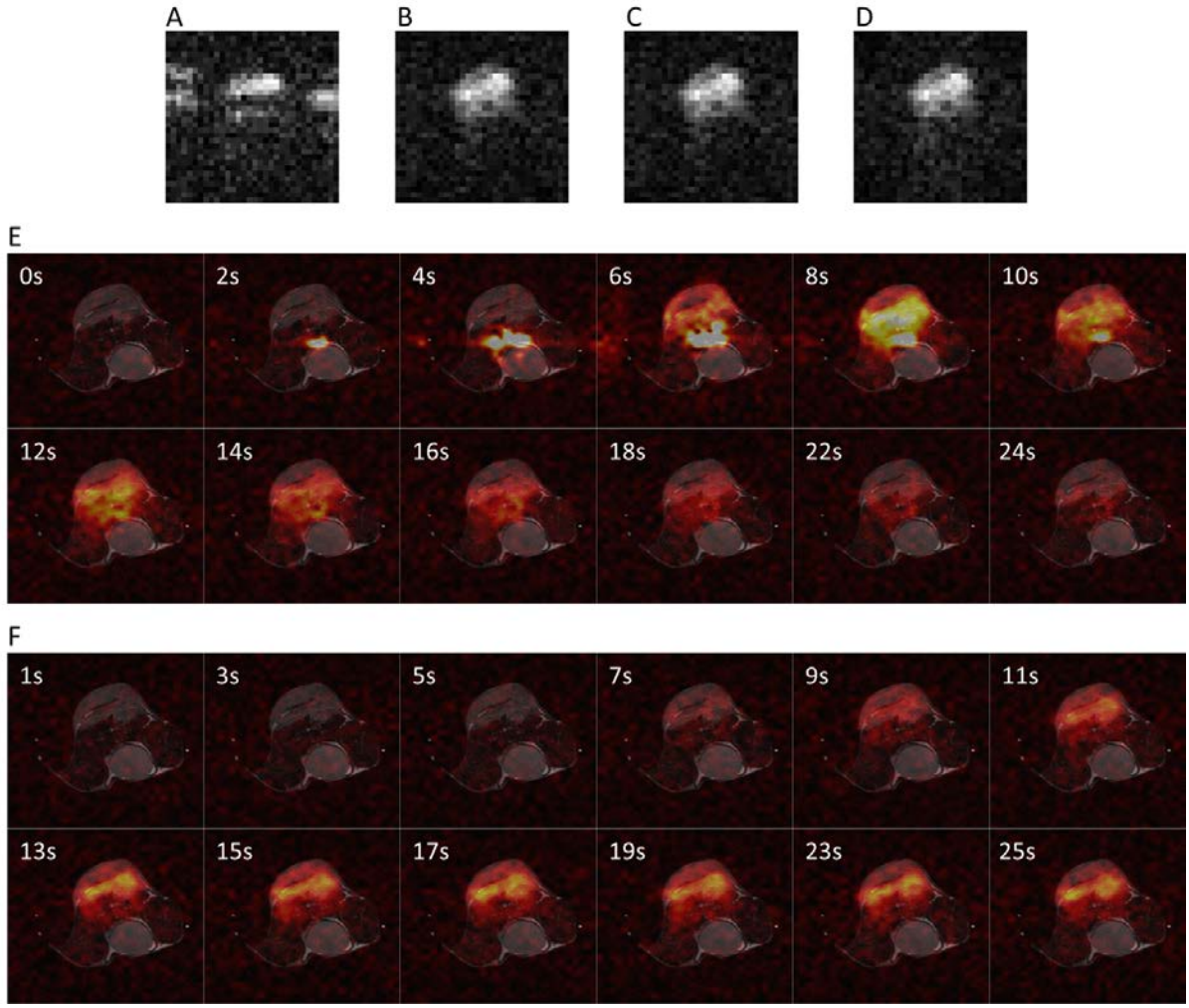

Figure 4.6: In vivo imaging results with the referenceless workflow
Representative images acquired following injection of hyperpolarized [1-^{13}C]pyruvate into an EL4-tumour bearing mouse. The [1-^{13}C]lactate image acquired at 10 s was used to search for the phase error correction coefficients. Images show a slice reconstructed without phase correction (A), phase corrected with ^{13}C reference scan data (B), corrected with a 1D search (C), and corrected with a 2D search (D). Panels (E) and (F) show dynamically acquired [1-^{13}C]pyruvate (E) and [1-^{13}C]lactate images (F), which were corrected using the phase error correction coefficients obtained from (C). Only data acquired from the first 25 seconds is shown. Note that images acquired at 20 and 21 seconds were used as ^{13}C reference scans and are not shown. ^{13}C signals in (E) and (F) were normalized to the pixel with the highest intensity in the [1-^{13}C]pyruvate images.

For the phantoms, the 1D search method resulted in images of similar quality to those obtained using a ^{13}C reference scan and integrated ^{13}C reference echoes, with a large FOV, a restricted FOV, and with multiple signal sources (Figure 4.3A). A quantitative comparison of residual ghosting showed similar ghost removal using all three methods, except that the 2D

search almost doubled residual ghosting, in comparison with the other methods, when there were multiple signal sources (Figure 4.3B). The images obtained using the proposed workflow with a 1D search showed a similar SNR compared to all the other methods and under all conditions (Figure 4.3C). Compared to the ^{13}C reference scan method residual ghosting was 1.3% versus 1.2% under well-shimmed conditions and 1.6% versus 1.5% under de-shimmed conditions (Figure 4.4). However, the images were better than images corrected using ^{1}H reference data when the magnetic field homogeneity was degraded: residual ghosting was 1.4% under well-shimmed and 3.8% under de-shimmed conditions (Figure 4.4) in images corrected using ^{1}H reference data.

The influence of FOV on images corrected using the 1D search and direct ^{13}C reference scan methods is shown in Figure 4.5A. Images corrected using either method were effectively identical. Image similarity was assessed using the Structural Similarity (SSIM) method [103,194] (Figure 4.5B; SSIM = 1 indicates identical images) which describes image similarities based on their luminance, contrasts, and structures. The SSIM indices were calculated using a downloaded Matlab script (http://www.cns.nyu.edu/~lcv/ssim/).

Images acquired in vivo were phase corrected using a ^{13}C reference scan and 1D/2D searches. For the [1-^{13}C]lactate images, 23 time points, and for the [1-^{13}C]pyruvate images, 10 time points, were selected from the dataset of each of three mice. Images at earlier and later time points were excluded since they were dominated by noise (Figure 4.6). The 1D and 2D search algorithms gave similar levels of ghosting as the ^{13}C reference scan method (Figure 4.7A). The similarity of dynamic [1-^{13}C]pyruvate and [1-^{13}C]lactate images, from an in vivo dataset, and phase corrected using the ^{13}C reference scan or 1D search methods, was demonstrated using the SSIM index (Figures 4.7B and 4.7C).

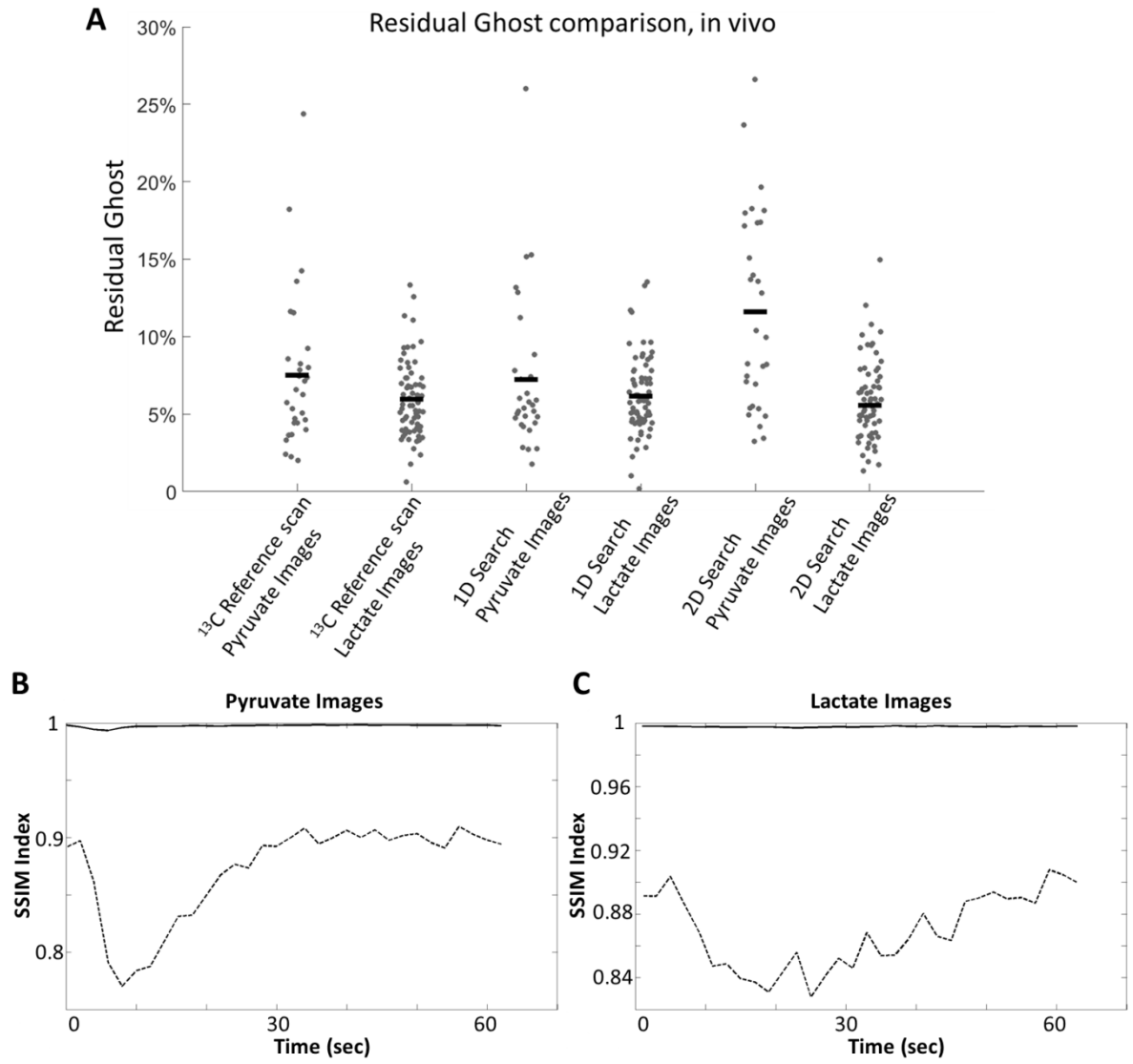

Figure 4.7: Quantitative analysis of the in vivo results
(A) Residual ghosting level in the lactate and pyruvate images acquired in vivo, where the images were phase corrected using a ^{13}C reference scan, 1D search, and 2D search. Both searches were performed on the [1-^{13}C]lactate image with highest SNR. The horizontal bars represent the mean value for that data cohort. The similarities (indicated with solid lines) between the images corrected with the ^{13}C reference scan and the images corrected using a 1D search were measured for both the [1-^{13}C]pyruvate (B) and [1-^{13}C]lactate (C) images taken from a representative in vivo dataset (SSIM indices ≈ 1). The dotted lines show the similarities between the uncorrected images and the images corrected using reference scans.

Phase correction using an exhaustive search in a late stage [1-^{13}C]pyruvate image (9th image) yielded results similar to those using a search in the [1-^{13}C]lactate image with the highest SNR, while a search in an early stage [1-^{13}C]pyruvate image (2nd image) led to

considerable residual ghosting (Figure 4.8). When the sum of the [1-^{13}C]pyruvate images collected over the time course was used, similar phase correction results were obtained with 6.2±2.6% (mean±S.D., 69 images in total, 23 images from each of three mice) and 7.2±5.0% (30 images in total, 10 images from each of three mice) residual ghosting in [1-^{13}C]lactate and [1-^{13}C]pyruvate images respectively. Similarly, an exhaustive search in the sum of the [1-^{13}C]lactate images gave 6.0±2.5% (n=69) and 8.1±5.0% (n=30) residual ghosting in the [1-^{13}C]lactate and [1-^{13}C]pyruvate images.

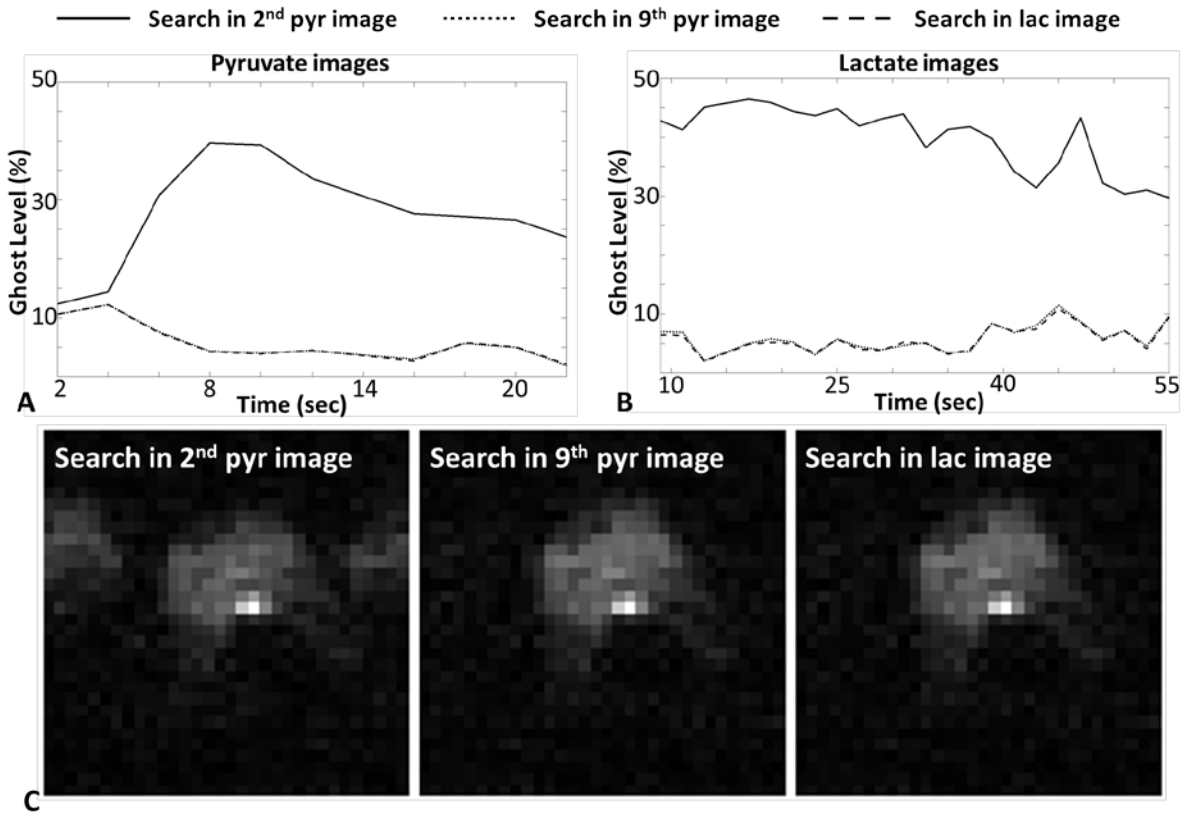

Figure 4.8: Exhaustive search in pyruvate images
Representative measurements of residual ghosting in (A) [1-^{13}C]pyruvate and (B) [1-^{13}C]lactate images. The phase corrections were performed based on a 1D exhaustive search in the [1-^{13}C]lactate image with the highest SNR, a [1-^{13}C]pyruvate image acquired at an early stage (2 s), and a [1-^{13}C]pyruvate image acquired at a late stage (16 s) following injection. Representative images from each dataset are displayed in (C).

To evaluate the tolerance of the proposed workflow to differences in SNR, a 1D search was performed on each of the lactate images from an in vivo dataset. The coefficients obtained were then applied to the lactate image with the highest SNR. Residual ghosting in

this latter image and the coefficients obtained from the individual images were then plotted against the SNR of the individual images (Figures 4.9A and 4.9B). The workflow yielded a ghost-free image when the SNR of the image from which the coefficients were calculated was greater than 4.7. Below this value the coefficients obtained appeared to be random. I also applied a range of coefficient pairs (from $-\pi/2$ to $\pi/2$ for each coefficient) to the same [1-^{13}C]lactate image with the highest SNR and found that the algorithm is relatively tolerant to a range of values for α provided that β is measured correctly, as was also observed using the other phase correction methods (Figure 4.3).

The 1D search method would have had a clear SNR benefit in vivo when compared to phase correction using integrated ^{13}C echoes. Although I did not collect integrated reference ^{13}C echoes in vivo, with the reference scan data I can calculate the signal loss that would have resulted from their collection by comparing the signal intensities in the echo acquired at the centre of k space and three echoes later. The 1D search method showed a SNR benefit of 17.0±9.1% (n=3) for [1-^{13}C]pyruvate and 15.3±8.7% (n=3) for [1-^{13}C]lactate.

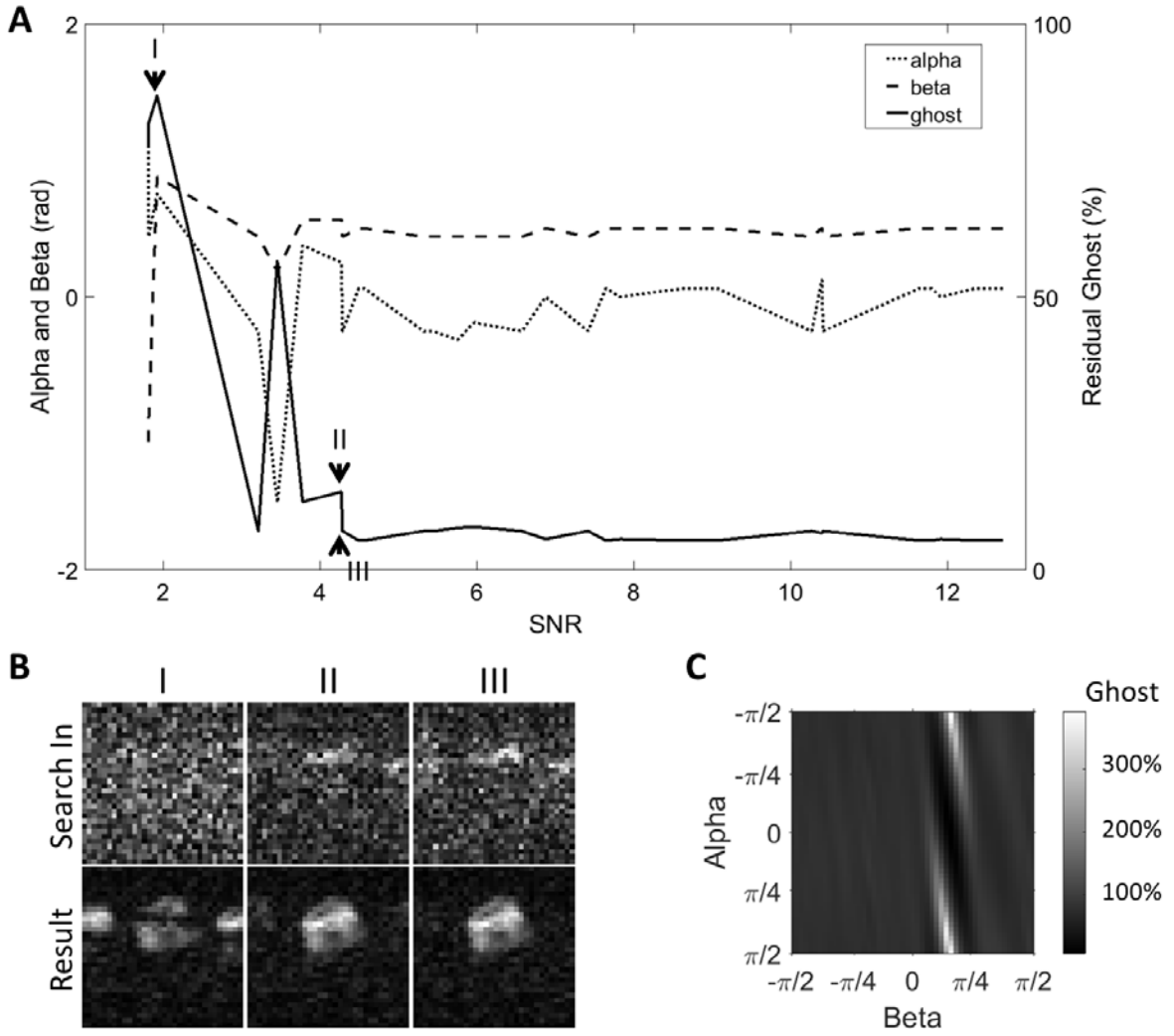

Figure 4.9: Robustness in case of low SNR images
(A) The tolerance of the 1D search to differences in SNR was examined using the lactate images from one representative in vivo dataset. The search was performed on each of the lactate images (with SNRs ranging from 1.8 to 12.7) and the pair of phase correction coefficients obtained was then applied to the lactate image with the highest SNR. The resulting image was free of ghosting until the SNR of the individual lactate images was less than 4.7. The α and β pairs obtained from the searches in each image are also plotted. (B) Representative lactate images with different SNRs (upper row), which were used to determine α and β pairs, and the corresponding phase corrected lactate image with the highest SNR. (C) Residual ghosting in the same image when corrected using different pairs of phase correction coefficients.

4.4. Discussion

The proposed method reliably removed Nyquist ghosting in ^{13}C echo planar images acquired from phantoms and in vivo, showing similar removal of ghosting as the direct ^{13}C

reference scan method (Figures 4.3-4.7). To my experience, the remaining blurring and ringing artefacts in the phase encode direction in Figure 4.3A are the result of zero-filling during image reconstruction. Compared to conjugate reconstruction for partial k-space acquisition, zero-filling improves the SNR but causes image blurring and Gibbs ringing. Residual artefacts in the phase encoding direction in [1-^{13}C]pyruvate images acquired in vivo at 4 and 6 seconds (Figure 4.6E) were primarily from high intensity signals in blood vessels, which were undergoing rapid flow and could not be accurately phase corrected. The same artefacts were observed in images corrected using a ^{13}C reference scan. The proposed workflow does not require sacrifice of a time point in the limited image acquisition time window, potentially giving a more accurate estimate of kinetic rate constants. Although not important in this case, where signals from pyruvate and lactate were relatively long lived, this will be more important when there is more rapid polarization decay.

1D search and 2D search

A 2D search offered no advantage over a 1D search. Residual ghosting levels in in vivo [1-^{13}C]pyruvate images were 6.3±3.4% (n=30) and 11.4±5.9% (n=30) for the 1D and 2D searches respectively and for the in vivo [1-^{13}C]lactate images 6.0±2.5% (n=69) and 5.6±3.0% (n=69). However, noise levels were higher in images corrected using the 2D search due to matrix inversion in the phase correction algorithm. For a modern MR scanner, where the gradient coils are well shielded and cross term eddy currents are minimized, correction in both the readout and phase encoding directions is not required [189,190]. In the phantom experiments where there were multiple signal sources, the 2D search method led to more residual ghosting than the 1D search, especially from the small phantom. This was because the 2D search relied on local ghost minimization for each line in the frequency encode direction, which could be biased in lines where little ghosting was present. This problem could be resolved by explicitly drawing ROIs for each signal source. When this was done the residual ghosting was reduced to 1.9%, which is similar to that obtained with all the other methods. With oblique plane imaging the 2D search method may be needed to correct for k-space displacement in both the kx and ky directions. However, even in this situation the 1D search method should perform better than the abovementioned reference scan methods as it directly minimizes ghosting in the image domain.

1D search and other phase correction methods

The 1D search is based on a linear phase error model that is similar to that of the widely used reference scan method, which has proven to be robust on modern clinical systems. The 1D search renders a reference proton scan [103] unnecessary, which can be compromised by differences in the spatial location of the ^{1}H and ^{13}C signals. Eddy currents, a major source of Nyquist ghosting, are spatially dependent, and a mismatch in location may render the proton reference scan less than optimal for phase correction (see Figure 4.4). This mismatch may arise because the ^{1}H image has only 1/4 of the FOV of the ^{13}C image in the readout direction. Although a four times larger receiver bandwidth could be used in the ^{1}H image, in order to keep the same readout FOV, the high sampling rate needed may exceed hardware capability (a large receiver bandwidth is already used for EPI to reduce image distortion). For example, a 250 kHz bandwidth in ^{13}C imaging will require a 1 MHz receiver bandwidth in the ^{1}H reference scan. Moreover, if the same slice selection gradients are used in acquisition of the ^{1}H reference, the slice thickness will also be 1/4 of that in the ^{13}C image. A smaller (~1/4) slice selection gradient could be used but then the eddy currents would be different. Since these eddy currents may interfere with the eddy currents generated by the readout gradients, different phase errors may be measured in the ^{1}H reference than are actually present in the ^{13}C image.

An EPI sequence with integrated ^{13}C reference echoes [96,97] does not use up a dynamic time point, acquires reference data directly from the ^{13}C signals, and requires no operator intervention. However, it sacrifices image SNR by prolonging TE. The method proposed here has therefore a substantial SNR benefit in vivo over the integrated reference echoes method. Although clinical systems usually have lower field strengths than the 7T used here, and therefore longer T_2*, this SNR benefit may still hold in clinical applications because of the slower gradient slew rates and the potential need for a larger acquisition matrix to cover a larger FOV. The integrated reference echoes may be inserted at the end of the acquisition train so that the SNR of the image would not be sacrificed, however this may result in very low signal from the reference echoes.

Reference data could be acquired from a ^{13}C phantom. However, a phantom further complicates the spectrum and places more restrictions on SpSp pulse design. Using an image from the phantom for phase-correction will also potentially suffer from the same problems as using a proton reference image, where differences in spatial location and eddy currents could lead to sub-optimal calculation of the phase correction coefficients.

The exhaustive search method has not been widely used in the clinic for proton MRI mainly because many imaging objects cover most of the FOV and, if there is a large overlap between object and ghosting, the exhaustive search method can sometimes lead to heavily biased results. This is not the case for ^{13}C imaging because the ^{13}C signals are usually localized. This was the case here where labeled lactate was observed predominantly in the tumour, but is also the case for other hyperpolarized ^{13}C-labeled imaging agents, such as the perfusion markers ^{13}C-labeled urea [134,151] and [1-^{13}C]2-methylpropan-2-ol (t-butanol) [195,196]. For perfusion imaging, searches in early stage images may lead to biased correction coefficients because of rapid motion of the marker in the blood vessels, as is indicated by the results shown in Figure 4.8. These effects could potentially be reduced by using EPI-based sequences designed to reduce flow artefacts [197]. Motion artefacts could also be minimized by summing images over the time course. As shown here, a search based on the summed [1-^{13}C]pyruvate images yielded similar phase correction coefficients to those determined from the [1-^{13}C]lactate image with the highest SNR.

Robustness

The proposed method works well with a restricted FOV, provided that the target metabolite signal does not cover the whole FOV, and also with multiple signal sources. The method worked well even when the object filled up to ≈ 90% of the FOV in both the phase and frequency encoding directions. Images of a centrally placed 10.5 mm diameter phantom phase corrected using a 1D search were similar to those phase corrected using a ^{13}C reference scan between FOVs of 11.5 and 20 mm (SSIM>0.98) (Figure 4.5). In unusual cases where no major localized signal is present and multiple signal-containing regions are located close to both ends in the phase encode direction, such that there is no ghosting outside the selected object region, an entropy-based convergence criterion [189,192] may be needed.

However, an entropy-based criterion was not used in my implementation because it can result in an image shifted by half a FOV when large eddy currents are present, as the entropy is the same for the original and shifted images.

The second step in Figure 4.1A is just one of the possible implementations of the proposed workflow. The workflow is relatively tolerant to the selection of images in which to perform the 1D exhaustive search. Similar correction results were obtained from a search in the [1-^{13}C]lactate image with the highest signal intensity, from a late phase [1-^{13}C]pyruvate image, and from [1-^{13}C]pyruvate and [1-^{13}C]lactate images that have been summed over the entire time course. The workflow is also tolerant to a wide range of SNR conditions (Figure 4.9A).

Gross shifts and distortions in the ^{13}C image caused by B_0 field drift and inhomogeneity may lead to a spatial mismatch between ^{13}C and ^{1}H images (i.e., the object in ^{13}C image falls partially outside the ROI drawn in the ^{1}H image). Fortunately, the relatively small ^{13}C gyromagnetic ratio and small acquisition matrix (hence high bandwidth in the phase encode direction) makes it less prone to off-resonance effects. Ramp-sampling can also help by further increasing the phase encode bandwidth. For example, the 552 μs echo spacing used here results in an immunity to a B_0 shift of ±57 Hz, which can be increased to ~±100 Hz when ramp-sampling is used with the same gradient amplitude and slew-rate. In comparison, the ^{13}C linewidth of [1-^{13}C]lactate in vivo is usually around 40 Hz on our system. Dynamic central frequency measurements could be incorporated into the experiment by using a simple pulse-acquire sequence with a small flip angle, although to my experience this is unnecessary as the central frequency does not vary much (usually a few Hertz) after the injection of the hyperpolarized media.

Compatibility

The proposed workflow could readily be applied to 3D EPI, where the 1D search could be performed per slice and the correction coefficients obtained applied to each kx-ky-z hybrid k-space (the hybrid k-space is obtained by Fourier transforming the 3D k-space in the kz direction). The method is also compatible with multi-channel receive coils. Provided that accelerated acquisition is not used, the search need only be on data from a single channel.

When there are strong eddy currents in Y or Z then a search may be needed in the image from each channel. In the case of parallel imaging, the phase correction coefficients in each iteration of the search should be implemented in the sensitivity map in a similar way to that described by Chen et al [190]. The image should then be reconstructed with this modified sensitivity map for each iteration of the search.

4.5. Conclusion

I have developed a referenceless EPI workflow for hyperpolarized ^{13}C labeled metabolites. This workflow is as capable of removing Nyquist ghosting as a ^{13}C reference scan, at no cost of extra data acquisition during dynamic imaging, and would be straightforward to implement in clinical imaging.

5. Dynamic ^{1}H imaging of hyperpolarized [1-^{13}C]lactate

5.1. Introduction

To date most DNP studies have focused on ^{13}C imaging, while in the clinic ^{1}H is the nucleus that is most widely used in MRI. This is because, as described in Section 1.3, ^{13}C is a better hyperpolarization target than ^{1}H due to its much longer T_1. On the other hand, ^{1}H is a better imaging target as it has ~4 times higher gyromagnetic ratio than ^{13}C. The difference in gyromagnetic ratios, and therefore resonance frequencies, means that ^{13}C imaging requires an extra RF transmitter and receiver, in addition to the proton channel, and a more powerful gradient set. In addition, the lower gyromagnetic ratio of ^{13}C means that the SNR is lower than for ^{1}H. Detection of hyperpolarized methyl protons in lactate would give, for the same level of polarization, a significant increase in SNR compared to direct detection of the ^{13}C-labeled C1 carbon. However, direct hyperpolarization of ^{1}H is difficult due to its relatively short T_1; the T_1 of the lactate methyl protons in vivo at 4.7 T is about 1.7 s [198]. Therefore the feasibility of transferring nuclear spin polarization from the hyperpolarized ^{13}C nucleus to ^{1}H has been explored. Frydman et al used a spatially encoded ultra-fast HSQC (heteronuclear single quantum coherence) experiment for ^{1}H detection of hyperpolarized ^{13}C nuclei in high-resolution solution experiments in vitro [199,200]. Sarkar et al used a reverse INEPT (insensitive nuclei enhanced by polarization transfer) sequence for proton detection of hyperpolarized ^{15}N choline [201] and Harris et al used a spatially selective variant of this experiment to monitor the kinetics of choline phosphorylation catalysed by choline kinase in vitro [202]. Recently, Dzien et al used a reverse INEPT sequence to study pyruvate decarboxylase activity in cultures of *S. cerevisiae* following injection of hyperpolarized [U-$^{2}H_3$, 2-^{13}C]pyruvate [203]. Chekmenev et al [204] used a refocused INEPT sequence, in spectroscopic studies in solution, to transfer hyperpolarization from ^{13}C to ^{1}H in [1-^{13}C]succinate-d_2 and in 2,2,3,3-tetrafluoropropyl 1-^{13}C-propionate-d_3 and Truong et al [205] used the same sequence, in conjunction with 2D fast steady state free precession ^{1}H imaging, to image hyperpolarized 2-hydroxyethyl-^{13}C-propionate-$d_{2,3,3}$ in a phantom. Mishkovsky et al have described spectroscopic studies in vivo, in which a heteronuclear polarization transfer sequence was used to acquire localized ^{1}H spectra of hyperpolarized [1-^{13}C]acetate in rat brain, in which polarization was transferred from the carboxyl carbon to

the methyl protons [206]. Here I demonstrate dynamic imaging of the conversion of hyperpolarized [1-^{13}C]pyruvate to [1-^{13}C]lactate in tumour-bearing mice, in which labelled lactate in the tumour was detected via its methyl protons using a modified reverse INEPT experiment, where a double dual spin echo sequence ensured acquisition of a fully refocused echo (Figure 5.1).

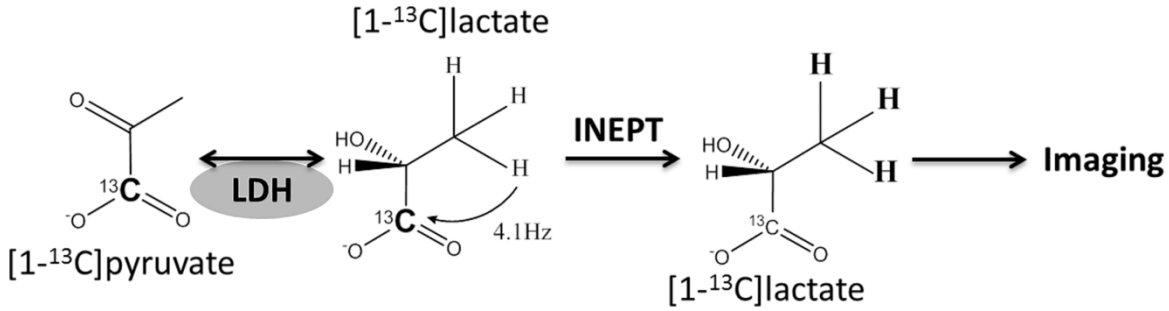

Figure 5.1: Workflow of the proton detection experiment
Lactate dehydrogenase (LDH) catalyses exchange of hyperpolarized ^{13}C label between injected hyperpolarized [1-^{13}C]pyruvate and the endogenous lactate pool. Hyperpolarized [1-^{13}C]lactate is detected by transferring hyperpolarization from the C1 carbon to the spin-coupled (J = 4.1 Hz) methyl protons in a reverse INEPT experiment.

5.2. Methods

Transfer of polarization from lactate $^{13}C_1$ to the methyl protons

I first discuss the use of a reverse-INEPT sequence to transfer the longitudinal polarization of a single spin-1/2 nucleus of isotopic species S to transverse polarization of a set of *N* magnetically equivalent spins-1/2 of isotopic species I. The conventional reverse INEPT pulse sequence has the following form:

$$90_{\mathrm{x}}(\mathrm{S}) - \tau_1/2 - 180_{\mathrm{x}}(\mathrm{I},\mathrm{S}) - \tau_1/2 - 90_{\mathrm{y}}(\mathrm{I},\mathrm{S}) - \tau_2/2 - 180_{\mathrm{x}}(\mathrm{I},\mathrm{S}) - \tau_2/2 \qquad 5.1$$

In the absence of relaxation, and assuming infinitely short pulses, the polarization transfer amplitude from the S-spin to the *N* magnetically equivalent I-spins is given by the functions [207,208]:

$$f_N(\theta_1, \theta_2) = (\cos\theta_1)^{N-1} \sin\theta_1 \sin\theta_2 \qquad 5.2$$

where the delays are expressed as angles $\theta_j = \pi J_{CH} \tau_j$. If the initial ^{13}C polarization level is denoted P_S, the maximum level of I-spin polarization and the optimal values of the time variables are given by:

$$\begin{cases} N = 1: P_I(\max) = P_S, & \text{at } \theta_1 = \theta_2 = 90° \\ N = 2: P_I(\max) = \dfrac{P_S}{2}, & \text{at } \theta_1 = 45°, \theta_2 = 90° \\ N = 3: P_I(\max) = \dfrac{2P_S}{3\sqrt{3}}, & \text{at } \theta_1 = \arctan\dfrac{1}{\sqrt{2}} \approx 35.3°, \theta_2 = 90° \end{cases} \qquad 5.3$$

The case N=1 is relevant to polarization transfer from lactate $^{13}C_1$ to the C2 proton. In the best case, the initial ^{13}C polarization level, P_S, is preserved upon transfer to the C2 proton, this leads to an enhancement in hyperpolarized magnetization by a factor $\gamma_I/\gamma_S \approx 3.97$, taking into account the relative gyromagnetic ratios of 1H and 13C (e.g., I is ^1H and S is ^{13}C). The case N=3 is relevant to polarization transfer from lactate $^{13}C_1$ to the methyl protons. In the best case, the methyl protons acquire a polarization of $0.385P_S$. The hyperpolarized magnetization is therefore enhanced by the factor $3 \times 0.385 \times \gamma_I/\gamma_S$, taking into account the number of polarized protons and the relative gyromagnetic ratios. Furthermore, optimal transfer to the methyl protons occurs at a much shorter τ_1 interval, assuming equal J-couplings. In fact, the coupling constant between the C1 carbon and the C3 methyl protons in [1-^{13}C]lactate is larger than the coupling constant with the C2 proton (3.2 Hz versus 4.1 Hz). In the absence of relaxation, the optimal value of τ_1 is therefore approximately 3 times shorter, and the achievable ^1H magnetization 15% larger, when the methyl protons are targeted, compared to the C2 proton. Since short pulse sequence intervals generally lead to smaller relaxation losses, the lactate methyl protons are a more promising target for polarization transfer than the C2 proton.

Pulse sequence

The pulse sequence (Figure 5.2A) starts with a saturation module on the proton resonances, so that unwanted signals from water and lipids are suppressed, followed by a double-dual-spin-echo (DDSE) INEPT preparation module, after which pre-phasing gradients are applied on both readout and phase encoding axes, followed by a symmetric echo-planar acquisition train [94]. The transmission coil in our setup could not be used to pulse simultaneously on ^{1}H and ^{13}C and therefore there was a delay between the ^{1}H and ^{13}C pulses, which otherwise would happen at the same time in a conventional INEPT sequence. In the DDSE-INEPT preparation sequence the ^{1}H and ^{13}C coherences evolve with the same phase as in a conventional INEPT sequence at each of the 90° pulses and at the end of the preparation period (Figure 5.2B).

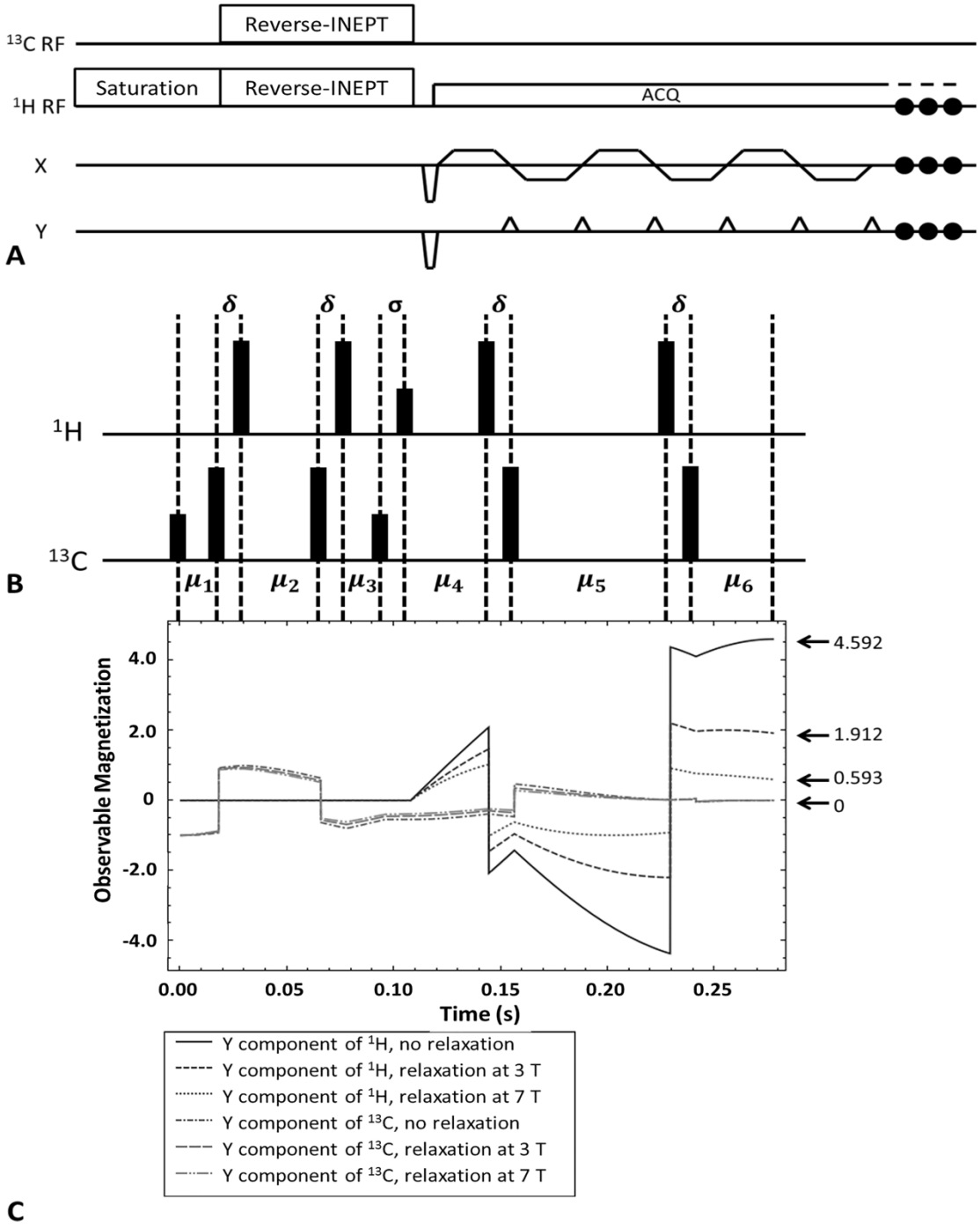

Figure 5.2: DDSE-INEPT sequence for polarization transfer

(A) Pulse sequence for transferring hyperpolarization from the C1 carbon to the methyl protons of lactate and imaging of the resulting hyperpolarized proton signal. (B) Pulse sequence for the double-dual-spin-echo INEPT module shown in (A). Shorter and longer bars refer to 90° and 180° pulses respectively. The 90° pulse on ^{1}H is the ^{1}H excitation pulse. The 1st and 2nd 90° pulses on ^{13}C are the ^{13}C excitation and flip-back pulses, respectively. The phases of the RF pulses are, in the order as displayed, $x, x, x, x, x, y, -y, x, x, x, x$. (C) Evolution of ^{13}C and ^{1}H y magnetizations in [1-^{13}C]lactate during the DDSE-INEPT module.

Three simulations are shown with: no relaxation, ^{1}H and ^{13}C T_1 and T_2 relaxation at 3T, and ^{1}H and ^{13}C T_1 and T_2 relaxation at 7T. The y component of the methyl group proton magnetization is shown.

If relaxation effects are neglected, maximum polarization transfer occurs when:

$$\begin{cases} \mu_1 + \mu_2 + \mu_3 - 2\delta = \operatorname{acos}\left(\sqrt{\frac{2}{3}}\right) \Big/ \pi J = 47.78 \text{ ms} \\ \mu_4 + \mu_5 + \mu_6 - 2\delta = \frac{1}{2J} = 121.952 \text{ ms} \end{cases} \quad 5.4$$

where δ is the centre-to-centre delay between a pair of ^{13}C and ^{1}H pulses. In order for spin echoes to be formed at the time of the second ^{13}C 90° pulse in the DDSE-INEPT module, when magnetization is flipped back along the z axis, and at the end of this module (at the end of μ_6) (Figure 5.2B), the timing must fulfil the following conditions:

$$\begin{cases} \mu_2 = \mu_1 + \mu_3 \\ \mu_5 = \mu_4 + \mu_6 \end{cases} \quad 5.5$$

Equations 5.4 and 5.5 determine the values of $\mu_1, \mu_2, \ldots, \mu_6$. The interval δ was kept to a minimum and was determined by the length of the ^{13}C flip-back and ^{1}H excitation pulses. The total duration of the DDSE-INEPT module, from the first ^{13}C pulse to the echo formed at the end of the module, was 278 ms.

The saturation module consisted of a 4 ms 90° sinc pulse, with a bandwidth of 8 kHz, followed immediately by a spoiler gradient in the slice direction. A 4 ms sinc-shaped pulse was designed with the SLR algorithm [159] for both excitation and flip-back of the ^{13}C coherences (the 1st and 2nd 90° pulses on ^{13}C). The bandwidth was 600 Hz to allow selective excitation of [1-^{13}C]lactate without perturbing the [1-^{13}C]pyruvate polarization. A sinc-shaped ^{1}H pulse was used for selective excitation of the lactate C3 methyl protons (the 1st 90° pulse on ^{1}H). The bandwidth was 1500 Hz in order to avoid excitation of the C2 and water protons. The ^{13}C and ^{1}H magnetizations were inverted using 10 ms adiabatic Hyperbolic-Secant (HS) pulses [180]. The bandwidth of the ^{13}C pulses was 8 kHz, so that

even far off-resonance [1-^{13}C]pyruvate magnetization (far from the magnet iso-centre) would experience full inversion and the hyperpolarization would not be destroyed by the pulses. For the ^{1}H pulses the bandwidth was only 1000 Hz, in order to avoid inversion of the C2 proton resonance (approximately 850 Hz from the C3 proton resonance).

The dual-spin-echo design was required because an adiabatic pulse results in a non-linear phase change across the swept frequency range, which can only be cancelled by another adiabatic pulse with the same waveform and RF power [112,179]. This sequence also ensures that the spin echo resulting from phase evolution induced by local B_0 field variations coincides with complete polarization transfer, under conditions where the ^{1}H and ^{13}C pulses cannot be applied simultaneously.

Simulation of the effects of relaxation

Evolution of the ^{13}C and ^{1}H polarizations during the DDSE-INEPT preparation block was simulated, in the weak-polarization limit, using the SpinDynamica platform (available online at www.SpinDynamica.soton.ac.uk) in Wolfram Mathematica (Wolfram Research, Inc., Mathematica, Version 10.4, Champaign, IL). For simplicity, shaped pulses were treated as being infinitely short and relaxation losses during the pulses were neglected. A relaxation model of uncorrelated random fields was used. Simulations were performed by Felix Kreis.

MR scanner

The same hardware setup was used as described in Section 2.2.

Phantom experiments

A 60 µl [1-^{13}C]lactate sample, containing 58 mg 50% w/w [1-^{13}C]lactate solution (Sigma-Aldrich, MO, USA), 15 mM OXØ63 (GE Healthcare, Amersham, UK), 1.2 mM Dotarem gadoterate meglumine (Dotarem; Guerbet, Roissy, France), and 20 µl 1/10 v/v DMSO (Sigma-Aldrich, MO, USA) was hyperpolarized for 2 hours using a Hypersense polarizer (Oxford Instruments, Abingdon, UK) at 1.2 K in a magnetic field of 3.35 T with microwave irradiation at 94.116 GHz. The hyperpolarized sample was then dissolved in 4 ml superheated PBS buffer and 0.5 ml was injected into an 18 mm inner diameter sphere filled

with H_2O. The final [1-^{13}C]lactate concentration in the phantom was then approximately 15 mM. Two spectra were acquired using the pulse sequence shown in Figure 5.2, but without the imaging gradients (Figure 5.3A). The delay between the INEPT preparation module and the beginning of signal acquisition was 170 ms, calculated from the centre of the 90° ^{1}H excitation pulse, which was set at the C3 ^{1}H resonance frequency (Figure 5.2B). Data were acquired into 2048 points covering a bandwidth of 12.5 kHz. In a second experiment hyperpolarized [1-^{13}C]lactate was injected and a series of echo planar images were acquired from the C3 ^{1}H resonance, with a time resolution of 2 s and starting 2 s after the completion of the lactate injection (a single image is shown in Figure 5.3B). The receiver bandwidth was 125 kHz and the echo spacing 400 µs. A FOV of 4x4 cm^2 covered a 32x32 data matrix, and the k-space centre was acquired after only 4 echoes in order to minimize TE (173 ms). A ^{1}H fast spin echo image was acquired (256x256, 4x4 cm^2, slice thickness 80 mm) in order to provide a positional reference.

Tumour model

The same tumour model was used as described in Section 2.2, prepared by Richard L. Hesketh and Deen Hu.

Dynamic imaging in vivo

The mouse was fasted for 6 hours before imaging [157], and warmed at 32 °C one hour prior to induction of anaesthesia using 1.5-2.5% isoflurane. The hyperpolarized [1-^{13}C]pyruvate sample was prepared as described in Section 2.2. The injection of hyperpolarized [1-^{13}C]pyruvate took 8 s, and imaging started 10 s after completion of the injection when a substantial amount of [1-^{13}C]lactate had already been generated from the injected [1-^{13}C]pyruvate. Images were acquired every 2 seconds and a total of 30 images were acquired, with the 7th acquisition used as a reference for EPI phase correction. Ninety-degree pulses were used for ^{13}C excitation and flip-back so that all of the [1-^{13}C]lactate polarization produced from the injected [1-^{13}C]pyruvate during each 2 s interval was detected in the ^{1}H image. A 90° flip angle was used for ^{1}H excitation in order to make full use of the transferred polarization. The same acquisition parameters were used for in vivo and phantom imaging.

T_2 weighted proton FSE images (16 slices, slice thickness 2 mm) with a 128x128 data matrix covering a 4×4 cm^2 FOV were acquired to provide a positional reference.

Image reconstruction

Phase correction was performed using the reference image data, as described in [94]. The partial k-space was then zero-filled from 20x32 to 32x32 before Fourier transform. Phase correction and image reconstruction were performed in Matlab (The Math Works, Natick, MA, USA).

5.3. Results

Hyperpolarized ^{13}C label is exchanged between injected hyperpolarized [1-^{13}C]pyruvate and the endogenous unlabelled lactate pool in the reaction catalysed by LDH (Figure 5.1A). Polarization was transferred from the C1 carbon to the indirectly coupled C3 methyl protons (J = 4.1 Hz) using a DDSE-INEPT sequence (Figure 5.2B) and the resulting hyperpolarized ^{1}H signal imaged using an EPI readout (Figure 5.2A). Simulations showed that evolution of the magnetization of the three magnetically equivalent methyl ^{1}H spins in [1-^{13}C]lactate under the four-spin coupling Hamiltonian, relative to the initial magnetization of the hyperpolarized ^{13}C spin, enhances the hyperpolarized magnetization by a factor of 4.6 and that this is decreased by relaxation to a factor of 1.9 at 3 T, and to 0.6 at 7 T (Figure 5.2C). The simulations that included relaxation were performed using the following published values for T_1 and T_2 at 3 and 7 T: T_2^{13C} (7 T) = 300 ms [172], T_2^{13C} (3 T) = 520 ms [209], T_2^{1H} (7 T) = 100ms [210], T_2^{1H} (3 T) = 256ms [211], T_1^{13C} (3T) = 45 s [113] and T_1^{1H} (4.7T) = 1.73 s [198].

^{1}H spectra and images acquired using the DDSE-INEPT sequence, following injection of hyperpolarized [1-^{13}C]lactate into a phantom, are shown in Figure 5.3. ^{1}H signal in the first acquisition (solid line in Figure 5.3A and image shown in Figure 5.3B) was approximately 10 times larger than in the second acquisition (dotted line in Figure 5.3A and image shown in Figure 5.3C) due to depletion of the ^{13}C hyperpolarization by the 90° ^{13}C excitation pulse. The methyl proton resonance shown in Figure 5.3A had a peak width at half height of about 35 Hz and therefore splitting due to ^{1}H and ^{13}C coupling was not resolved (the methyl

proton resonance of [1-^{13}C]lactate is split into a doublet by coupling to the C2 proton (J = 7.2 Hz) and these doublets are further split into doublets by coupling to the C1 ^{13}C (J = 4.1 Hz)). In the image this splitting of the methyl proton resonance will not compromise SNR if the k-space centre is acquired at the time when the spin echo is formed, where the image signal is then the integral of all the in-phase peaks. The SNR of the spectrum from the first acquisition was 8618, which decreased to 1560 for the second acquisition. The SNR for the first image was 586.4 and only 56.9 for the second. The spectrum and image SNRs were measured as the ratios between maximum and mean signals respectively and the standard deviation of the background noise [16]. There was no observable excitation of the water resonance, which should be about 1090 Hz away from the lactate methyl proton resonance. The residual signal observed in the second image (Figure 5.3C) appeared to be water signal from the injection line. The B_0 field was only shimmed over the spherical phantom. Water protons in the injection line may therefore have been off-resonance and excited by the transition band of the proton inversion pulses. The residual signal was spatially displaced from the injection line in the phase encoding direction, consistent with it being from off-resonance signal. The hyperpolarized [1-^{13}C]lactate solution (0.5 ml) was injected into the bottom of the sphere phantom, which contained 3 ml of water, and the first acquisition started 2 s after completion of the injection. The methyl proton signals were concentrated, therefore, at the bottom of the phantom.

Dynamic images of the methyl proton resonance of hyperpolarized [1-^{13}C]lactate were acquired using the DDSE-INEPT sequence following injection of hyperpolarized [1-^{13}C]pyruvate into an EL4 tumour-bearing mouse (Figure 5.4A). A series of images are shown in Figure 5.4A and an overlay of the first image, rendered in false colour, on an anatomic image acquired using a ^{1}H fast spin echo sequence is shown in Figure 5.4B. The ^{1}H signals from hyperpolarized [1-^{13}C]lactate were observed at the base of the tumour and adjacent to the body of the animal. I have observed a similar distribution of labelled lactate in this tumour model using direct ^{13}C detection. Unlike in the phantom, the hyperpolarized ^{13}C and ^{1}H signals in the tumour are sustained over time by inflow of hyperpolarized [1-^{13}C]pyruvate into the tumour from the rest of the animal.

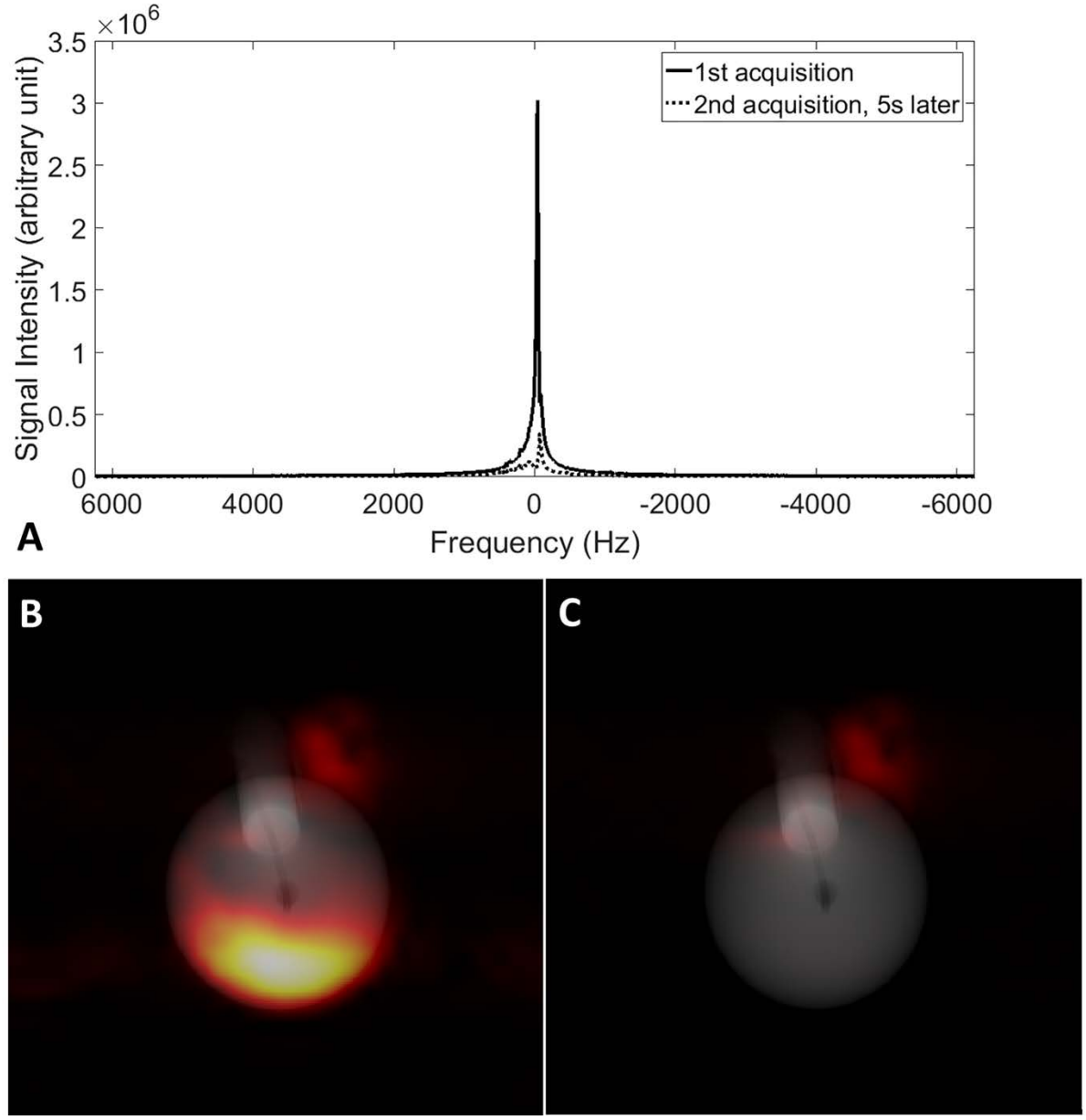

Figure 5.3: Phantom imaging with hyperpolarized [1-^{13}C]lactate

Phantom experiments with hyperpolarized [1-^{13}C]lactate. ^{1}H spectra acquired after injection of hyperpolarized [1-^{13}C]lactate into the phantom are shown in (A), where the ^{1}H excitation was set to the methyl proton resonance frequency. The second spectrum (dotted line) was acquired 5s later. Sequential methyl group ^{1}H images acquired after injection of hyperpolarized [1-^{13}C]lactate into the phantom are shown in (B) and (C). The lactate proton images in (B) and (C), which are rendered in colour, have been overlaid on a fast spin echo water ^{1}H image, which has been rendered in greyscale.

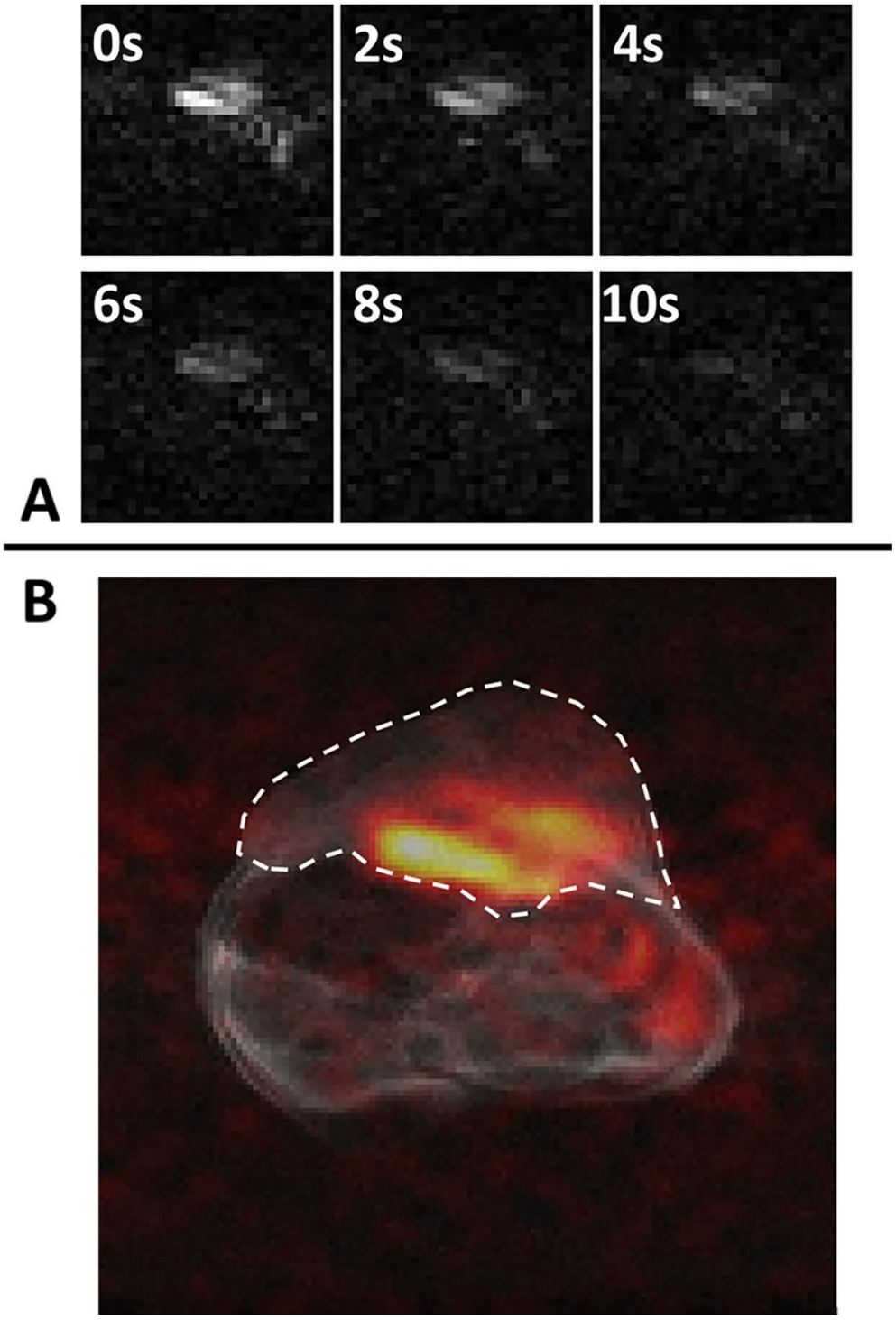

Figure 5.4: Dynamic in vivo acquisition after hyperpolarized [1-^{13}C]pyruvate injection
(A) Dynamic ^{1}H images of the lactate methyl protons acquired using the DDSE-INEPT sequence at the indicated times following injection of hyperpolarized [1-^{13}C]pyruvate into a tumour-bearing mouse. The first image (at 0 s) was acquired 2 s after completion of the injection, which took a total of 10 s. (B) The image in (A) acquired at 0 s and rendered in false colour overlaid on a fast spin echo ^{1}H image of tissue water, which is in greyscale. The tumour is outlined.

5.4. Discussion

The DDSE-INEPT pulse sequence transfers ^{13}C nuclear spin polarization in hyperpolarized [1-^{13}C]lactate from the $^{13}C_1$ carbon to the spin coupled methyl protons. The SNR on the lactate ^{1}H image acquired in vivo was 17 (Figure 5.4B), which is comparable to SNR values obtained previously in this tumour model with direct ^{13}C detection, where the SNR of ^{13}C images of [1-^{13}C]lactate acquired using a 90° pulse and summed over a 20 mm thick slab were between 13-20 [178]. However, these ^{13}C images were acquired using a 20 mm diameter surface coil placed immediately over the tumour whereas the ^{1}H images shown here were acquired using a 42 mm diameter ^{1}H and ^{13}C transmit/receive volume coil. Given the difficulty in ensuring equal coil efficiencies and in order to generalize the relevance of the measurements shown here for other field strengths the experiment was simulated. Simulation using published values for the T_1s and T_2s of the ^{1}H and ^{13}C nuclei in lactate in vivo, showed that transferring ^{13}C hyperpolarization into the methyl protons enhances the hyperpolarized magnetization by a factor of 4.6 and that this is decreased by relaxation to 1.9 at 3 T, and to 0.6 at 7 T, which was the field strength used here. The amplitude of the detected MR signal depends on this polarization but is also proportional to the precession frequency, since it is generated by electromagnetic induction in the receiver coil. Assuming identical coil efficiencies, then detecting spin polarization in ^{1}H rather than ^{13}C is beneficial due to the higher gyromagnetic ratio of the proton, γ_{1H}; for a given level of polarization, signal increases as $\sim\gamma^2$ [212] as magnetization is proportional to γ and, given the same magnetization, the current induced in the receiver coil is also proportional to γ. Hence, for the same level of polarization ^{1}H will generate an approximately 16 times larger signal in the receiver coil than ^{13}C. With the simulated values for the magnetizations, which includes T_1 and T_2 relaxation of the ^{13}C and ^{1}H spins, detection of the $^{13}C_1$ polarization via the methyl protons will increase the signal 7.6 fold at 3T and 2.4 fold at 7T. These numbers were obtained by multiplying the simulated magnetizations by four (the same operation was performed for all the SNR calculations shown below). However, noise also increases with frequency. Noise due to coil resistance, R_C, is proportional to the square root of the frequency of the induced alternating current whereas noise due to sample resistance, R_S, increases quadratically with frequency. Since the overall noise signal is proportional to

$\sqrt{R} = \sqrt{R_C + R_S}$, the SNR that takes account of sample and coil noise can be calculated as [213]:

$$SNR = \frac{v^2}{[\alpha a^2 v^{1/2} + \beta v^2 b^5]^{1/2}} \quad 5.6$$

where v is the Larmor frequency, a and b are coil geometry parameters, and α and β are weightings for the two sources of noise, where α represents coil noise and β sample noise. Assuming the same coil geometry, the SNR for ^{1}H is 11.3 ($16/\sqrt{2}$) times that for ^{13}C when sample noise is neglected (α = 1, β = 0). With the calculated ^{13}C and ^{1}H magnetizations this will give an SNR benefit when detecting ^{13}C hyperpolarization via the methyl protons of 5.4 times at 3T and 1.7 times at 7T (magnetization enhancement x 4 /$\sqrt{2}$, where the denominator is determined by coil noise, which is proportional to the fourth root of the Larmor frequency, as shown in Equation 5.6). If sample noise dominates (α = 0, β = 1) detection via ^{1}H gives an SNR benefit of only 4 times that of ^{13}C detection if relaxation is ignored and, given the calculated ^{13}C and ^{1}H magnetizations, the SNR benefit would decrease to 1.9 times at 3T and 0.6 times at 7T (4x magnetization enhancement / 4, where the denominator comes from the fact that sample noise is proportional to the Larmor frequency, as shown in Equation 5.6). Although sample noise is thought to dominate with relatively large imaging objects at high magnetic fields [214] this is evidently not the only source of noise since superconducting coils show an increased ^{1}H SNR of 2 to 5 fold at fields between 1.5 T and 9.4 T when compared to room temperature copper coils [215-217]. Therefore even at 7 T there may still be a SNR benefit in detecting hyperpolarized [1-^{13}C]lactate via the spin coupled methyl protons.

The dynamic images (Figure 5.4A) showed rapid signal decay as each acquisition sampled effectively all of the hyperpolarized signal from [1-^{13}C]lactate generated from hyperpolarized [1-^{13}C]pyruvate in the preceding 2 s. Such a rapid decay has been observed previously in saturation-recovery experiments, where following injection of hyperpolarized [1-^{13}C]pyruvate the [1-^{13}C]lactate produced was sampled with repeated spectrally selective 90° ^{13}C pulses [162]. This problem could be addressed by using a preparation module that

allows partial transfer of the polarization [218]. This would also allow serial observations of the pyruvate resonance, which is not possible with the reverse INEPT sequence since effectively all of the polarization is transferred following the first application of the pulse sequence. The simulation showed in Figure 5.2C shows that there is also the potential for shortening the DDSE-INEPT module, and thus reducing signal loss due to T_2 decay, since this may be affected without significantly reducing polarization transfer.

The longer ^{1}H and ^{13}C T_2 relaxation times at lower magnetic field strengths will improve the efficiency of polarization transfer and there may be a benefit in going to very low fields since there is evidence that these may be more sensitive for hyperpolarized contrast agents [219]. The four-fold higher ^{1}H gyromagnetic ratio means that there is a four-fold lower demand on the gradient system, which, with the availability of high quality proton receive coils, makes this an attractive technique for clinical translation.

5.5. Conclusion

In summary, I have demonstrated a DDSE-INEPT sequence that allows ^{1}H detection of hyperpolarized ^{13}C label exchange between injected hyperpolarized [1-^{13}C]pyruvate and the tumour lactate pool. Further incorporation of a spectrally-selective ^{1}H 90° pulse that flips the magnetization back along the Z axis at the end of the reverse INEPT preparation module would allow any ^{1}H imaging sequence to be used for signal detection. The sequence is fully compatible with clinical scanners that are already equipped for hyperpolarized ^{13}C imaging, where the lower field strengths and consequently longer relaxation times should improve sensitivity.

6. General Discussion and future work

6.1. High resolution imaging for hyperpolarized ^{13}C MRI

The sequences introduced in Chapters 2 and 3 have enabled high resolution imaging in all three dimensions for hyperpolarized ^{13}C MRI after a single excitation. These techniques hold promise for clinical translation, where the main challenge on a clinical system will be to keep the spirals to reasonable durations. Due to the nature of phase encoding in the z direction using blipped gradient trains, longer duration spirals will lead to image distortion in the z direction. To maintain a relatively high spatial resolution, while using a short spiral duration, the imaging FOV in the xy plane will need to be kept small. Since imaging objects in clinical applications are much larger than in mice, it will be important to restrict the excitation FOV in the xy plane in order to avoid wrap-around artefacts when a small FOV is used for acquisition. Since spectral selectivity will still be required for excitation, in order to resolve signals from different metabolites, a three dimensional selective (2 spatial dimensions and 1 spectral dimension) RF pulse will be required for excitation. A straightforward design for such an RF is a train of spirals that are chemical shift encoded, where each spiral repeatedly encodes the same xy plane [220]. The challenges in 3D pulse design are the limited gradient strength and slew rate on clinical systems, which could be 10 fold lower than on our pre-clinical system. A 3D excitation pulse that could be used to excite [1-^{13}C]pyruvate and [1-^{13}C]lactate at 3T on a clinical system was designed subject to a 40 mT/m maximum gradient strength and 200 T/m/s slew rate and is shown in Figure 6.1. An envelope pulse was first designed using the SLR algorithm and then discretely sampled by a train of 8 identical sub-pulses. The gradients were designed using the analytical method described by Glover et al [160] to encode a 8x8 cm^2 FOV given the hardware capabilities. The sub-pulse was then designed based on the excitation k-space trajectory [221]. The excitation profile of the pulse was simulated using the Hard-Pulse Approximation [159] where the pulse operation on the magnetization was taken as a series of rotations incurred by sampling the pulse at a 4 μs step size. With a 30.752 ms duration, this pulse excites an 8 cm diameter cylinder with a 72 Hz wide band at the target frequency in the spectrum, where the other metabolite, which is 390 Hz away, is not excited. The peak B_1 is only 7.99 μT, far below the hardware restrictions on clinical 3T systems. Slice selection could be

realized either by using refocusing pulses accompanied by slice selection gradients or a transmission or receive coil with restricted sensitivity in the z direction. On the acquisition side, when an 8 cm FOV is imaged (yellow square in Figure 6.1C), an isotropic resolution of 2.5x2.5x2.5 cm^3 could be achieved using the proposed sequences and the gradient constraints given above. The design and simulation were performed in Matlab using a custom written script. Despite the long duration of the pulse, T_2* decay would not be a concern as refocusing pulses are used to form spin echoes for signal acquisition. Alternatively, restricted FOV imaging could be achieved on the hardware side by using transmission or receive coils that have restricted sensitivity in the xy plane. These techniques could readily be implemented using clinical systems in the future.

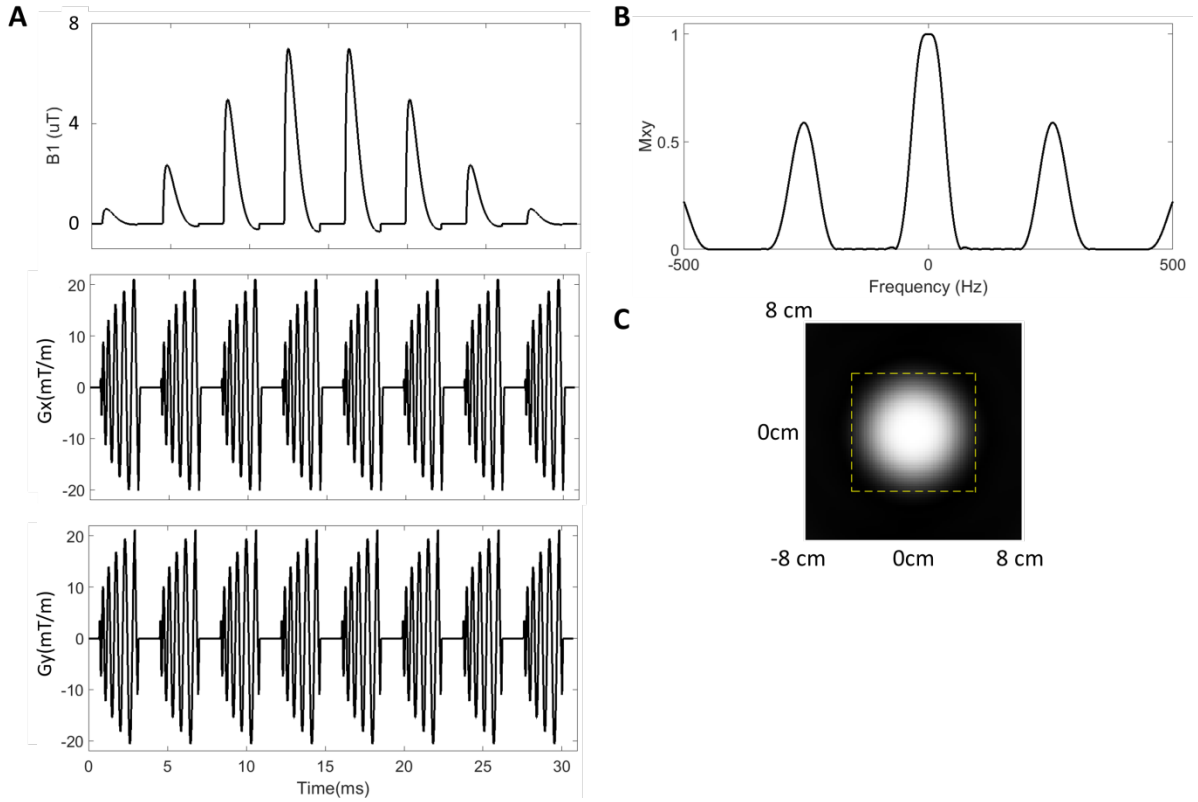

Figure 6.1: RF design for 2D-spatial-1D-spectral selectivity
(A) Three dimensional excitation pulse and its accompanying gradients on the x and y axes. (B) The frequency response of the pulse. (C) The spatial response of the pulse in the xy plane.

6.2. ^{1}H imaging of hyperpolarized ^{13}C labelled metabolites

With the DDSE-INEPT sequence described in Chapter 5, imaging hyperpolarized ^{13}C nuclei via spin-coupled protons is expected to have substantial SNR benefit over direct ^{13}C imaging, given the same starting polarization. This SNR benefit can be further enhanced if the sequence timing is optimized. As shown in Chapter 3, a dual spin echo design is not required for HS adiabatic inversion pulse to form a spin echo in the absence of slice selection gradients. In light of this, the DDSE design could be reduced to a regular INEPT sequence except that pulsing on ^{1}H and ^{13}C channels is not simultaneous, as shown in Figure 6.2A. This design, with shifted ^{1}H and ^{13}C pulsing, leads to a spin echo that is formed before complete transfer of the polarization. However, this is not a concern as transfer of the polarization at the spin echo is already >90%, if relaxation is ignored. The key concept in this design is to achieve a balance between T_2 loss, transfer of polarization, and signal loss due to the non-linear phase induced by the inversion pulses. Therefore, this sequence needs to be optimized based on the imaging agents and the imaging object, where the former determines T_2 and the latter affects shimming (signal loss due to non-linear phase depends on field homogeneity). The balance between T_2 loss and polarization transfer is simulated in Figure 6.2B, where signal loss due to non-linear phase is neglected for simplicity. A phantom experiment using this sequence following injection of hyperpolarized [1-^{13}C]lactate was performed and the results are shown in Figures 6.3C (acquired immediately after completion of the injection) and 6.3D (acquired 10s later), where images were acquired at the frequency of lactate methyl group protons and displayed with the same scaling. The [1-^{13}C]lactate sample was prepared in the same way as described in Chapter 5. The 8-fold signal decrease in the second acquisition indicated that the acquired signal was hyperpolarized. A positional reference was acquired with a FSE sequence on water protons before hyperpolarized [1-^{13}C]lactate injection, shown in Figure 6.2E.

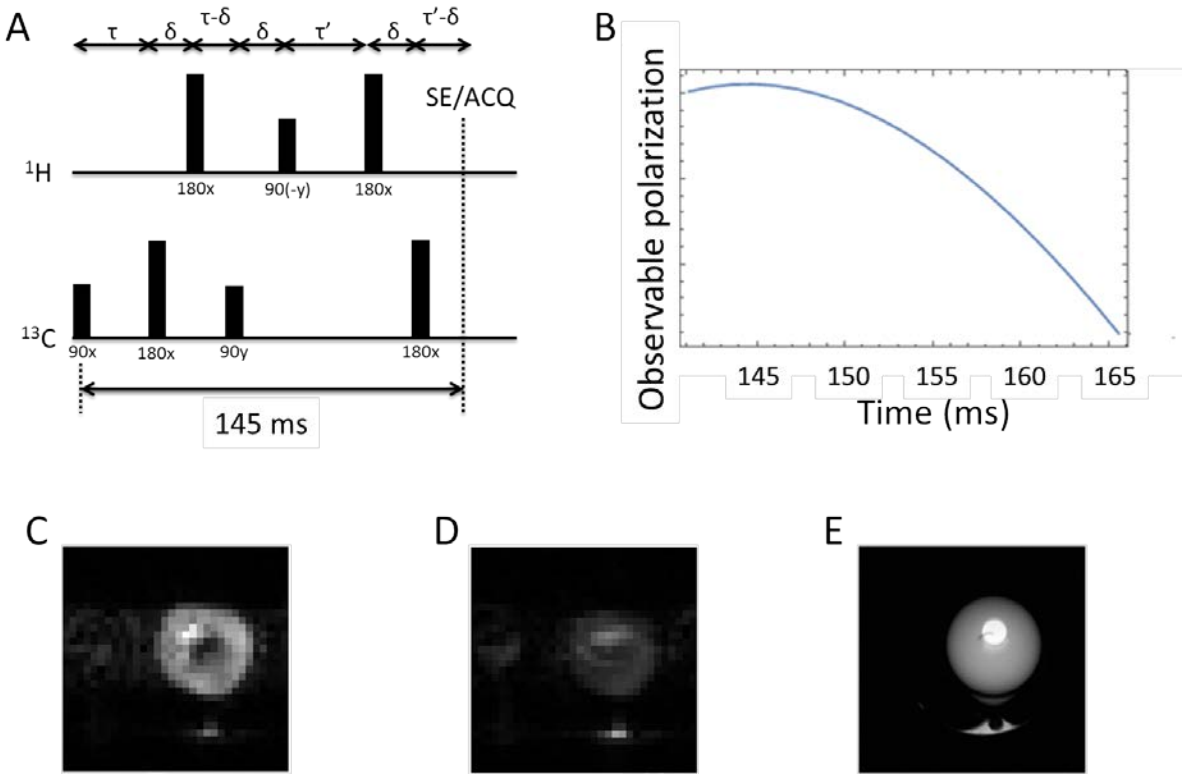

Figure 6.2: INEPT preparation with optimized timing
(A) INEPT sequence with non-simultaneous $^{1}H/^{13}C$ pulsing and optimized timing. (B) The observable polarization on 1H peaks at 145 ms, assuming a T_2 of 100 ms. (C) First acquisition in phantom imaging after hyperpolarized [1-^{13}C]lactate injection, where hyperpolarization was transferred from 13C to methyl protons using the optimized INEPT sequence and signal acquired with EPI trajectory as described in Chapter 5. (D) Second acquisition in the same experiment, where signal strength was only 1/8 of that in (C). (E) Positional reference of phantom, acquired with FSE at water proton frequency.

The technique described in Chapter 5 could readily be implemented on clinical scanners. To comply with the B_1 limitations of the ^{13}C transmission coil (Rapid $^{13}C/^{1}H$ Head Coil MR750, Rapid Biomedical GMBH, Rimpar, Germany) on our 3T system (99 μT, GE MR750), I re-designed the inversion pulses such that the bandwidth was reduced to 6 kHz from 10 kHz while the duration was kept at 10 ms. I inserted the inversion pulses into the EPI sequence (epi.e) to replace the regular preparation and excitation pulses. The modified sequence had separate RF power control on ^{1}H and ^{13}C channels and the pulses on both channels were used in the SAR calculation. Experiments were conducted by injecting hyperpolarized [1-^{13}C]pyruvate into a Falcon tube phantom via plastic tubing. Both the phantom and tubing were filled with a solution of NADH (4.4 mM) and LDH (12.5 U/ml) so

that there was rapid conversion of the injected [1-^{13}C]pyruvate into [1-^{13}C]lactate. The resulting ^{13}C hyperpolarization in [1-^{13}C]lactate was then transferred to the methyl group protons by the sequence. A series of images were acquired at the methyl group proton frequency with a 5 s TR, as shown in Figure 6.3, while a positional reference ^{1}H image (shown as the last image) was acquired with a regular EPI sequence before the [1-^{13}C]pyruvate injection. Hyperpolarized ^{1}H signals, decaying with time, could be observed inside both the phantom and the tubing. Signal could be still observed after the first acquisition because there was continued conversion of the injected [1-^{13}C]pyruvate into [1-^{13}C]lactate. For this experiment, a research grade fluid path (GE Healthcare, Milwaukee, WI, USA) was filled with 100 μl [1-^{13}C]pyruvic acid, 15 mM trityl radical AH111501 (GE Healthcare) and 30 ml dissolution fluid containing 1 g/L EDTA (GE Healthcare). The sample was polarized in a SPINlab hyperpolarizer (GE Healthcare) at ~0.9 K and 5 T for 1.5 hours and was then dissolved in 1.4 ml neutralization medium containing 0.72 M NaOH, 0.4 M Tris buffer, and 0.1 g/L EDTA [184]. Future scans in patients and volunteers are scheduled in order to further validate this technique.

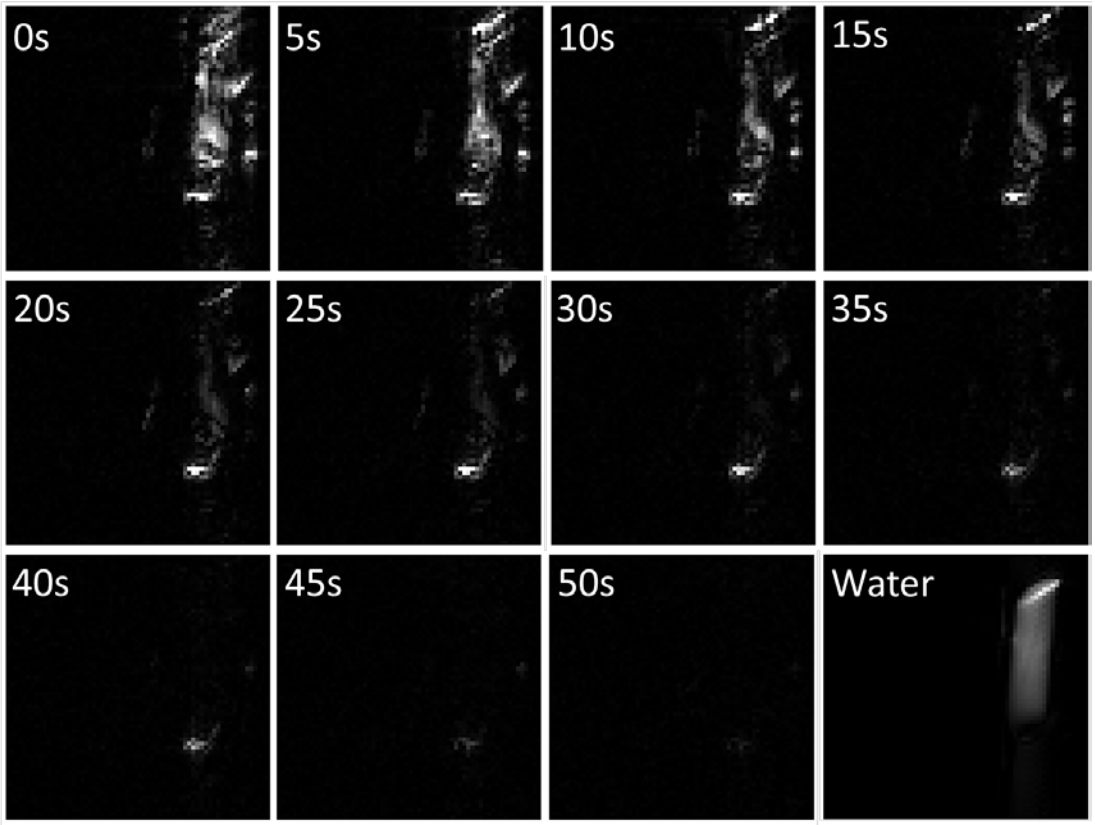

Figure 6.3: Dynamic polarization transfer imaging on a clinical system
Images acquired on a clinical 3T system at the lactate methyl proton resonance frequency following injection of hyperpolarized [1-^{13}C]pyruvate into a phantom containing LDH and NADH (TR = 5 s). A positional reference ^{1}H image, displayed as the last image, was acquired with a regular EPI sequence at the water proton resonance frequency prior to [1-^{13}C]pyruvate injection.

6.3. Monitoring LDH activity without [1-^{13}C]pyruvate injection

A potential limitation of using pyruvate as the imaging agent is that it is injected at supra-physiological concentrations. In the first clinical study [27] hyperpolarized [1-^{13}C]-pyruvate was injected to achieve a plasma concentration of 1.5 mM. In contrast, the normal concentration of pyruvate in human blood is 0.061+/-0.024mM [222]. This supra-physiological concentration is undesirable as it may temporarily alter metabolism, although there is no evidence of toxicity [26]. On the other hand, tumours usually have a large lactate concentration. Chen et al used hyperpolarized [1-^{13}C]lactate to probe pyruvate-lactate conversion [113], however the small pyruvate pool size led to only low levels of pyruvate labelling and hence a low SNR. Kennedy et al explored the feasibility of using lactate alone

to measure the LDH activity [222] by using double-labelled lactate, with both a ^{13}C nucleus at the C1 position and ^{2}H in place the protons (L-[1-^{13}C, U-^{2}H]lactate). Exchange of deuterium label was measured between the injected and endogenous lactate pools via the lactate-pyruvate conversion (as shown in Figure 6.4).

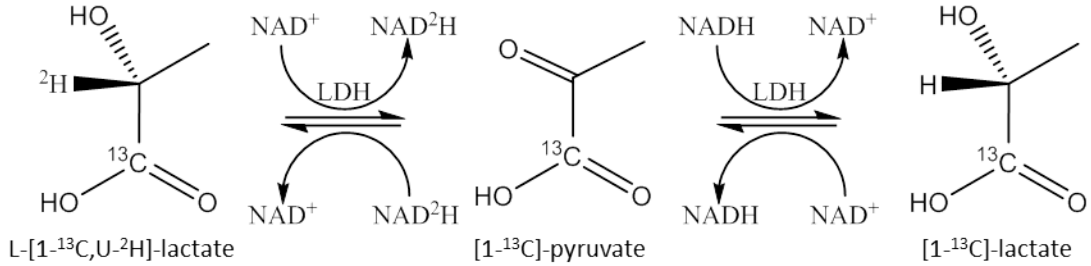

Figure 6.4: Monitoring LDH activity using L-[1-^{13}C,U-^{2}H]-lactate
Exchange of deuterium label between injected and endogenous lactate, through the interconversion of lactate and pyruvate.

The original study of Kennedy et al acquired spectra from the whole tumour, without any spatial information. This is not satisfactory for clinical use, due to the metabolic heterogeneity of tumours and the increased information that would have been available from acquiring two or three dimensional images. I have extended this concept with an imaging sequence, which is shown in Figure 6.5B. Figure 6.5A shows the sequence used in Kennedy's study.

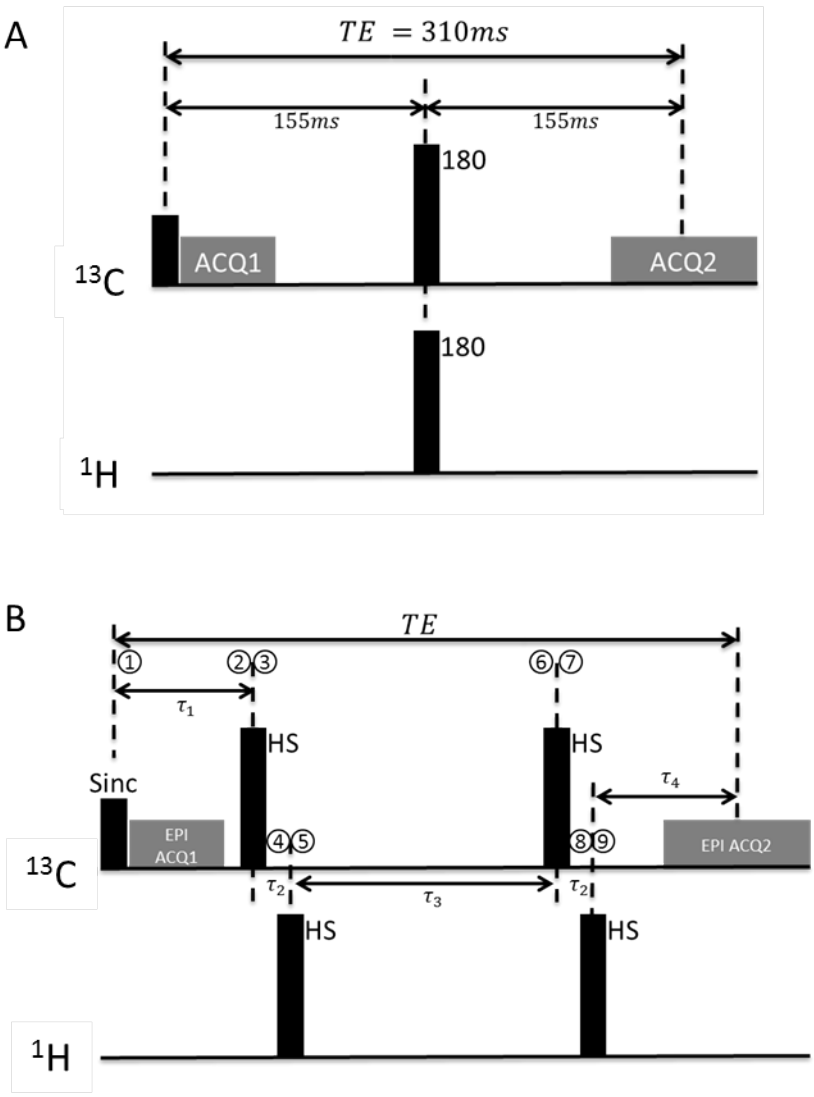

Figure 6.5: Sequence design for L-[1-^{13}C,U-^{2}H]-lactate experiment
Carbon-Observed-Proton-Edited (COPE) sequences for L-[1-^{13}C, U-^{2}H]lactate imaging. (A) The NMR sequence used in the literature. (B) A dual-spin-echo sequence for 2D imaging.

In practice, the RF coil system used in my experiment does not support simultaneous pulsing on carbon and proton channels. In addition, it requires a delay to allow the system to switch from the carbon channel to the proton channel. The dual-spin-echo design allowed a full inversion of the ^{13}C phase in the protonated lactate while the phase of the ^{13}C in the deuterated lactate was unaffected as the ^{1}H pulse has no effect on the ^{2}H spins. An additional scan is required using the same sequence but with ^{1}H inversion pulses turned off so that signals from deuterated and protonated lactate are both fully refocused. A subtraction between the two acquisitions then reveals the signal for protonated lactate

while adding the signal from the acquisitions recovers the signal from deuterated lactate. To achieve these phase modulations, the sequence needed to be timed as:

$$\begin{cases} \tau_1 + \tau_3 + \tau_4 - 2\tau_2 = 1/J_{CH} = 310\ \text{ms} \\ \tau_3 = \tau_1 + \tau_4 \end{cases} \quad 6.1$$

where J_{CH} is 3.2 Hz, the coupling constant between the C1 position ^{13}C and the C2 position ^{1}H. The parameter τ_2 is determined by the delay between the ^{13}C and ^{1}H pulses, which was 5 ms in my implementation, and the duration of the pulses. Adiabatic pulses with Hyperbolic-Secant modulation were used for both ^{13}C and ^{1}H inversion pulses to ensure insensitivity to B_0 and B_1 inhomogeneity. For ^{13}C inversion a 10 ms pulse with 2400 Hz bandwidth was used and for ^{1}H inversion a 10 ms pulse with a 1000 Hz bandwidth was used. Hence τ_2 was 15 ms, and TE was 370 ms. The sequence was calibrated on a phantom filled with 5 M [1-^{13}C]lactate with ^{1}H inversion pulses turned on and off respectively. Since the sample under observation contained protonated lactate only and no deuterated lactate, the sequence with ^{1}H inversion pulses turned on would edit the phase evolution of the observed signal with a time-dependent effect. The TE required to achieve full phase inversion was measured to be 376 ms, very close to the theoretically expected value. In fact, phase inversion of the protonated lactate resonance had already been achieved (97%) when TE was 350 ms, leading to much less T_2 decay than if a TE of 376 ms had been used. In vivo experiments with this sequence need to be conducted once L-[1-^{13}C, U-^{2}H]lactate can be produced consistently. Clinical studies will be scheduled once promising results are obtained from an in vivo study with tumour-bearing mice.

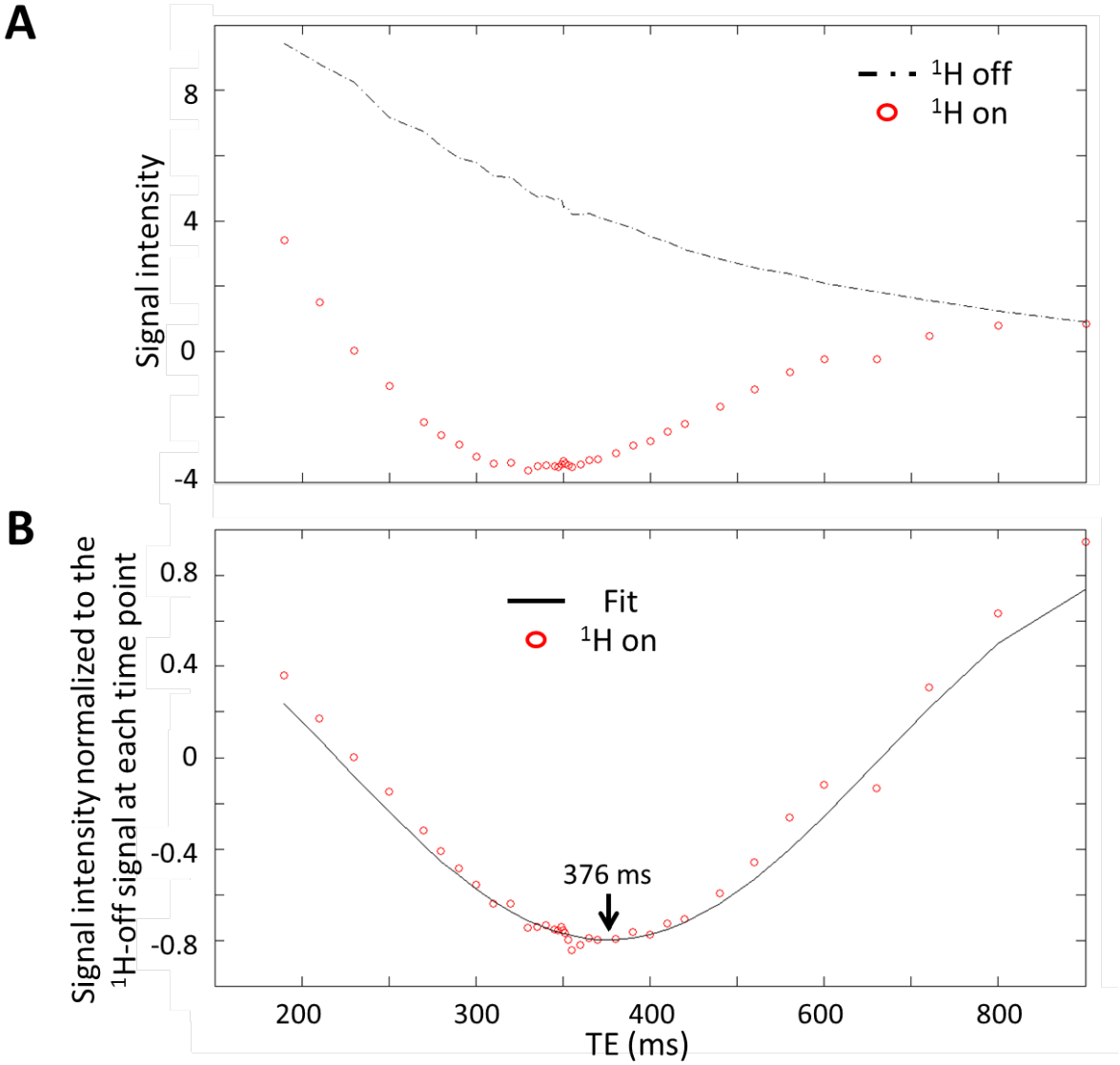

Figure 6.6: Optimal TE for L-[1-^{13}C,U-^{2}H]-lactate experiment
Measurement of signal inversion in a protonated [1-^{13}C]lactate phantom with the COPE sequence. (A) Signal obtained ± a proton pulse. (B) Signal with the proton pulse on (normalized to the signal with the proton pulse off) fitted to the theoretical cosine function. Fitting the acquired data to the expected theoretical signal evolution revealed that full phase inversion should happen when TE = 376 ms.

6.4. Conclusion

In conclusion, I have developed high resolution imaging sequences for hyperpolarized ^{13}C labelled metabolites that acquire a three dimensional image for individual metabolites after a single excitation. I have proposed a referenceless workflow for EPI phase correction in hyperpolarized ^{13}C MRI based on the *a priori* knowledge of the possible signal locations

from the proton image, which make it unnecessary to acquire extra data for Nyquist ghost removal. I have shown that ^{1}H detection of the hyperpolarized ^{13}C signal has SNR benefits over direct ^{13}C detection and can be implemented on current clinical MRI systems. All these techniques hold promise for clinical imaging, as presented in the general discussion. I have also initiated work on imaging L-[1-^{13}C, U-^{2}H]lactate, as an alternative probe to [1-^{13}C]pyruvate for imaging LDH activity. However, further work is required for this to be used for in vivo and clinical imaging.

References

1. Ferlay J, Soerjomataram I, Dikshit R, Eser S, Mathers C, Rebelo M, Parkin DM, Forman D, Bray F. Cancer incidence and mortality worldwide: sources, methods and major patterns in GLOBOCAN 2012. Int J Cancer 2015;136(5):E359-386.

2. Zagars GK, Schultheiss TE, Peters LJ. Inter-tumor heterogeneity and radiation dose-control curves. Radiother Oncol 1987;8(4):353-361.

3. Marusyk A, Almendro V, Polyak K. Intra-tumour heterogeneity: a looking glass for cancer? Nat Rev Cancer 2012;12(5):323-334.

4. Brindle K. New approaches for imaging tumour responses to treatment. Nat Rev Cancer 2008;8(2):94-107.

5. O'Connor JP, Rose CJ, Waterton JC, Carano RA, Parker GJ, Jackson A. Imaging intratumor heterogeneity: role in therapy response, resistance, and clinical outcome. Clin Cancer Res 2015;21(2):249-257.

6. Michaelis LC, Ratain MJ. Measuring response in a post-RECIST world: from black and white to shades of grey. Nat Rev Cancer 2006;6(5):409-414.

7. Eisenhauer EA, Therasse P, Bogaerts J, Schwartz LH, Sargent D, Ford R, Dancey J, Arbuck S, Gwyther S, Mooney M, Rubinstein L, Shankar L, Dodd L, Kaplan R, Lacombe D, Verweij J. New response evaluation criteria in solid tumours: revised RECIST guideline (version 1.1). Eur J Cancer 2009;45(2):228-247.

8. Brindle K. Watching tumours gasp and die with MRI: the promise of hyperpolarised 13C MR spectroscopic imaging. Br J Radiol 2012;85(1014):697-708.

9. Hanahan D, Weinberg RA. Hallmarks of cancer: the next generation. Cell 2011;144(5):646-674.

10. Rozental JM, Levine RL, Nickles RJ, Dobkin JA. Glucose uptake by gliomas after treatment. A positron emission tomographic study. Arch Neurol 1989;46(12):1302-1307.

11. Rozental JM, Levine RL, Mehta MP, Kinsella TJ, Levin AB, Algan O, Mendoza M, Hanson JM, Schrader DA, Nickles RJ. Early changes in tumor metabolism after treatment: the effects of stereotactic radiotherapy. Int J Radiat Oncol Biol Phys 1991;20(5):1053-1060.

12. Gadian DG, Radda GK. NMR studies of tissue metabolism. Annu Rev Biochem 1981;50:69-83.

13. Howe FA, Barton SJ, Cudlip SA, Stubbs M, Saunders DE, Murphy M, Wilkins P, Opstad KS, Doyle VL, McLean MA, Bell BA, Griffiths JR. Metabolic profiles of human brain tumors using quantitative in vivo 1H magnetic resonance spectroscopy. Magn Reson Med 2003;49(2):223-232.

14. Hensley CT, Faubert B, Yuan Q, Lev-Cohain N, Jin E, Kim J, Jiang L, Ko B, Skelton R, Loudat L, Wodzak M, Klimko C, McMillan E, Butt Y, Ni M, Oliver D, Torrealba J, Malloy CR, Kernstine K, Lenkinski RE, DeBerardinis RJ. Metabolic Heterogeneity in Human Lung Tumors. Cell 2016;164(4):681-694.

15. Hensley CT, Wasti AT, DeBerardinis RJ. Glutamine and cancer: cell biology, physiology, and clinical opportunities. J Clin Invest 2013;123(9):3678-3684.

16. Ardenkjaer-Larsen JH, Fridlund B, Gram A, Hansson G, Hansson L, Lerche MH, Servin R, Thaning M, Golman K. Increase in signal-to-noise ratio of > 10,000 times in liquid-state NMR. Proc Natl Acad Sci U S A 2003;100(18):10158-10163.

17. Levitt MH. Ensemble of spins-1/2. Spin dynamics: John Wiley & Sons, Ltd; 2008. p 259-294.

18. Le Guennec A, Tea I, Antheaume I, Martineau E, Charrier B, Pathan M, Akoka S, Giraudeau P. Fast determination of absolute metabolite concentrations by spatially encoded 2D NMR: application to breast cancer cell extracts. Anal Chem 2012;84(24):10831-10837.

19. Wenckebach WT. The solid effect. Appl Magn Reson 2008;34:227-235.

20. Ni QZ, Daviso E, Can TV, Markhasin E, Jawla SK, Swager TM, Temkin RJ, Herzfeld J, Griffin RG. High frequency dynamic nuclear polarization. Acc Chem Res 2013;46(9):1933-1941.

21. Levitt MH. Relaxation. Spin dynamics: John Wiley & Sons, Ltd; 2008. p 543-595.

22. Wenckebach WT. Dynamic nuclear polarization via thermal mixing: Beyond the high temperature approximation. J Magn Reson 2017;277:68-78.

23. Meier S, Jensen PR, Karlsson M, Lerche MH. Hyperpolarized NMR probes for biological assays. Sensors (Basel) 2014;14(1):1576-1597.

24. Brindle KM, Bohndiek SE, Gallagher FA, Kettunen MI. Tumor imaging using hyperpolarized 13C magnetic resonance spectroscopy. Magn Reson Med 2011;66(2):505-519.

25. Ardenkjaer-Larsen JH, Laustsen C, Bowen S, Rizi R. Hyperpolarized H2O MR angiography. Magn Reson Med 2014;71(1):50-56.

26. Brindle KM. Imaging metabolism with hyperpolarized 13C-labeled cell substrates. J Am Chem Soc 2015;137(20):6418-6427.

27. Nelson SJ, Kurhanewicz J, Vigneron DB, Larson PE, Harzstark AL, Ferrone M, van Criekinge M, Chang JW, Bok R, Park I, Reed G, Carvajal L, Small EJ, Munster P, Weinberg VK, Ardenkjaer-Larsen JH, Chen AP, Hurd RE, Odegardstuen LI, Robb FJ, Tropp J, Murray JA. Metabolic imaging of patients with prostate cancer using hyperpolarized [1-13C]pyruvate. Sci Transl Med 2013;5(198):198ra108.

28. Cunningham CH, Lau JY, Chen AP, Geraghty BJ, Perks WJ, Roifman I, Wright GA, Connelly KA. Hyperpolarized 13C Metabolic MRI of the Human Heart: Initial Experience. Circ Res 2016;119(11):1177-1182.

29. Aggarwal R, Vigneron DB, Kurhanewicz J. Hyperpolarized 1-[13C]-Pyruvate Magnetic Resonance Imaging Detects an Early Metabolic Response to Androgen Ablation Therapy in Prostate Cancer. Eur Urol 2017.

30. Vander Heiden MG, Cantley LC, Thompson CB. Understanding the Warburg effect: the metabolic requirements of cell proliferation. Science 2009;324(5930):1029-1033.

31. Lunt SY, Vander Heiden MG. Aerobic glycolysis: meeting the metabolic requirements of cell proliferation. Annu Rev Cell Dev Biol 2011;27:441-464.

32. Schulze A, Harris AL. How cancer metabolism is tuned for proliferation and vulnerable to disruption. Nature 2012;491(7424):364-373.

33. Kroemer G, Pouyssegur J. Tumor cell metabolism: cancer's Achilles' heel. Cancer Cell 2008;13(6):472-482.

34. Kim JW, Tchernyshyov I, Semenza GL, Dang CV. HIF-1-mediated expression of pyruvate dehydrogenase kinase: a metabolic switch required for cellular adaptation to hypoxia. Cell Metab 2006;3(3):177-185.

35. Day SE, Kettunen MI, Gallagher FA, Hu DE, Lerche M, Wolber J, Golman K, Ardenkjaer-Larsen JH, Brindle KM. Detecting tumor response to treatment using hyperpolarized 13C magnetic resonance imaging and spectroscopy. Nat Med 2007;13(11):1382-1387.

36. Day SE, Kettunen MI, Cherukuri MK, Mitchell JB, Lizak MJ, Morris HD, Matsumoto S, Koretsky AP, Brindle KM. Detecting response of rat C6 glioma tumors to radiotherapy using hyperpolarized [1- 13C]pyruvate and 13C magnetic resonance spectroscopic imaging. Magn Reson Med 2011;65(2):557-563.

37. Saito K, Matsumoto S, Takakusagi Y, Matsuo M, Morris HD, Lizak MJ, Munasinghe JP, Devasahayam N, Subramanian S, Mitchell JB, Krishna MC. 13C-MR Spectroscopic Imaging with Hyperpolarized [1-13C]pyruvate Detects Early Response to Radiotherapy in SCC Tumors and HT-29 Tumors. Clin Cancer Res 2015;21(22):5073-5081.

38. Ward CS, Venkatesh HS, Chaumeil MM, Brandes AH, Vancriekinge M, Dafni H, Sukumar S, Nelson SJ, Vigneron DB, Kurhanewicz J, James CD, Haas-Kogan DA, Ronen SM. Noninvasive detection of target modulation following phosphatidylinositol 3-kinase inhibition using hyperpolarized 13C magnetic resonance spectroscopy. Cancer Res 2010;70(4):1296-1305.

39. Rajeshkumar NV, Dutta P, Yabuuchi S, de Wilde RF, Martinez GV, Le A, Kamphorst JJ, Rabinowitz JD, Jain SK, Hidalgo M, Dang CV, Gillies RJ, Maitra A. Therapeutic

Targeting of the Warburg Effect in Pancreatic Cancer Relies on an Absence of p53 Function. Cancer Res 2015;75(16):3355-3364.

40. Bohndiek SE, Kettunen MI, Hu DE, Brindle KM. Hyperpolarized 13C spectroscopy detects early changes in tumor vasculature and metabolism after VEGF neutralization. Cancer Res 2012;72(4):854-864.

41. Park JM, Spielman DM, Josan S, Jang T, Merchant M, Hurd RE, Mayer D, Recht LD. Hyperpolarized 13C-lactate to 13C-bicarbonate ratio as a biomarker for monitoring the acute response of anti-vascular endothelial growth factor (anti-VEGF) treatment. NMR Biomed 2016;29(5):650-659.

42. Albers MJ, Bok R, Chen AP, Cunningham CH, Zierhut ML, Zhang VY, Kohler SJ, Tropp J, Hurd RE, Yen YF, Nelson SJ, Vigneron DB, Kurhanewicz J. Hyperpolarized 13C lactate, pyruvate, and alanine: noninvasive biomarkers for prostate cancer detection and grading. Cancer Res 2008;68(20):8607-8615.

43. Serrao EM, Kettunen MI, Rodrigues TB, Dzien P, Wright AJ, Gopinathan A, Gallagher FA, Lewis DY, Frese KK, Almeida J, Howat WJ, Tuveson DA, Brindle KM. MRI with hyperpolarised [1-13C]pyruvate detects advanced pancreatic preneoplasia prior to invasive disease in a mouse model. Gut 2016;65(3):465-475.

44. Schroeder MA, Cochlin LE, Heather LC, Clarke K, Radda GK, Tyler DJ. In vivo assessment of pyruvate dehydrogenase flux in the heart using hyperpolarized carbon-13 magnetic resonance. Proc Natl Acad Sci U S A 2008;105(33):12051-12056.

45. Laustsen C, Ostergaard JA, Lauritzen MH, Norregaard R, Bowen S, Sogaard LV, Flyvbjerg A, Pedersen M, Ardenkjaer-Larsen JH. Assessment of early diabetic renal changes with hyperpolarized [1-13C]pyruvate. Diabetes Metab Res Rev 2013;29(2):125-129.

46. Lau AZ, Miller JJ, Tyler DJ. Mapping of intracellular pH in the in vivo rodent heart using hyperpolarized [1-13C]pyruvate. Magn Reson Med 2017;77(5):1810-1817.

47. Laustsen C, Hansen ES, Kjaergaard U, Bertelsen LB, Ringgaard S, Stodkilde-Jorgensen H. Acute porcine renal metabolic effect of endogastric soft drink administration assessed with hyperpolarized [1-13C]pyruvate. Magn Reson Med 2015;74(2):558-563.

48. Gallagher FA, Kettunen MI, Day SE, Lerche M, Brindle KM. 13C MR spectroscopy measurements of glutaminase activity in human hepatocellular carcinoma cells using hyperpolarized 13C-labeled glutamine. Magn Reson Med 2008;60(2):253-257.

49. Gallagher FA, Kettunen MI, Day SE, Hu DE, Ardenkjaer-Larsen JH, Zandt R, Jensen PR, Karlsson M, Golman K, Lerche MH, Brindle KM. Magnetic resonance imaging of pH in vivo using hyperpolarized 13C-labelled bicarbonate. Nature 2008;453(7197):940-943.

50. Gallagher FA, Sladen H, Kettunen MI, Serrao EM, Rodrigues TB, Wright A, Gill AB, McGuire S, Booth TC, Boren J, McIntyre A, Miller JL, Lee SH, Honess D, Day SE, Hu DE,

Howat WJ, Harris AL, Brindle KM. Carbonic Anhydrase Activity Monitored In Vivo by Hyperpolarized 13C-Magnetic Resonance Spectroscopy Demonstrates Its Importance for pH Regulation in Tumors. Cancer Res 2015;75(19):4109-4118.

51. Gallagher FA, Kettunen MI, Hu DE, Jensen PR, Zandt RI, Karlsson M, Gisselsson A, Nelson SK, Witney TH, Bohndiek SE, Hansson G, Peitersen T, Lerche MH, Brindle KM. Production of hyperpolarized [1,4-13C2]malate from [1,4-13C2]fumarate is a marker of cell necrosis and treatment response in tumors. Proc Natl Acad Sci U S A 2009;106(47):19801-19806.

52. Bohndiek SE, Kettunen MI, Hu DE, Witney TH, Kennedy BW, Gallagher FA, Brindle KM. Detection of tumor response to a vascular disrupting agent by hyperpolarized 13C magnetic resonance spectroscopy. Mol Cancer Ther 2010;9(12):3278-3288.

53. Bohndiek SE, Kettunen MI, Hu DE, Kennedy BW, Boren J, Gallagher FA, Brindle KM. Hyperpolarized [1-13C]-ascorbic and dehydroascorbic acid: vitamin C as a probe for imaging redox status in vivo. J Am Chem Soc 2011;133(30):11795-11801.

54. Timm KN, Hu DE, Williams M, Wright AJ, Kettunen MI, Kennedy BW, Larkin TJ, Dzien P, Marco-Rius I, Bohndiek SE, Brindle KM. Assessing Oxidative Stress in Tumors by Measuring the Rate of Hyperpolarized [1-13C]Dehydroascorbic Acid Reduction Using 13C Magnetic Resonance Spectroscopy. J Biol Chem 2017;292(5):1737-1748.

55. Gallagher FA, Kettunen MI, Day SE, Hu DE, Karlsson M, Gisselsson A, Lerche MH, Brindle KM. Detection of tumor glutamate metabolism in vivo using 13C magnetic resonance spectroscopy and hyperpolarized [1-13C]glutamate. Magn Reson Med 2011;66(1):18-23.

56. Rodrigues TB, Serrao EM, Kennedy BW, Hu DE, Kettunen MI, Brindle KM. Magnetic resonance imaging of tumor glycolysis using hyperpolarized 13C-labeled glucose. Nat Med 2014;20(1):93-97.

57. Timm KN, Hartl J, Keller MA, Hu DE, Kettunen MI, Rodrigues TB, Ralser M, Brindle KM. Hyperpolarized [U-2H, U-13C]Glucose reports on glycolytic and pentose phosphate pathway activity in EL4 tumors and glycolytic activity in yeast cells. Magn Reson Med 2015;74(6):1543-1547.

58. Chaumeil MM, Larson PE, Yoshihara HA, Danforth OM, Vigneron DB, Nelson SJ, Pieper RO, Phillips JJ, Ronen SM. Non-invasive in vivo assessment of IDH1 mutational status in glioma. Nat Commun 2013;4:2429.

59. Chaumeil MM, Larson PE, Woods SM, Cai L, Eriksson P, Robinson AE, Lupo JM, Vigneron DB, Nelson SJ, Pieper RO, Phillips JJ, Ronen SM. Hyperpolarized [1-13C] glutamate: a metabolic imaging biomarker of IDH1 mutational status in glioma. Cancer Res 2014;74(16):4247-4257.

60. Mazuel L, Schulte RF, Cladiere A, Speziale C, Lagree M, Leremboure M, Jean B, Durif F, Chassain C. Intracerebral synthesis of glutamine from hyperpolarized glutamate. Magn Reson Med 2016.

61. Koellisch U, Laustsen C, Norlinger TS, Ostergaard JA, Flyvbjerg A, Gringeri CV, Menzel MI, Schulte RF, Haase A, Stodkilde-Jorgensen H. Investigation of metabolic changes in STZ-induced diabetic rats with hyperpolarized [1-13C]acetate. Physiol Rep 2015;3(8).

62. von Morze C, Bok RA, Ohliger MA, Zhu Z, Vigneron DB, Kurhanewicz J. Hyperpolarized [13C]ketobutyrate, a molecular analog of pyruvate with modified specificity for LDH isoforms. Magn Reson Med 2016;75(5):1894-1900.

63. Park JM, Josan S, Jang T, Merchant M, Watkins R, Hurd RE, Recht LD, Mayer D, Spielman DM. Volumetric spiral chemical shift imaging of hyperpolarized [2-13C]pyruvate in a rat c6 glioma model. Magn Reson Med 2016;75(3):973-984.

64. Marco-Rius I, von Morze C, Sriram R, Cao P, Chang GY, Milshteyn E, Bok RA, Ohliger MA, Pearce D, Kurhanewicz J, Larson PE, Vigneron DB, Merritt M. Monitoring acute metabolic changes in the liver and kidneys induced by fructose and glucose using hyperpolarized [2-13C]dihydroxyacetone. Magn Reson Med 2017;77(1):65-73.

65. Cowan B. Theoretical background. In: Cowan B, editor. Nuclear magnetic resonance and relaxation. New York: Cambridge University Press; 1997. p 20-23.

66. Keeler J. Relaxation mechanisms. Understanding NMR spectroscopy: Wiley; 2002.

67. Haacke E, Brown R, Thompson M, Venkatesan R. Introductory signal acquisition methods: free induction decay, spin echoes, inversion recovery and spectroscopy. Magnetic resonance imaging: physical principles and sequence design: John Wiley & Sons, Inc; 1999. p 111-137.

68. Levitt MH. NMR spectroscopy. Spin dynamics: John Wiley & Sons, Ltd; 2008. p 39-61.

69. Outwater EK, Blasbalg R, Siegelman ES, Vala M. Detection of lipid in abdominal tissues with opposed-phase gradient-echo images at 1.5 T: techniques and diagnostic importance. Radiographics 1998;18(6):1465-1480.

70. Levitt MH. Internal spin interactions. Spin dynamics: John Wiley & Sons Ltd; 2008. p 195-227.

71. Jung BA, Weigel M. Spin echo magnetic resonance imaging. J Magn Reson Imaging 2013;37(4):805-817.

72. Hennig J, Nauerth A, Friedburg H. RARE imaging: a fast imaging method for clinical MR. Magn Reson Med 1986;3(6):823-833.

73. Elster AD. Gradient-echo MR imaging: techniques and acronyms. Radiology 1993;186(1):1-8.

74. Stehling MK, Turner R, Mansfield P. Echo-planar imaging: magnetic resonance imaging in a fraction of a second. Science 1991;254(5028):43-50.

75. King KF, Foo TK, Crawford CR. Optimized gradient waveforms for spiral scanning. Magn Reson Med 1995;34(2):156-160.

76. Cho HH, Choi YH, Cheon JE, Lee SM, Kim WS, Kim IO, Paek M. Free-Breathing Radial 3D Fat-Suppressed T1-Weighted Gradient-Echo Sequence for Contrast-Enhanced Pediatric Spinal Imaging: Comparison With T1-Weighted Turbo Spin-Echo Sequence. AJR Am J Roentgenol 2016;207(1):177-182.

77. Madio DP, Lowe IJ. Ultra-fast imaging using low flip angles and fids. Magn Reson Med 1995;34(4):525-529.

78. Sarty GE, Bennett R, Cox RW. Direct reconstruction of non-Cartesian k-space data using a nonuniform fast Fourier transform. Magn Reson Med 2001;45(5):908-915.

79. Beatty PJ, Nishimura DG, Pauly JM. Rapid gridding reconstruction with a minimal oversampling ratio. IEEE Trans Med Imaging 2005;24(6):799-808.

80. Tan H, Meyer CH. Estimation of k-space trajectories in spiral MRI. Magn Reson Med 2009;61(6):1396-1404.

81. Brateman L. Chemical shift imaging: a review. AJR Am J Roentgenol 1986;146(5):971-980.

82. Sogaard LV, Schilling F, Janich MA, Menzel MI, Ardenkjaer-Larsen JH. In vivo measurement of apparent diffusion coefficients of hyperpolarized 13C-labeled metabolites. NMR Biomed 2014;27(5):561-569.

83. Wang JX, Merritt ME, Sherry AD, Malloy CR. Accelerated chemical shift imaging of hyperpolarized 13C metabolites. Magn Reson Med 2016;76(4):1033-1038.

84. Lustig M, Donoho D, Pauly JM. Sparse MRI: The application of compressed sensing for rapid MR imaging. Magn Reson Med 2007;58(6):1182-1195.

85. Arunachalam A, Whitt D, Fish K, Giaquinto R, Piel J, Watkins R, Hancu I. Accelerated spectroscopic imaging of hyperpolarized C-13 pyruvate using SENSE parallel imaging. NMR Biomed 2009;22(8):867-873.

86. Sodickson DK, Manning WJ. Simultaneous acquisition of spatial harmonics (SMASH): fast imaging with radiofrequency coil arrays. Magn Reson Med 1997;38(4):591-603.

87. Pruessmann KP, Weiger M, Scheidegger MB, Boesiger P. SENSE: sensitivity encoding for fast MRI. Magn Reson Med 1999;42(5):952-962.

88. Griswold MA, Jakob PM, Heidemann RM, Nittka M, Jellus V, Wang J, Kiefer B, Haase A. Generalized autocalibrating partially parallel acquisitions (GRAPPA). Magn Reson Med 2002;47(6):1202-1210.

89. Zeng H, Constable RT. Image distortion correction in EPI: comparison of field mapping with point spread function mapping. Magn Reson Med 2002;48(1):137-146.

90. Papadakis NG, Smponias T, Berwick J, Mayhew JE. k-space correction of eddy-current-induced distortions in diffusion-weighted echo-planar imaging. Magn Reson Med 2005;53(5):1103-1111.

91. Geraghty BJ, Lau JY, Chen AP, Cunningham CH. Dual-Echo EPI sequence for integrated distortion correction in 3D time-resolved hyperpolarized 13C MRI. Magn Reson Med 2017.

92. Cunningham CH, Dominguez Viqueira W, Hurd RE, Chen AP. Frequency correction method for improved spatial correlation of hyperpolarized 13C metabolites and anatomy. NMR Biomed 2014;27(2):212-218.

93. Boesch C, Gruetter R, Martin E. Temporal and spatial analysis of fields generated by eddy currents in superconducting magnets: optimization of corrections and quantitative characterization of magnet/gradient systems. Magn Reson Med 1991;20(2):268-284.

94. Zhou XJ. Echo planar imaging. In: Bernstein MA, King KF, Zhou XJ, editors. Handbook of MRI pulse sequences: Elsevier Academic Press; 2004. p 702-739.

95. Lau AZ, Tunnicliffe EM, Frost R, Koopmans PJ, Tyler DJ, Robson MD. Accelerated human cardiac diffusion tensor imaging using simultaneous multislice imaging. Magn Reson Med 2015;73(3):995-1004.

96. Wielopolski PA, Schmitt F, Stehling MK. Echo-Planar Imaging Pulse Sequences. In: Schmitt F, Stehling MK, Turner R, editors. Echo-Planar Imaging: Theory, Technique and Application: Springer; 1998. p 97-98.

97. Miller JJ, Lau AZ, Teh I, Schneider JE, Kinchesh P, Smart S, Ball V, Sibson NR, Tyler DJ. Robust and high resolution hyperpolarized metabolic imaging of the rat heart at 7 T with 3D spectral-spatial EPI. Magn Reson Med 2016;75(4):1515-1524.

98. Cunningham CH, Vigneron DB, Chen AP, Xu D, Nelson SJ, Hurd RE, Kelley DA, Pauly JM. Design of flyback echo-planar readout gradients for magnetic resonance spectroscopic imaging. Magn Reson Med 2005;54(5):1286-1289.

99. Cunningham CH, Chen AP, Lustig M, Hargreaves BA, Lupo J, Xu D, Kurhanewicz J, Hurd RE, Pauly JM, Nelson SJ, Vigneron DB. Pulse sequence for dynamic volumetric imaging of hyperpolarized metabolic products. J Magn Reson 2008;193(1):139-146.

100. Feinberg DA, Turner R, Jakab PD, von Kienlin M. Echo-planar imaging with asymmetric gradient modulation and inner-volume excitation. Magn Reson Med 1990;13(1):162-169.

101. Koelsch BL, Reed GD, Keshari KR, Chaumeil MM, Bok R, Ronen SM, Vigneron DB, Kurhanewicz J, Larson PEZ. Rapid in vivo apparent diffusion coefficient mapping of hyperpolarized 13C metabolites. Magn Reson Med 2015;74(3):622-633.

102. Marco-Rius I, Gordon JW, Mattis AN, Bok R, Delos Santos R, Sukumar S, Larson PEZ, Vigneron DB, Ohliger MA. Diffusion-weighted imaging of hyperpolarized [13C]urea in mouse liver. J Magn Reson Imaging 2017.

103. Gordon JW, Vigneron DB, Larson PE. Development of a symmetric echo planar imaging framework for clinical translation of rapid dynamic hyperpolarized 13C imaging. Magn Reson Med 2017;77(2):826-832.

104. Qin Q. Point spread functions of the T2 decay in k-space trajectories with long echo train. Magn Reson Imaging 2012;30(8):1134-1142.

105. Meyer CH, Pauly JM, Macovski A, Nishimura D. Simultaneous spatial and spectral selective excitation. Magn Reson Med 1990;15(2):287-304.

106. Larson PE, Kerr AB, Chen AP, Lustig MS, Zierhut ML, Hu S, Cunningham CH, Pauly JM, Kurhanewicz J, Vigneron DB. Multiband excitation pulses for hyperpolarized 13C dynamic chemical-shift imaging. J Magn Reson 2008;194(1):121-127.

107. Reed GD, Larson PE, Morze C, Bok R, Lustig M, Kerr AB, Pauly JM, Kurhanewicz J, Vigneron DB. A method for simultaneous echo planar imaging of hyperpolarized 13C pyruvate and 13C lactate. J Magn Reson 2012;217:41-47.

108. Shin PJ, Larson PE, Uecker M, Reed GD, Kerr AB, Tropp J, Ohliger MA, Nelson SJ, Pauly JM, Lustig M, Vigneron DB. Chemical shift separation with controlled aliasing for hyperpolarized 13C metabolic imaging. Magn Reson Med 2015;74(4):978-989.

109. Mulkern RV, Panych LP. Echo planar spectroscopic imaging. Concepts Magn Reson 2001;13:213-237.

110. Guilfoyle DN, Blamire A, Chapman B, Ordidge RJ, Mansfield P. PEEP--a rapid chemical-shift imaging method. Magn Reson Med 1989;10(2):282-287.

111. Mansfield P. Spatial mapping of the chemical shift in NMR. Magn Reson Med 1984;1(3):370-386.

112. Cunningham CH, Chen AP, Albers MJ, Kurhanewicz J, Hurd RE, Yen YF, Pauly JM, Nelson SJ, Vigneron DB. Double spin-echo sequence for rapid spectroscopic imaging of hyperpolarized 13C. J Magn Reson 2007;187(2):357-362.

113. Chen AP, Kurhanewicz J, Bok R, Xu D, Joun D, Zhang V, Nelson SJ, Hurd RE, Vigneron DB. Feasibility of using hyperpolarized [1-13C]lactate as a substrate for in vivo metabolic 13C MRSI studies. Magn Reson Imaging 2008;26(6):721-726.

114. Larson PE, Bok R, Kerr AB, Lustig M, Hu S, Chen AP, Nelson SJ, Pauly JM, Kurhanewicz J, Vigneron DB. Investigation of tumor hyperpolarized [1-13C]-pyruvate dynamics using time-resolved multiband RF excitation echo-planar MRSI. Magn Reson Med 2010;63(3):582-591.

115. Hu S, Lustig M, Chen AP, Crane J, Kerr A, Kelley DA, Hurd R, Kurhanewicz J, Nelson SJ, Pauly JM, Vigneron DB. Compressed sensing for resolution enhancement of hyperpolarized 13C flyback 3D-MRSI. J Magn Reson 2008;192(2):258-264.

116. Hu S, Lustig M, Balakrishnan A, Larson PE, Bok R, Kurhanewicz J, Nelson SJ, Goga A, Pauly JM, Vigneron DB. 3D compressed sensing for highly accelerated hyperpolarized 13C MRSI with in vivo applications to transgenic mouse models of cancer. Magn Reson Med 2010;63(2):312-321.

117. Larson PE, Hu S, Lustig M, Kerr AB, Nelson SJ, Kurhanewicz J, Pauly JM, Vigneron DB. Fast dynamic 3D MR spectroscopic imaging with compressed sensing and multiband excitation pulses for hyperpolarized 13C studies. Magn Reson Med 2011;65(3):610-619.

118. Otazo R, Tsai SY, Lin FH, Posse S. Accelerated short-TE 3D proton echo-planar spectroscopic imaging using 2D-SENSE with a 32-channel array coil. Magn Reson Med 2007;58(6):1107-1116.

119. Tsai SY, Otazo R, Posse S, Lin YR, Chung HW, Wald LL, Wiggins GC, Lin FH. Accelerated proton echo planar spectroscopic imaging (PEPSI) using GRAPPA with a 32-channel phased-array coil. Magn Reson Med 2008;59(5):989-998.

120. Milshteyn E, Zhang X. The Need and Initial Practice of Parallel Imaging and Compressed Sensing in Hyperpolarized 13C MRI in vivo. OMICS J Radiol 2015;4(4).

121. Shin PJ, Larson PE, Ohliger MA, Elad M, Pauly JM, Vigneron DB, Lustig M. Calibrationless parallel imaging reconstruction based on structured low-rank matrix completion. Magn Reson Med 2014;72(4):959-970.

122. Feng Y, Gordon JW, Shin PJ, von Morze C, Lustig M, Larson PEZ, Ohliger MA, Carvajal L, Tropp J, Pauly JM, Vigneron DB. Development and testing of hyperpolarized 13C MR calibrationless parallel imaging. J Magn Reson 2016;262:1-7.

123. Meyer CH, Hu BS, Nishimura DG, Macovski A. Fast spiral coronary artery imaging. Magn Reson Med 1992;28(2):202-213.

124. King KF. Spiral. In: Bernstein MA, King KF, Zhou XJ, editors. Handbook of MRI pulse sequences: Elsevier Academic Press; 2004. p 928-954.

125. Spielman DM, Pauly JM, Meyer CH. Magnetic resonance fluoroscopy using spirals with variable sampling densities. Magn Reson Med 1995;34(3):388-394.

126. Tsai CM, Nishimura DG. Reduced aliasing artifacts using variable-density k-space sampling trajectories. Magn Reson Med 2000;43(3):452-458.

127. Kim DH, Adalsteinsson E, Spielman DM. Simple analytic variable density spiral design. Magn Reson Med 2003;50(1):214-219.

128. Chang C, Glover GH. Variable-density spiral-in/out functional magnetic resonance imaging. Magn Reson Med 2011;65(5):1287-1296.

129. Takahashi A, Peters T. Compensation of multi-dimensional selective excitation pulses using measured k-space trajectories. Magn Reson Med 1995;34(3):446-456.

130. Irarrazabal P, Meyer CH, Nishimura DG, Macovski A. Inhomogeneity correction using an estimated linear field map. Magn Reson Med 1996;35(2):278-282.

131. Man LC, Pauly JM, Macovski A. Improved automatic off-resonance correction without a field map in spiral imaging. Magn Reson Med 1997;37(6):906-913.

132. Lau AZ, Chen AP, Ghugre NR, Ramanan V, Lam WW, Connelly KA, Wright GA, Cunningham CH. Rapid multislice imaging of hyperpolarized 13C pyruvate and bicarbonate in the heart. Magn Reson Med 2010;64(5):1323-1331.

133. Gordon JW, Niles DJ, Adamson EB, Johnson KM, Fain SB. Application of flow sensitive gradients for improved measures of metabolism using hyperpolarized 13C MRI. Magn Reson Med 2016;75(3):1242-1248.

134. Lau AZ, Miller JJ, Robson MD, Tyler DJ. Cardiac perfusion imaging using hyperpolarized 13C urea using flow sensitizing gradients. Magn Reson Med 2016;75(4):1474-1483.

135. Lau AZ, Miller JJ, Robson MD, Tyler DJ. Simultaneous assessment of cardiac metabolism and perfusion using copolarized [1-13C]pyruvate and 13C-urea. Magn Reson Med 2017;77(1):151-158.

136. Adalsteinsson E, Irarrazabal P, Topp S, Meyer C, Macovski A, Spielman DM. Volumetric spectroscopic imaging with spiral-based k-space trajectories. Magn Reson Med 1998;39(6):889-898.

137. Mayer D, Levin YS, Hurd RE, Glover GH, Spielman DM. Fast metabolic imaging of systems with sparse spectra: application for hyperpolarized 13C imaging. Magn Reson Med 2006;56(4):932-937.

138. Mayer D, Yen YF, Tropp J, Pfefferbaum A, Hurd RE, Spielman DM. Application of subsecond spiral chemical shift imaging to real-time multislice metabolic imaging of the rat in vivo after injection of hyperpolarized 13C1-pyruvate. Magn Reson Med 2009;62(3):557-564.

139. Josan S, Yen YF, Hurd R, Pfefferbaum A, Spielman D, Mayer D. Application of double spin echo spiral chemical shift imaging to rapid metabolic mapping of hyperpolarized [1-13C]-pyruvate. J Magn Reson 2011;209(2):332-336.

140. Mayer D, Yen YF, Takahashi A, Josan S, Tropp J, Rutt BK, Hurd RE, Spielman DM, Pfefferbaum A. Dynamic and high-resolution metabolic imaging of hyperpolarized [1-13C]-pyruvate in the rat brain using a high-performance gradient insert. Magn Reson Med 2011;65(5):1228-1233.

141. Xu T, Mayer D, Gu M, Yen YF, Josan S, Tropp J, Pfefferbaum A, Hurd R, Spielman D. Quantification of in vivo metabolic kinetics of hyperpolarized pyruvate in rat kidneys using dynamic 13C MRSI. NMR Biomed 2011;24(8):997-1005.

142. Josan S, Hurd R, Park JM, Yen YF, Watkins R, Pfefferbaum A, Spielman D, Mayer D. Dynamic metabolic imaging of hyperpolarized [2-13C]pyruvate using spiral chemical shift imaging with alternating spectral band excitation. Magn Reson Med 2014;71(6):2051-2058.

143. Dixon WT. Simple proton spectroscopic imaging. Radiology 1984;153(1):189-194.

144. Glover GH. Multipoint Dixon technique for water and fat proton and susceptibility imaging. J Magn Reson Imaging 1991;1(5):521-530.

145. Reeder SB, Pineda AR, Wen Z, Shimakawa A, Yu H, Brittain JH, Gold GE, Beaulieu CH, Pelc NJ. Iterative decomposition of water and fat with echo asymmetry and least-squares estimation (IDEAL): application with fast spin-echo imaging. Magn Reson Med 2005;54(3):636-644.

146. Wiesinger F, Weidl E, Menzel MI, Janich MA, Khegai O, Glaser SJ, Haase A, Schwaiger M, Schulte RF. IDEAL spiral CSI for dynamic metabolic MR imaging of hyperpolarized [1-13C]pyruvate. Magn Reson Med 2012;68(1):8-16.

147. Durst M, Koellisch U, Gringeri C, Janich MA, Rancan G, Frank A, Wiesinger F, Menzel MI, Haase A, Schulte RF. Bolus tracking for improved metabolic imaging of hyperpolarised compounds. J Magn Reson 2014;243:40-46.

148. Koellisch U, Gringeri CV, Rancan G, Farell EV, Menzel MI, Haase A, Schwaiger M, Schulte RF. Metabolic imaging of hyperpolarized [1-13C]acetate and [1-13C]acetylcarnitine - investigation of the influence of dobutamine induced stress. Magn Reson Med 2015;74(4):1011-1018.

149. Leupold J, Mansson S, Petersson JS, Hennig J, Wieben O. Fast multiecho balanced SSFP metabolite mapping of 1H and hyperpolarized 13C compounds. MAGMA 2009;22(4):251-256.

150. Shang H, Sukumar S, von Morze C, Bok RA, Marco-Rius I, Kerr A, Reed GD, Milshteyn E, Ohliger MA, Kurhanewicz J, Larson PEZ, Pauly JM, Vigneron DB. Spectrally selective three-dimensional dynamic balanced steady-state free precession for hyperpolarized C-13 metabolic imaging with spectrally selective radiofrequency pulses. Magn Reson Med 2017;78(3):963-975.

151. Laustsen C, Stokholm Norlinger T, Christoffer Hansen D, Qi H, Mose Nielsen P, Bonde Bertelsen L, Henrik Ardenkjaer-Larsen J, Stodkilde Jorgensen H. Hyperpolarized 13C urea relaxation mechanism reveals renal changes in diabetic nephropathy. Magn Reson Med 2016;75(2):515-518.

152. Altbach MI, Outwater EK, Trouard TP, Krupinski EA, Theilmann RJ, Stopeck AT, Kono M, Gmitro AF. Radial fast spin-echo method for T2-weighted imaging and T2 mapping of the liver. J Magn Reson Imaging 2002;16(2):179-189.

153. Ramirez MS, Lee J, Walker CM, Sandulache VC, Hennel F, Lai SY, Bankson JA. Radial spectroscopic MRI of hyperpolarized [1-13C] pyruvate at 7 tesla. Magn Reson Med 2014;72(4):986-995.

154. Schmidt R, Laustsen C, Dumez JN, Kettunen MI, Serrao EM, Marco-Rius I, Brindle KM, Ardenkjaer-Larsen JH, Frydman L. In vivo single-shot 13C spectroscopic imaging of hyperpolarized metabolites by spatiotemporal encoding. J Magn Reson 2014;240:8-15.

155. Bedard PL, Hansen AR, Ratain MJ, Siu LL. Tumour heterogeneity in the clinic. Nature 2013;501(7467):355-364.

156. Junttila MR, de Sauvage FJ. Influence of tumour micro-environment heterogeneity on therapeutic response. Nature 2013;501(7467):346-354.

157. Serrao EM, Rodrigues TB, Gallagher FA, Kettunen MI, Kennedy BW, Vowler SL, Burling KA, Brindle KM. Effects of fasting on serial measurements of hyperpolarized [1-13C]pyruvate metabolism in tumors. NMR Biomed 2016;29(8):1048-1055.

158. Pauly JM, Nishimura D, Macovski A. A k-space analysis of small tip excitation. J Magn Reson 1989;81:43-56.

159. Pauly J, Le Roux P, Nishimura D, Macovski A. Parameter relations for the Shinnar-Le Roux selective excitation pulse design algorithm [NMR imaging]. IEEE Trans Med Imaging 1991;10(1):53-65.

160. Glover GH. Simple analytic spiral K-space algorithm. Magn Reson Med 1999;42(2):412-415.

161. Durst M, Koellisch U, Frank A, Rancan G, Gringeri CV, Karas V, Wiesinger F, Menzel MI, Schwaiger M, Haase A, Schulte RF. Comparison of acquisition schemes for hyperpolarised 13C imaging. NMR Biomed 2015;28(6):715-725.

162. Schulte RF, Sperl JI, Weidl E, Menzel MI, Janich MA, Khegai O, Durst M, Ardenkjaer-Larsen JH, Glaser SJ, Haase A, Schwaiger M, Wiesinger F. Saturation-recovery metabolic-exchange rate imaging with hyperpolarized [1-13C] pyruvate using spectral-spatial excitation. Magn Reson Med 2013;69(5):1209-1216.

163. Lai S, Glover GH. Three-dimensional spiral fMRI technique: a comparison with 2D spiral acquisition. Magn Reson Med 1998;39(1):68-78.

164. Bernstein MA. Three-dimensional acquisition. In: Bernstein MA, King KF, Zhou XJ, editors. Handbook of MRI pulse sequences: Elsevier Academic Press; 2004. p 424-442.

165. Sukumar S, Hu S, Larson PE, Zhang VY, Ohliger MA, Bok R, Kurhanewicz J, Vigneron DB. Single-shot, 2D and 3D dynamic imaging of hyperpolarized 13C biomarkers in vivo at 14.1 Tesla. In Proceedings of the 20th Annual Meeting of ISMRM, Melbourne, Australia 2012:4292.

166. Irarrazabal P, Nishimura DG. Fast three dimensional magnetic resonance imaging. Magn Reson Med 1995;33(5):656-662.

167. Irarrazabal P, Santos JM, Guarini M, Nishimura D. Flow properties of fast three-dimensional sequences for MR angiography. Magn Reson Imaging 1999;17:1469-1479.

168. Shu Y, Riederer SJ, Bernstein MA. Three-dimensional MRI with an undersampled spherical shells trajectory. Magn Reson Med 2006;56(3):553-562.

169. Wu HH, Nishimura DG. 3D magnetization-prepared imaging using a stack-of-rings trajectory. Magn Reson Med 2010;63(5):1210-1218.

170. Asslander J, Zahneisen B, Hugger T, Reisert M, Lee HL, LeVan P, Hennig J. Single shot whole brain imaging using spherical stack of spirals trajectories. Neuroimage 2013;73:59-70.

171. van Gorp JS, Bakker CJ, Bouwman JG, Smink J, Zijlstra F, Seevinck PR. Geometrically undistorted MRI in the presence of field inhomogeneities using compressed sensing accelerated broadband 3D phase encoded turbo spin-echo imaging. Phys Med Biol 2015;60(2):615-631.

172. Kettunen MI, Kennedy BW, Hu DE, Brindle KM. Spin echo measurements of the extravasation and tumor cell uptake of hyperpolarized [1-13C]lactate and [1-13C]pyruvate. Magn Reson Med 2013;70(5):1200-1209.

173. Xu D, Maier JK, King KF, Collick BD, Wu G, Peters RD, Hinks RS. Prospective and retrospective high order eddy current mitigation for diffusion weighted echo planar imaging. Magn Reson Med 2013;70(5):1293-1305.

174. Wang J, Kreis F, Wright AJ, Hesketh RL, Levitt MH, Brindle KM. Dynamic 1 H imaging of hyperpolarized [1-13C]lactate in vivo using a reverse INEPT experiment. Magn Reson Med 2017.

175. Gallagher FA, Bohndiek SE, Kettunen MI, Lewis DY, Soloviev D, Brindle KM. Hyperpolarized 13C MRI and PET: in vivo tumor biochemistry. J Nucl Med 2011;52(9):1333-1336.

176. Gutte H, Hansen AE, Henriksen ST, Johannesen HH, Ardenkjaer-Larsen J, Vignaud A, Hansen AE, Borresen B, Klausen TL, Wittekind AM, Gillings N, Kristensen AT, Clemmensen A, Hojgaard L, Kjaer A. Simultaneous hyperpolarized 13C-pyruvate MRI and 18F-FDG-PET in cancer (hyperPET): feasibility of a new imaging concept using a clinical PET/MRI scanner. Am J Nucl Med Mol Imaging 2015;5(1):38-45.

177. Serrao EM, Brindle KM. Potential Clinical Roles for Metabolic Imaging with Hyperpolarized [1-13C]Pyruvate. Front Oncol 2016;6:59.

178. Wang J, Wright AJ, Hu DE, Hesketh R, Brindle KM. Single shot three-dimensional pulse sequence for hyperpolarized 13C MRI. Magn Reson Med 2017;77(2):740-752.

179. Park JY, Garwood M. Spin-echo MRI using pi/2 and pi hyperbolic secant pulses. Magn Reson Med 2009;61(1):175-187.

180. Tannus A, Garwood M. Adiabatic pulses. NMR Biomed 1997;10(8):423-434.

181. Zhu X, Gordon JW, Larson PE. Slice selective adiabatic refocusing pulses for high field, pre-clinical hyperpolarized C-13 imaging. In Proceedings of the 24th Annual Meeting of ISMRM, Honolulu, Hawaii USA 2017.

182. Sacolick LI, Wiesinger F, Hancu I, Vogel MW. B1 mapping by Bloch-Siegert shift. Magn Reson Med 2010;63(5):1315-1322.

183. Glover GH, Lai S. Self-navigated spiral fMRI: interleaved versus single-shot. Magn Reson Med 1998;39(3):361-368.

184. Daniels CJ, McLean MA, Schulte RF, Robb FJ, Gill AB, McGlashan N, Graves MJ, Schwaiger M, Lomas DJ, Brindle KM, Gallagher FA. A comparison of quantitative methods for clinical imaging with hyperpolarized 13C-pyruvate. NMR Biomed 2016;29(4):387-399.

185. Moore J, Jankiewicz M, Anderson AW, Gore JC. Evaluation of non-selective refocusing pulses for 7 T MRI. J Magn Reson 2012;214(1):212-220.

186. Odedra S, Wimperis S. Use of composite refocusing pulses to form spin echoes. J Magn Reson 2012;214(1):68-75.

187. Levine D, Zuo C, Faro CB, Chen Q. Potential heating effect in the gravid uterus during MR HASTE imaging. J Magn Reson Imaging 2001;13(6):856-861.

188. Busse RF, Hariharan H, Vu A, Brittain JH. Fast spin echo sequences with very long echo trains: design of variable refocusing flip angle schedules and generation of clinical T2 contrast. Magn Reson Med 2006;55(5):1030-1037.

189. Foxall DL, Harvey PR, Huang J. Rapid iterative reconstruction for echo planar imaging. Magn Reson Med 1999;42(3):541-547.

190. Chen NK, Avram AV, Song AW. Two-dimensional phase cycled reconstruction for inherent correction of echo-planar imaging Nyquist artifacts. Magn Reson Med 2011;66(4):1057-1066.

191. Ahn CB, Cho ZH. A new phase correction method in NMR imaging based on autocorrelation and histogram analysis. IEEE Trans Med Imaging 1987;6(1):32-36.

192. Skare S, Clayton D, Newbould R, Moseley M, Bammer R. A fast and robust minimum entropy based non-interactive Nyquist host correction algorithm. In Proceedings of the 14th Annual Meeting of ISMRM, Seattle, Washington, USA 2006:p2349.

193. Price R, Allison J, Clarke G, Dennis M, Hendrick R, Keener C, Masten J, Nessaiver M, Och J, Reeve D. 2015 Magnetic Resonance Imaging Quality Control Manual. American College of Radiology Website (https://shop.acr.org/Default.aspx?TabID=55&ProductId=731499117)2015.

194. Wang Z, Bovik AC, Sheikh HR, Simoncelli EP. Image quality assessment: from error visibility to structural similarity. IEEE Trans Image Process 2004;13(4):600-612.

195. Grant AK, Vinogradov E, Wang X, Lenkinski RE, Alsop DC. Perfusion imaging with a freely diffusible hyperpolarized contrast agent. Magn Reson Med 2011;66(3):746-755.

196. von Morze C, Bok RA, Reed GD, Ardenkjaer-Larsen JH, Kurhanewicz J, Vigneron DB. Simultaneous multiagent hyperpolarized 13C perfusion imaging. Magn Reson Med 2014;72(6):1599-1609.

197. Luk Pat GT, Meyer CH, Pauly JM, Nishimura DG. Reducing flow artifacts in echo-planar imaging. Magn Reson Med 1997;37(3):436-447.

198. Luo Y, Rydzewski J, de Graaf RA, Gruetter R, Garwood M, Schleich T. In vivo observation of lactate methyl proton magnetization transfer in rat C6 glioma. Magn Reson Med 1999;41(4):676-685.

199. Frydman L, Blazina D. Ultrafast two-dimensional nuclear magnetic resonance spectroscopy of hyperpolarized solutions. Nature Physics 2007;3(6):415-419.

200. Giraudeau P, Shrot Y, Frydman L. Multiple ultrafast, broadband 2D NMR spectra of hyperpolarized natural products. J Am Chem Soc 2009;131(39):13902-13903.

201. Sarkar R, Comment A, Vasos PR, Jannin S, Gruetter R, Bodenhausen G, Hall H, Kirik D, Denisov VP. Proton NMR of 15N-choline metabolites enhanced by dynamic nuclear polarization. J Am Chem Soc 2009;131(44):16014-16015.

202. Harris T, Giraudeau P, Frydman L. Kinetics from indirectly detected hyperpolarized NMR spectroscopy by using spatially selective coherence transfers. Chemistry 2011;17(2):697-703.

203. Dzien P, Fages A, Jona G, Brindle KM, Schwaiger M, Frydman L. Following Metabolism in Living Microorganisms by Hyperpolarized 1H NMR. J Am Chem Soc 2016;138(37):12278-12286.

204. Chekmenev EY, Norton VA, Weitekamp DP, Bhattacharya P. Hyperpolarized 1H NMR employing low gamma nucleus for spin polarization storage. J Am Chem Soc 2009;131(9):3164-3165.

205. Truong ML, Coffey AM, Shchepin RV, Waddell KW, Chekmenev EY. Sub-second proton imaging of 13C hyperpolarized contrast agents in water. Contrast Media Mol Imaging 2014;9(5):333-341.

206. Mishkovsky M, Cheng T, Comment A, Gruetter R. Localized in vivo hyperpolarization transfer sequences. Magn Reson Med 2012;68(2):349-352.

207. Sorensen OW. Polarization transfer experimetns in high-resolution NMR spectroscopy. Prog NMR Spectrosc 1989;21:503-569.

208. Levitt MH. Many-spin dynamics. Spin dynamics: John Wiley & Sons, Ltd; 2008. p 467-505.

209. Yen YF, Le Roux P, Mayer D, King R, Spielman D, Tropp J, Butts Pauly K, Pfefferbaum A, Vasanawala S, Hurd R. T2 relaxation times of 13C metabolites in a rat hepatocellular carcinoma model measured in vivo using 13C-MRS of hyperpolarized [1-13C]pyruvate. NMR Biomed 2010;23(4):414-423.

210. Wijnen JP, Haarsma J, Boer VO, Luijten PR, van der Stigchel S, Neggers SF, Klomp DW. Detection of lactate in the striatum without contamination of macromolecules by J-difference editing MRS at 7T. NMR Biomed 2015;28(4):514-522.

211. Madan A, Ganji SK, An Z, Choe KS, Pinho MC, Bachoo RM, Maher EM, Choi C. Proton T2 measurement and quantification of lactate in brain tumors by MRS at 3 Tesla in vivo. Magn Reson Med 2015;73(6):2094-2099.

212. Levitt MH. Experiments on AX systems. Spin dynamics: John Wiley & Sons, Ltd; 2008. p 409-452.

213. Hoult D, Lauterbur P. The sensitivity of the zeugmatographic experiment involving human samples. J Magn Reson 1979;34:425-433.

214. Darrasse L. Perspectives with cryogenic RF probes in biomedical MRI. Biochimie 2003;85(9):915-937.

215. Poirier-Quinot M, Ginefri JC, Girard O, Robert P, Darrasse L. Performance of a miniature high-temperature superconducting (HTS) surface coil for in vivo microimaging of the mouse in a standard 1.5T clinical whole-body scanner. Magn Reson Med 2008;60(4):917-927.

216. Hu B, Varma G, Randell C, Keevil S, Schaeffter T, Glover P. A novel receive-only liquid nitrogen (LN_2)-cooled RF coil for high-resolution in vivo imaging on a 3-Tesla whole-body scanner. IEEE Trans Instrum Meas 2012;61:129-139.

217. Wagenhaus B, Pohlmann A, Dieringer MA, Els A, Waiczies H, Waiczies S, Schulz-Menger J, Niendorf T. Functional and morphological cardiac magnetic resonance imaging of mice using a cryogenic quadrature radiofrequency coil. PLoS One 2012;7(8):e42383.

218. Norton VA, Weitekamp DP. Communication: partial polarization transfer for single-scan spectroscopy and imaging. J Chem Phys 2011;135(14):141107.

219. Coffey AM, Truong ML, Chekmenev EY. Low-field MRI can be more sensitive than high-field MRI. J Magn Reson 2013;237:169-174.

220. Stenger VA, Boada FE, Noll DC. Variable-density spiral 3D tailored RF pulses. Magn Reson Med 2003;50(5):1100-1106.

221. Pauly J, Nishimura D, Macovski A. A linear class of large-tip-angle selective excitation pulses. J Magn Reson 1989;82:571-587.

222. Kennedy BW, Kettunen MI, Hu DE, Brindle KM. Probing lactate dehydrogenase activity in tumors by measuring hydrogen/deuterium exchange in hyperpolarized l-[1-13C,U-2H]lactate. J Am Chem Soc 2012;134(10):4969-4977.